



# Report on optimised stimulation scenario for Acoculco

D7.2

# Report on optimised stimulation scenario for Acoculco

D 7.2

Version 2

Task Lead: Dr. Hannes Hofmann (GFZ)

Contributors: Dr. Francesco Parisio (TUBAF), Baptiste Lepillier (TUD), Dr. Thibault Candela (TNO), Dr. Elisabeth Peters (TNO), Michal Kruszewski (Fraunhofer IEG), Leandra Weydt (TUDA)

Work package 7

30.05.2020

Website: <http://www.gemex-h2020.eu>



The GEMex project is supported by the European Union's Horizon 2020 programme for Research and Innovation under grant agreement No 727550

# Table of Contents<sup>1</sup>

<b>List of figures</b>	<b>5</b>
<b>List of tables</b>	<b>8</b>
<b>Executive summary</b>	<b>9</b>
<b>1 Introduction</b>	<b>10</b>
<b>2 Conceptual model of Acoculco</b>	<b>10</b>
2.1 Faults and fractures	10
2.2 Stress field	11
2.3 Exploration wells EAC-1 and EAC-2	13
2.4 Rock properties	14
<b>3 Hydraulic fracturing analysis of EAC-1 with MFrac</b>	<b>16</b>
3.1 Introduction	16
3.2 Methodology	17
3.3 Model setup	17
3.3.1 Fracture geometry model and constitutive relationships	17
3.3.2 Model properties	18
3.4 Results and discussion	19
3.4.1 Sensitivity analysis	19
3.4.2 Forward modelling scenarios	20
3.5 Conclusions	22
<b>4 Hydraulic and acid fracturing analysis of EAC-2 with MFrac</b>	<b>22</b>
4.1 Introduction	22
4.2 Methodology	22
4.3 Model setup	22
4.4 Results and discussion	25
4.4.1 Hydraulic fracturing scenarios at different depths	25
4.4.2 Influence of injection rate on treatment parameters, fracture geometry, fracture conductivity and thermal and water fronts	27
4.4.3 Injection parameters required to achieve different fracture half-lengths and influence on fracture geometry	30
4.4.4 Influence of acid diffusivity and concentration on fracture conductivity and width	30
4.4.5 Influence of multiple fracture growth on fracture dimensions	32
4.4.6 Influence of stress gradient on fracture dimensions	32

---

<sup>1</sup> The content of this report reflects only the authors' view. The Innovation and Networks Executive Agency (INEA) is not responsible for any use that may be made of the information it contains.

4.5	<i>Conclusions</i>	33
<b>5</b>	<b>Analytical and numerical analysis of hydraulic fracturing and fracture re-opening</b>	<b>33</b>
5.1	<i>Introduction</i>	33
5.2	<i>Methodology</i>	34
5.2.1	Fluid-driven fracture propagation	34
5.2.2	Lower interface elements for re-injection modelling	35
5.3	<i>Model setup</i>	35
5.3.1	Fluid-driven fracture propagation	35
5.3.2	Re-injection modelling	36
5.4	<i>Results</i>	36
5.4.1	Hydraulic fracturing scenarios	36
5.4.2	Fracture re-opening scenarios	38
5.5	<i>Discussion and conclusions</i>	40
<b>6</b>	<b>Analysis of hydraulic stimulation of pre-existing fracture network with OpenGeoSys</b>	<b>41</b>
6.1	<i>Introduction</i>	41
6.2	<i>Methodology</i>	42
6.3	<i>Model setup</i>	42
6.4	<i>Results and discussion</i>	43
6.5	<i>Conclusions</i>	46
<b>7</b>	<b>Induced seismicity and permeability enhancement during fluid injection</b>	<b>47</b>
7.1	<i>Introduction</i>	47
7.2	<i>Methods and model setup</i>	47
7.3	<i>Results</i>	50
7.4	<i>Discussion and conclusions</i>	53
<b>8</b>	<b>EGS development options for EAC-1 and EAC-2</b>	<b>54</b>
8.1	<i>Stimulation type</i>	54
8.1.1	Thermal stimulation	54
8.1.2	Hydraulic shear stimulation	54
8.1.3	Hydraulic fracturing	55
8.1.4	Chemical stimulation	55
8.2	<i>Zonal isolation</i>	55
8.2.1	Open hole stimulation	56
8.2.2	Injection string	56
8.2.3	Casing packer	57
8.2.4	Open hole packer	57
8.2.5	Case and cement	57
8.3	<i>Wellbore integrity</i>	58
8.4	<i>Stimulation targets and scenarios</i>	58
8.4.1	Scenario 1: Stimulation of skarns below 800 m	59

8.4.2	Scenario 2: Stimulation of marbles at 1200 – 1300 m or 1600 – 1650 m in EAC-1 and 1500 – 1600 m in EAC-2	60
8.4.3	Scenario 3: Stimulation of granites below 1700 m in EAC-1 and below 1600 m in EAC-2	60
<b>9</b>	<b>EGS development workflow for EAC-1 and EAC-2</b>	<b>60</b>
<b>10</b>	<b>Conclusion</b>	<b>62</b>
	<b>References</b>	<b>63</b>
	<b>Acknowledgments</b>	<b>69</b>

## List of figures

Figure 1:	Fault zones marked green on the geological cross-section (A) and the closest fault intersection zone marked green on the structural geological top-view map (B) are potential stimulation targets (adapted from Kruszewski et al. submitted). .....	11
Figure 2:	A) The Acoculco caldera: shaded relief map of Acoculco with main villages and roads in the region; blue bands represent caldera faults; red markers – maximum horizontal stress direction indicators from the World Stress Map Heidbach et al. 2016); green markers – maximum horizontal stress direction indicators from the Apan-Tezontepec scoria cones (García-Palomo et al., 2018); red dots – registered historical seismicity (between 1976 and 2017) with four bubble sizes representing event magnitudes (0.8 – 2.5, 2.5– 3.0, 3.0 – 3.375, and 3.375 – 4.40) (García-Palomo et al., 2018); EAC-1 and EAC-2 wells are marked with blue triangles; B) Distribution of the TMVB and regional tectonic setting through Central America; location of the studied area is represented with red squares. Figure and caption taken from Kruszewski et al. (submitted). .....	12
Figure 3:	A) Pore pressure $P_p$ , B) minimum horizontal stress $S_{hmin}$ , C) maximum horizontal stress $S_{Hmax}$ , D) vertical stress $S_v$ and E) formation breakdown pressure FBP for Acoculco near EAC-1 and EAC-2 from Kruszewski et al. (submitted). .....	13
Figure 4:	Results of the borehole logging campaigns in the EAC-2 well: A) gamma ray, B) main mineral components, C) compressional and shear wave velocities, D) bulk and grain density, E) total and effective porosities, F) deep resistivity, G) dynamic Poisson's ratio, H) dynamic Young's modulus, I) unconfined compressive strength. Figure and caption from Kruszewski et al. (submitted). .....	14
Figure 5:	MFrac rock properties based on well logs in EAC-2 and laboratory experiments. Laboratory data was used for the formations where no well log data was available. ....	24
Figure 6:	MFrac leak-off parameters based on well logs in EAC-2 and laboratory experiments (where no well log data was available). Fluid viscosity of reservoir fluid and filtrate fluid were set constant to 0.3 mPas and wall building coefficient $C_w$ of 5000 cm/min <sup>1/2</sup> (equivalent to no filter cake) and spurt loss coefficient of 0 cm were assigned to the whole model. ....	24
Figure 7:	Scenario 1 - Hydraulic fracture geometry at the end of injection (before closure) resulting from injection of 1062 m <sup>3</sup> water at 50 l/s below the casing shoe (open hole interval 800 – 1100 m) in EAC-1. ....	25
Figure 8:	Scenario 2 (base case) - Hydraulic fracture geometry at the end of injection (before closure) resulting from injection of 1062 m <sup>3</sup> water at 50 l/s below the casing shoe (open hole interval 800 – 1900 m). ....	26
Figure 9:	Scenario 3 - Hydraulic fracture geometry at the end of injection (before closure) resulting from injection of 1062 m <sup>3</sup> water at 50 l/s below 1500 m (open hole interval 1500 – 1900 m). ....	26

Figure 10: Scenario 4 - Hydraulic fracture geometry at the end of injection (before closure) resulting from injection of 1062 m <sup>3</sup> water at 50 l/s below 1800 m (open hole interval 1800 – 1900 m).....	27
Figure 11: Treatment parameters volume and time required to achieve a fracture half-length of 300 m in Scenario 2 (base case) and resulting fracture height and width at the end of the treatment (before fracture closure) for different water injection rates. ....	28
Figure 12: Fracture conductivity along one fracture wing at the end of the treatment (before closure) resulting from the different flow rate scenarios to achieve a fracture half-length of 300 m in Scenario 2 (base case). ....	28
Figure 13: Top view of thermal and water fronts of one fracture wing resulting from injection with 16.67 l/s (top), 50 l/s (center), 100 l/s (bottom) until a fracture half-length of 300 m is reached. ....	29
Figure 14: Treatment parameters (left) and fracture dimensions (right) at the end of the treatment (before closure) for different target fracture half-lengths when injecting water at 50 l/s in Scenario 2 (base case). ....	30
Figure 15: Fracture conductivity along one fracture wing at the end of the treatment (before closure) resulting from different HCl concentrations, equilibrium (eq.) concentrations and diffusivities. ....	31
Figure 16: Average fracture width along one fracture wing at the end of the treatment (before closure) resulting from different HCl concentrations, equilibrium (eq.) concentrations and diffusivities compared to the fracture width without acid.....	31
Figure 17: Fracture conductivity along one fracture wing at the end of the treatment (before closure) resulting from multiple parallel fracture growth compared to the base case scenario where only one single hydraulic fracture develops. ....	32
Figure 18: Hydraulic fracture geometry at the end of injection (before closure) resulting from injection of 1062 m <sup>3</sup> water at 50 l/s in the open hole interval 800 – 1900 m with a stress gradient of 12.0 MPa/km (top left), 19.2 MPa/km (bottom left), and 26.4 MPa/km (bottom right), and below the casing shoe (open hole interval 800 – 1100 m; top right). ....	33
Figure 19: Penny-shaped fluid driven fracture in an elastic porous medium.....	35
Figure 20: Evolution of hydraulic fracture width (a) and permeability (b) with time for hot and cold water injection....	37
Figure 21: Evolution of hydraulic fracture radius (a) and width (c) at different times for $Q_0 = 0.1 \text{ m}^3/\text{s}$ and for different flow rates (b, d) after 20 minutes of injection when injecting hot and cold fluid. ....	37
Figure 22: A rapid injection case (a) shows the initial pressure decay as a consequence of re-opening the existing crack, while continuous long-term injection will later pressurize the crack to failure (c), unless the crack is connected to a permeable fracture network (b). The width profile (d) along the crack at different time shows the different pressurization efficiency for the connected and non-connected case. A similar argument can be drawn for the pore pressure profile (e). ....	39
Figure 23: Deformed contour map of pressure during short-time water injection with variable flow rate at different time steps. The time instances are indicated as points in the time vs. pressure curve on the right side of each contour map. ....	40
Figure 24: Pre-processing methodology from reservoir scale to extracted, rotated and scaled DFNs used for the phase field simulations.....	42

Figure 25: Hydraulic fracture models using the variational phase-field approach with sub-DFNs of the limestone reservoir. The matrix domain $\Omega$ is shown in grey. The natural fracture domain $\Gamma$ is shown in black. The red dot represents the wellbore. ....	44
Figure 26: Hydraulic fracture models using the variational phase-field approach with sub-DFNs of the marble reservoir. The matrix domain $\Omega$ is shown in grey. The natural fracture domain $\Gamma$ is shown in black. The red dot represents the wellbore.....	45
Figure 27: Hydraulic fracture models using the variational phase-field approach with sub-DFNs of the skarn reservoir. The matrix domain $\Omega$ is shown in grey. The natural fracture domain $\Gamma$ is shown in black. The red dot represents the wellbore.....	46
Figure 28: Workflow to simulate induced seismicity and permeability enhancement during fluid injection throughout a fault. ....	47
Figure 29: Synthetic fault surface geometries used as inputs for our modelling strategy. ....	48
Figure 30: Constant (top) and cyclic (bottom) injection schemes used for the fault reactivation study. ....	49
Figure 31: Pre-injection distance to criticality at 800 m injection depth for the smooth (left) and rough (right) fault scenario. ....	50
Figure 32: Simulation results for the smooth fault and injection depth of 800 m. ....	51
Figure 33: Simulation results for the rough fault and injection depth of 800 m. ....	51
Figure 34: Simulation results for the smooth fault and injection depth of 1750 m. ....	52
Figure 35: Simulation results for the rough fault and injection depth of 1750 m. ....	52
Figure 36: Changes in the bottom hole pressure during constant (top) and cyclic (bottom) injection for the scenarios with an injection depth of 1750 m, and a constant permeability. Red circles represent the times of induced rupture events. ....	53
Figure 37: Summary of zonal isolation options. A) no zonal isolation with injection through the wellhead, B) no zonal isolation with injection through an injection string, C) isolation between casing and open hole by inflatable packer in casing, D) straddle packer system to isolate the desired target section, E) case and cement the well down to the target interval. ....	56
Figure 38: Frictional pressure losses resulting from cold water injection or production through a 4” ID casing of variable length L. ....	57
Figure 39: Wellbore schematic, lithology, identified fractures, temperature logs 6 hours after drilling, fluid losses during drilling and potential stimulation target zones (green) in wells EAC-1 (left) and EAC-2 (right). ....	59
Figure 40: Proposed EGS development workflow for Exploration wells EAC-1 or EAC-2 in Acoculco. It is recommended to start with EAC-1.....	62

## List of tables

Table 2.1: Completion of well EAC-1 .....	13
Table 2.2: Completion of well EAC-2 .....	14
Table 2.3: Overview of selected petrophysical and rock mechanical rock properties retrieved from Weydt et al. (submitted) and Lepillier et al. (submitted, marked with an *). Data for marble, skarn and granodiorite is retrieved from outcrop samples collected in the exhumed system in Las Minas (marked with **). .....	16
Table 3.1: Rock properties data for the sensitivity analysis and forward modelling scenarios. ....	19
Table 3.2: Leak-off parameter for the sensitivity analysis and forward modelling scenarios. Note that the permeability of the injection interval was set to zero. ....	19
Table 3.3: Sensitivity analysis for injection parameters slurry rate (SR) and injection volume (V <sub>tot</sub> ) and Mode 1 fracture toughness (K <sub>IC</sub> ) as an example for a rock property. ....	20
Table 3.4: MFrac simulation results for the four forward modelling scenarios using laboratory rock properties. ....	21
Table 6.1: Input parameters for the OpenGeoSys phase field models. ....	43
Table 7.1: Range of scenarios covered in this fault reactivation study. ....	48



## Executive summary

Acoculco is one of the geothermal areas in Mexico, which is located at the eastern part of the Trans-Mexican Volcanic Belt. The Comisión Federal de Electricidad (CFE) drilled two exploration wells in this area, EAC-1 in 1995 and EAC-2 in 2008. Both wells found high temperatures, but low productivity. Therefore, the area is regarded as a potential site for Enhanced Geothermal System (EGS) development.

Based on the reservoir characterization carried out in SP2 and wellbore information provided by CFE, several EGS development scenarios were investigated. Given the large uncertainties regarding stress field, local structures, local hydrogeology and status of the wells these scenarios should be considered as options and input to take informed decisions. This report summarizes relevant exploration results (Chapter 2), discusses various numerical modelling results (Chapter 3-7), and looks into several EGS development options for the two exploration wells in Acoculco (Chapter 8). Finally, a workflow is presented for a stepwise development of EAC-1 and EAC-2 to an EGS (Chapter 9). This workflow aims to reduce uncertainties and risks and allows to gain valuable knowledge for future developments of the Acoculco geothermal field.

Overall, the chances to develop a commercially successful EGS without drilling new wells but using only the existing exploration wells EAC-1 and EAC-2 in Acoculco were found to be relatively low. Nevertheless, the optimized stimulation concept for Acoculco allows to increase the chance of success at the lowest operational risk. The knowledge gained by the proposed injection tests in the existing exploration wells can be the basis for a controlled development of an EGS in Acoculco with new wells specifically designed for stimulation, if this is required. The stimulation concept for EAC-1 and EAC-2 involves a combined hydraulic shear stimulation and thermal stimulation of pre-existing inflow zones in marbles and granites to access permeable fault damage zones near the wells. This may be done by open hole stimulation without zonal isolation.

# 1 Introduction

The Acoculco Caldera is located in the Trans-Mexican Volcanic Belt. Two ~2 km deep exploration wells drilled in the caldera found sufficiently high temperatures for electricity generation ( $>260^{\circ}\text{C}$ ), but very low permeability. Early studies characterizing the Acoculco Caldera include for example Verma (2001), López-Hernández et al. (2009), Canet et al. (2010), Pfeiffer et al. (2014) and Canet et al. (2015). During this time, the area was already identified by CFE, the operator of the wells, as potential Enhanced Geothermal System (EGS) site.

Since the start of the GEMex project in 2016 the site has been extensively characterized by re-assessment of existing data, acquisition of new geophysical (e.g., Carrillo et al., 2020) and geological field data (e.g., Calcagno et al. 2018), determination of petro-physical properties of analogue rocks (Weydt et al., 2018) and numerical modelling studies (e.g., Lepillier et al., 2019). Based on this data a stepwise approach towards a stimulation concept is developed, taking into account technical and economic feasibility, environmental risks, and geological uncertainty.

First, the conceptual reservoir model of the Acoculco geothermal field is summarized including information on faults and fractures, stress field, exploration wells, and rock properties. Then, different development options are discussed and finally an EGS development workflow for Acoculco is presented. Individual studies performed within this task are displayed in separate chapters. First, hydraulic fracturing scenarios are simulated with linear stress gradients leading to excessive fracture height growth without stress barriers (Chapter 3). Then, well log data was used to introduce heterogeneity in stress and rock properties which led to better constrained hydraulic fractures. Acid fracturing scenarios show how these fractures may stay open due to etched fracture surfaces. Additionally, the hydraulic and thermal influence zones during stimulation treatments were simulated in Chapter 4. Chapter 5 investigates the re-opening of such hydraulic fractures and Chapter 6 shows how such a hydraulic fracture interacts with natural fracture systems. Finally, shearing of natural faults and associated permeability increase and induced seismicity is simulated in Chapter 7.

The thermal and hydraulic performance of a range of simulated stimulation scenarios presented here is simulated and evaluated in GEMex Deliverable 7.1 (Peters et al. 2020b).

## 2 Conceptual model of Acoculco

### 2.1 Faults and fractures

Two regional fault systems are present in Acoculco: NW-SE striking oblique to strike-slip faults and NE-SW striking oblique to normal faults (Figure 1). These systems were mapped as close as 100 m to the exploration wells and are believed to be active. However, none of the surface traces could be associated to fluid loss zones in the wells. Instead, faults intersecting the wells seem to be closed by mineral precipitation. Outcrop studies indicate that the associated fault damage zones are typically less than 20 m wide but may be as wide as 100 m within the caldera. Fractures inside these damage zones typically strike NE, NW and NS. Fracture frequency away from the faults is significantly less compared to the fault damage zones (Kruszewski et al. submitted). Thus, fault damage zones associated to the mapped NW and NE striking surface structures and their intersections may be potential stimulation targets. However, these structures may also pose the risk of fluid-injection induced seismicity, which is assessed in GEMex Deliverable D7.3 (Peters et al. 2020a) and Chapter 7.

A systematic mapping of fracture frequencies in analogue outcrops by Lepillier et al. (2020) may be summarized as follows: Frequent natural fractures with large aperture are found in limestones. Skarns are

frequently fractured, but fractures are short and have a low aperture. Few, but longer natural fractures with smaller aperture exist in marbles. No information is available about the granites. Additionally, it was observed that fractures are often sub-vertical (mostly 70-85°) and sealed with quartz, calcite, pyrite and epidote (Rocha et al. 2006). While all formations are naturally fractured, it appears that from the investigated lithologies limestones are the most suitable targets to stimulate a pre-existing fracture network followed by marbles and skarns. Since limestones are not present in the open hole sections of EAC-1 and EAC-2, marbles are identified as most promising target formation given that no information is available on granites.

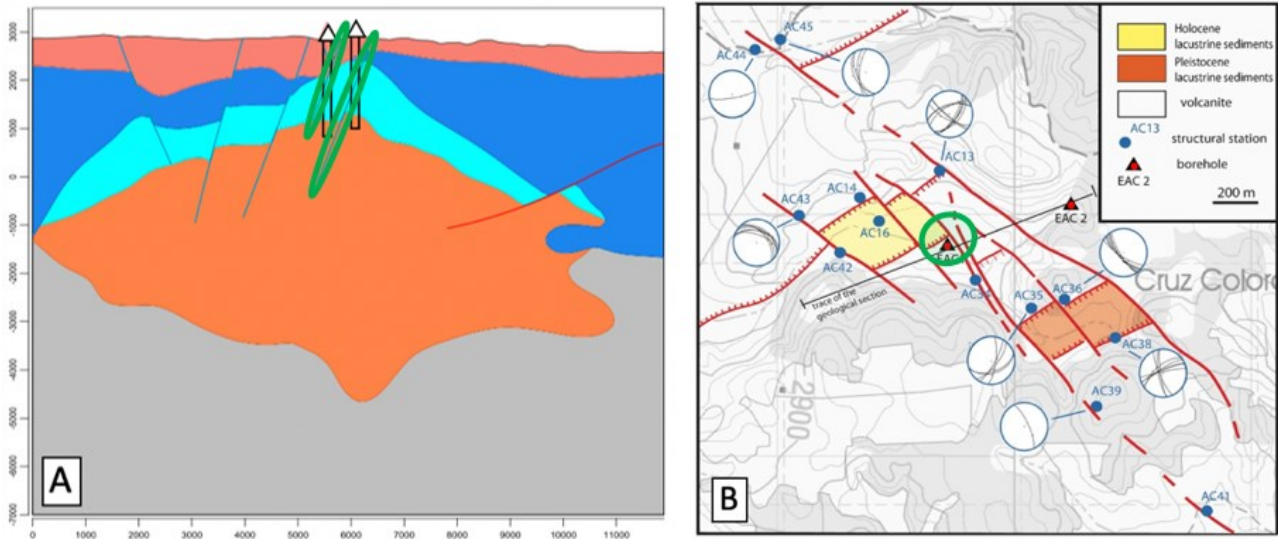


**Figure 1: Fault zones marked green on the geological cross-section (A) and the closest fault intersection zone marked green on the structural geological top-view map (B) are potential stimulation targets (adapted from Kruszewski et al. submitted).**

## 2.2 Stress field

Data on the stress field in Acoculco is very scarce. The stress field can therefore not be well determined. Nevertheless, comprehensive analysis of geological, drilling, and borehole logging data allowed to provide reasonable constraints on the stress field. The detailed stress field analysis for Acoculco is described in Kruszewski et al. (submitted). Their analysis suggests a normal ( $S_v \geq S_{Hmax} \geq S_{hmin}$ ) to strike-slip ( $S_{Hmax} \geq S_v \geq S_{hmin}$ ) faulting regime. Both stress states would promote the development of vertical hydraulic fractures and the shear stimulation of vertical pre-existing fractures instead of horizontal ones. The regional  $S_{Hmax}$  direction is N56°E±5° (Figure 2). Local stresses near EAC-1 and EAC-2 may significantly differ from this due to extensive faults and caldera structures. Best estimates of the pore pressure and stress gradients are  $\Delta P_p=8.73$  MPa/km,  $\Delta S_{hmin}=19.2\pm7.2$  MPa/km,  $\Delta S_v=24.3\pm1.5$  MPa/km,  $\Delta S_{Hmax}=34.4\pm21.4$  MPa/km (Figure 3). Based on the available data no stress barriers could be determined that would prevent excessive fracture height growth during stimulation.



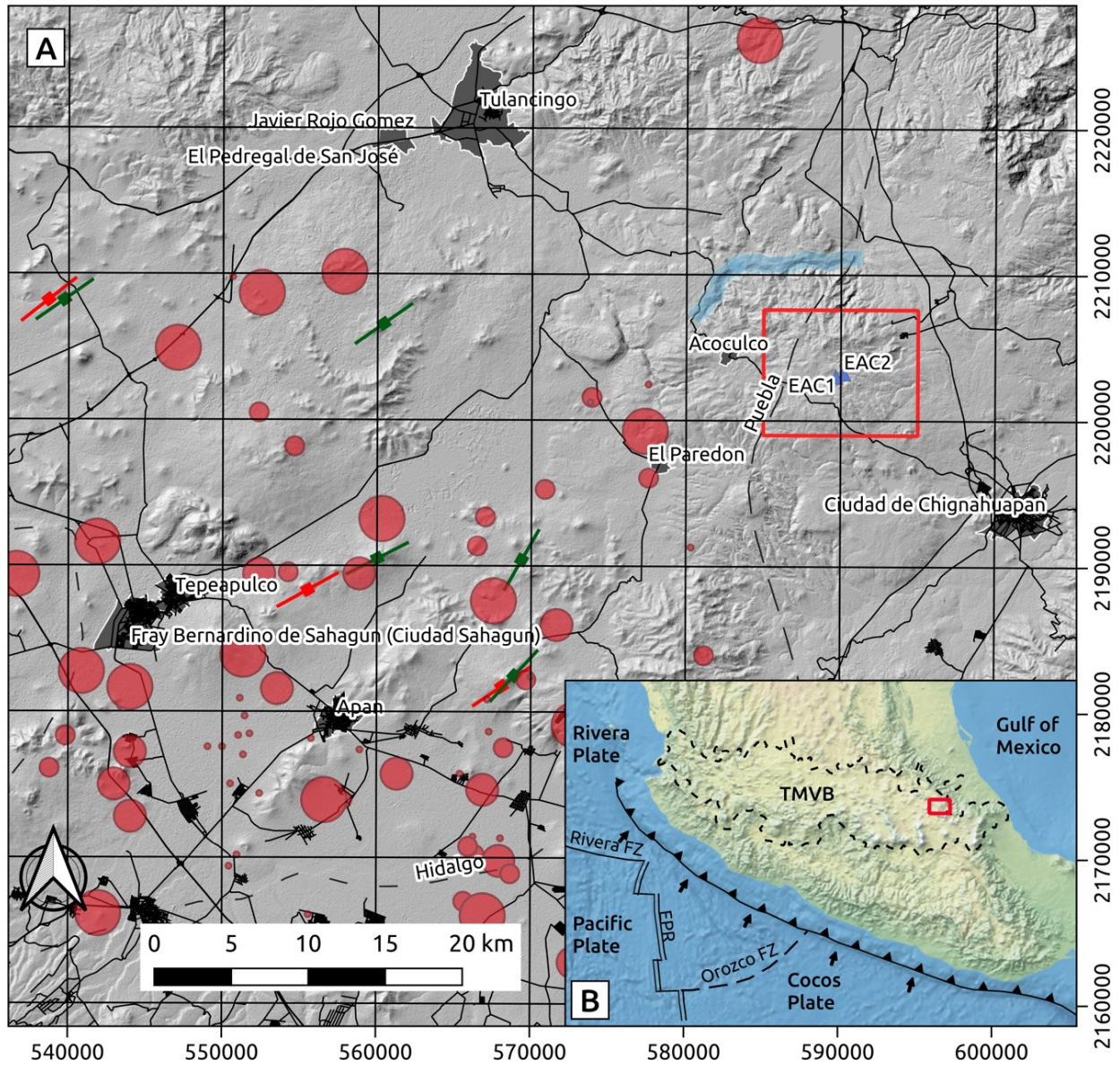


**Figure 2:** A) The Acoculco caldera: shaded relief map of Acoculco with main villages and roads in the region; blue bands represent caldera faults; red markers – maximum horizontal stress direction indicators from the World Stress Map (Heidbach et al. 2016); green markers – maximum horizontal stress direction indicators from the Apan-Tezontepec scoria cones (García-Palomo et al., 2018); red dots – registered historical seismicity (between 1976 and 2017) with four bubble sizes representing event magnitudes (0.8 – 2.5, 2.5– 3.0, 3.0 – 3.375, and 3.375 – 4.40) (García-Palomo et al., 2018); EAC-1 and EAC-2 wells are marked with blue triangles; B) Distribution of the TMVB and regional tectonic setting through Central America; location of the studied area is represented with red squares. Figure and caption taken from Kruszewski et al. (submitted).

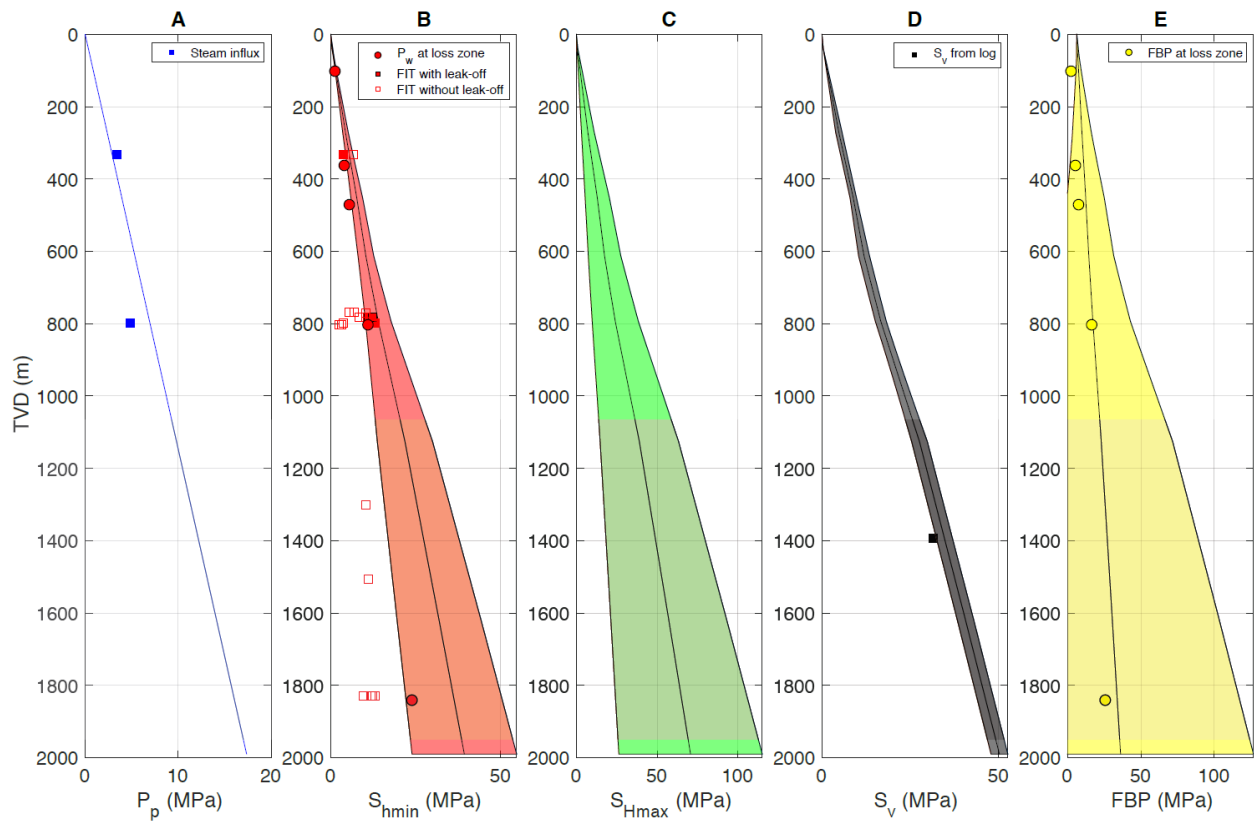


Figure 3: A) Pore pressure  $P_p$ , B) minimum horizontal stress  $S_{hmin}$ , C) maximum horizontal stress  $S_{Hmax}$ , D) vertical stress  $S_v$  and E) formation breakdown pressure FBP for Acoculco near EAC-1 and EAC-2 from Kruszewski et al. (submitted).

## 2.3 Exploration wells EAC-1 and EAC-2

The vertical exploration wells EAC-1 and EAC-2 were drilled in 1995 and 2008, respectively. Both wells are cased from surface to 800 m with 8 ½” casing. The potential reservoir rocks, which are skarns, marbles, and granites, are accessed by a 1200 m and 1100 m long open hole section of 5 7/8” to 6” diameter (Table 2.1 and Table 2.2). The cased section above the reservoir rocks is comprised of volcanics and limestones (Figure 39). Only limited fluid losses were encountered during drilling and only small temperature anomalies could be identified. At least for EAC-1 it is known that overbalanced drilling was used with fluid density between 1040 and 1280 kg/m<sup>3</sup>. This may have caused near wellbore damage. Well logs for this study were only available for EAC-2 and only from ~800 m to ~1400 m (Figure 4).

Drill bit diameter (cm)	Casing outside diameter (cm)	Steel grade	Casing weight (kg/m)	Casing setting depth (m)	Casing type
44.45	33.97	K-55	81.11	0 – 10	Surface
31.12	24.45	L-80	69.94	0 – 187.4	Anchor
21.59	17.78	N-80	55.06	0 – 800	Production
15.24	-	-	-	800 – 1500	Open hole
14.92	-	-	-	1500 – 2000	Open hole

Table 2.1: Completion of well EAC-1.

Drill bit diameter (cm)	Casing outside diameter (cm)	Steel grade	Casing weight (kg/m)	Casing setting depth (m)	Casing type
44.45	33.97	K-55	81.10	0 – 9.52	Surface
31.12	24.45	L-80	69.94	0 – 200.08	Anchor
21.59	17.78	L-80	43.16	0 – 798.85	Production
14.92	-	-	-	798.85 – 1900	Open hole

Table 2.2: Completion of well EAC-2.

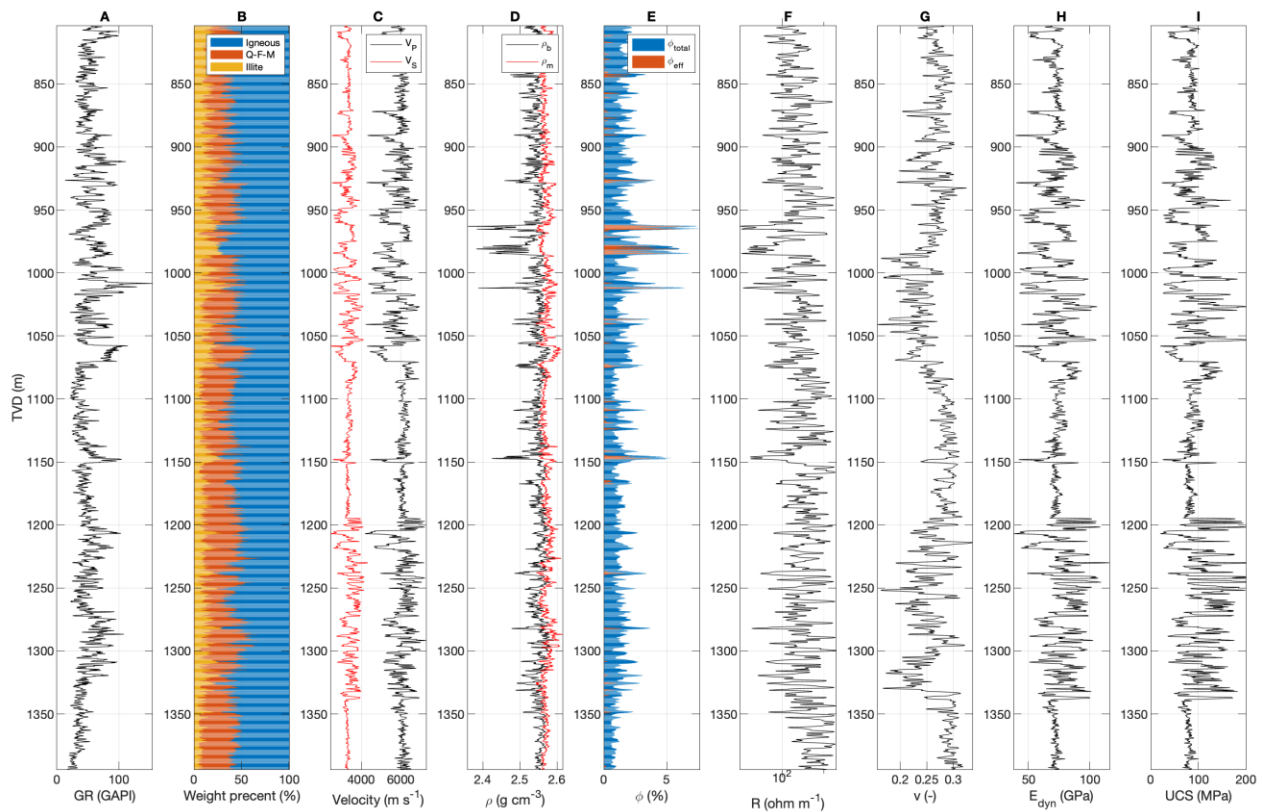


Figure 4: Results of the borehole logging campaigns in the EAC-2 well: A) gamma ray, B) main mineral components, C) compressional and shear wave velocities, D) bulk and grain density, E) total and effective porosities, F) deep resistivity, G) dynamic Poisson's ratio, H) dynamic Young's modulus, I) unconfined compressive strength. Figure and caption from Kruszewski et al. (submitted).

## 2.4 Rock properties

A representative summary of hydraulic and mechanical rock properties determined on outcrop samples within Task 6.1 and Task 7.1 is summarized in Table 2.3. Matrix permeability and porosity of the carbonatic basement, metamorphic and intrusive rocks are generally smaller than  $10^{-17}$  m<sup>2</sup> and  $< 5$  %, respectively. However, fine fractures and joints led to matrix permeabilities of up to  $10^{-15}$  m<sup>2</sup>. The volcanic rocks collected in the study area represent different stratigraphic units from Miocene to Pleistocene age as described in Avellán et al. (2018) and cover various rock types. The results of the petrophysical and rock mechanical parameters show a wide parameter range caused by the high geological heterogeneity. Additionally, hydrothermal alteration observed in some outcrops significantly increased matrix porosity and permeability (up to 50% and



$10^{-12}$  m<sup>2</sup>, Perdernal rhyolitic lavas). In contrast, matrix porosity and permeability of the volcanic units in the deep subsurface analysed on reservoir core samples from well EAC1 range between 3 and 7,5 % and  $10^{-16}$  to  $10^{-18}$  m<sup>2</sup> (Deliverable 7.1; Peters et al. 2020b), respectively, and are within the range of the skarns, marbles and granodiorites (< 5 % and  $10^{-17}$  m<sup>2</sup>). Although all reservoir core samples contain healed fractures and fissures, Figure 4 indicates that only the volcanic rocks, which are present above the open hole sections of the wells EAC-1 and EAC-2, have a high porosity and permeability. The rock matrix of the entire open hole sections consisting of limestones, marbles, skarns and granites/granodiorites has a porosity below 5 % and a permeability below  $1\text{E-}17$  m<sup>2</sup>. Thus, the rock matrix is likely not contributing to flow.

Regarding the basement rocks, the marbles and skarns are the stiffest of the tested rocks followed by granite and limestone. Stiffer rocks lead to the development of larger hydraulic fractures with smaller apertures (Hofmann et al. 2014). However, given the limited range this effect will be insignificant. Elastic fracture height growth barriers may only be present based on local heterogeneities. Poisson's ratio is lowest in skarn and limestones, and significantly higher for granite and marble. A high Poisson's ratio may lead to higher minimum horizontal stresses in granites and a low Poisson's ratio may lead to lower minimum horizontal stresses in skarns (Zoback 2007).

The basaltic lavas belonging to the Zacatlán basaltic plateau and the Augile basaltic trachyandesitic lavas have the highest uniaxial compressive strength (UCS) and tensile strength. Hydrothermal alteration led to reduced UCS in the rhyolitic and Miocene andesitic lavas. The UCS of limestones and marbles is relatively low compared to the significantly stronger skarns and granites. On the other hand, limestones have a higher fracture toughness and tensile strength as compared to the other rocks tested and marbles have a comparatively low tensile strength and the lowest fracture toughness. Based on this, relatively low pressures should be sufficient to hydraulically fracture marbles and higher pressures would be required to fracture limestones.

Parameters	$\phi$	K	UCS	E	$\mu$	TS	K <sub>IC</sub> *	G <sub>c</sub> *
Unit	[%]	[m <sup>2</sup> ]	[MPa]	[GPa]	[-]	[MPa]	[MPa m <sup>1/2</sup> ]	[Pa m]
<b>Volcanic rocks</b>								
Rhyolitic lava (mainly Pedernal rhyolitic lava)	27,99 (76) ± 16,18	4,98E-13/ <b>1,7E-15</b> (54) ± 1,72E-12	42,15 (28) ± 42,33	9,48 (17) ± 7,88	0,11 (16) ± 0,07	9,52 (4) ± 4,75	-	-
Dacitic lava	4,32 (8) ± 2,26	1,7E-18/ <b>1,5E-18</b> (7) ± 7,45E-19	63,05 (6) ± 8,48	14,51 (1)	0,26 (1)	-	-	-
Terrerillos andesitic lava	4,14 (7) ± 2,24	1,1E-17/ <b>4,9E-18</b> (6) ± 1,6E-17	-	-	-	13,63 (5) ± 2,06	-	-
Manzanito basaltic trachyandesitic lava	15,98 (9) ± 1,75	2,56E-14/ <b>6,4E-15</b> (7) ± 2,98E-14	71,67 (4) ± 11,81	23,60 (3) ± 1,19	0,17 (3) ± 0,04	11,67 (3) ± 1,60	-	-
Augile basaltic trachyandesitic lava	1,65 (19) ± 1,2	4,64E-18/ <b>3,5E-18</b> (16) ± 3,26E-18	242,0 (9) ± 102,5	33,2 (6) ± 6,59	0,17 (6) ± 0,07	40,93 (3) ± 4,31	-	-
Pyroclastics (undef.)	13,13 (18) ± 1,48	2,44E-14/ <b>6,17E-17</b> (10) ± 5,27E-14	-	-	-	-	-	-

Acoculco ignimbrite	52,69 (1)	-	-	-	-	-	-	-
Miocene basaltic trachyandesitic lava	11,61 (2) ± 0,55	5,19E-16 (2) ± 2,98E-16	61,99 (1)	-	-	42,50 (1)	-	-
Miocene andesitic lava	7,56 (19) ± 7,52	8,79E-16/ <b>1,4E-17</b> (14) ± 2,32E-15	90,76 (12) ± 37,69	13,61 (5) ± 3,56	0,12 (5) ± 0,06	8,33 (3) ± 1,81	-	-
Zacatlán basaltic plateau	10,48 (16) ± 3,9	4,92E-18/ <b>3,9E-18</b> (16) ± 3,58E-18	164,0 (9) ± 78,38	26,21 (6) ± 7,53	0,18 (6) ± 0,12	50,33 (12) ± 10,33	-	-
Carbonatic basement, metamorphic and intrusive rocks								
Limestone K	1,05 (134) ± 0,9	1E-15/ <b>3,1E-18</b> (86) ± 6,6E-15	129,3 (16) ± 44,46	29,29 (13) ± 11,1	0,16 (12) ± 0,11	15,08 (45) ± 5,31	2,63	182
Limestones/ Sandstones J	8,88 (12) ± 6,75	1,34E-14/ <b>2,4E-15</b> (12) ± 3,72E-14	-	37,74 (3) ± 7,46	0,10 (3) ± 0,02	-	-	-
Marbles **	1,55 (73) ± 1,78	1,34E-14/ <b>2,4E-15</b> (12) ± 3,72E-14	117,7 (11) ± 50,41	39,27 (11) ± 13,92	0,23 (11) ± 0,08	12,66 (49) ± 5,97	1,87	71,4
Skarn **	4,12 (99) ± 3,99	6,01E-12/ <b>2,4E-17</b> (81) ± 4,6E-11	185,0 (22) ± 51,41	44,05 (16) ± 7,50	0,16 (16) ± 0,08	15,15 (37) ± 6,62	2,31	108
Granite/ Granodiorite **	3,56 (25) ± 3,12	6,13E-17/ <b>57E-18</b> (16) ± 1,55E-16	171,3 (8) ± 25,86	37,35 (6) ± 6,71	0,24 (6) ± 0,15	16,20 (16) ± 3,58	2,36	130

arithmetic mean values in normal font, the numbers in bold represent geometric mean values, ± = standard deviation, () = number of analysed plugs, φ = Porosity, K = Permeability, UCS = Unconfined compressive strength, E = Static Young's modulus, μ = Poisson ratio, TS = Tensile strength, K<sub>IC</sub> = Fracture toughness, G<sub>C</sub> = Critical energy release rate

**Table 2.3: Overview of selected petrophysical and rock mechanical rock properties retrieved from Weydt et al. (submitted) and Lepillier et al. (submitted, marked with an \*). Data for marble, skarn and granodiorite is retrieved from outcrop samples collected in the exhumed system in Las Minas (marked with \*\*).**

### 3 Hydraulic fracturing analysis of EAC-1 with MFract

This chapter is based on the internal GEMex report “Acoculco Wellbore Hydraulic Fracture Stimulation models” by Baptiste Lepillier and Hannes Hofmann (December 13, 2019).

#### 3.1 Introduction

Given the low intrinsic rock permeability in the Acoculco wells hydraulic fracturing may be a suitable stimulation technique for Acoculco, especially to overcome near-wellbore damage and intersect pre-existing fracture networks close to the well. Therefore, hydraulic fracturing simulations have been performed using the commercial hydraulic fracturing simulator MFract. The software was validated within the GEMex project on laboratory hydraulic fracturing experiments in GEMex Deliverable 6.5 (Deb et al. 2019). This work is meant to provide an overview of the influence of a range of injection parameters on hydraulic fracture development for the assumptions stated below.



## 3.2 Methodology

For the hydraulic fracturing simulations, the commercial simulator MFract was used. The semi-analytical simulator is formulated between a pseudo-3D and full 3D model, including a coupling between fracture propagation and proppant transport. The main reasons for this choice were the 3D modelling capabilities, an extensive material database, the wide acceptance in the industry, the verification on laboratory experiments within GEMex (Deb et al. 2019) and integrated thermal and acid fracturing solutions. Fracture initiation and development is based on tensile opening of new fractures within intact rock. Major assumptions are that fractures can only develop horizontally or vertically, and the fracture shape is elliptical. The model is based on mass and momentum conservation, the continuity equation and a width-opening pressure equation. Details on the model implementation can be found in the extensive User's Guide (Baker Hughes 2019).

First, a sensitivity analysis was performed to evaluate the influence of different variables involved in the hydraulic fracturing process: i) for in-situ parameters, such as the fracture toughness or stress field and ii) for operational parameters, such as injection rate (here called "slurry rate" SR), and the total injected volume  $V_{tot}$ . Once the problem is better constrained, we present the predictive models for hydraulic fracturing treatments in well EAC-1. Here, we simulate different amounts of total injected fluid volume (500 m<sup>3</sup>, 1000 m<sup>3</sup>, and 2500 m<sup>3</sup>) using the rock physical properties measured on the samples in the laboratory. Additionally, we repeat the same simulations using upscaled rock properties following the Geological Strength Index correction by Hoek et al. (2002) and Marinatos and Hoek (2000). For both cases, we calculate 4 different scenarios:

- Scenario a: Hydraulic fracturing of the well in its present state. That means with an open hole section from 800 m to 1900 m
- Scenario b: Cased hole with perforations between 1500 and 1600 m MD and rock properties of marble
- Scenario c: Cased hole with perforations between 1700 and 1800 m MD and rock properties of skarn
- Scenario d: Cased hole with perforations between 1800 and 1900 m MD and rock properties of granodiorite

It is important to keep in mind that, regarding the high number of uncertainties, this model is mainly intended to guide the design of the stimulation job. A more realistic model could be calculated once more accurate measurements are provided especially for lithology distribution and stress field orientation and magnitude.

In this study, the models are built using an idealized well lithological section with no parameter variations between the different geological units. This analysis also does not consider thermal stresses, acidization and the use of proppants. Pure water is used as injection fluid.

## 3.3 Model setup

### 3.3.1 Fracture geometry model and constitutive relationships

Since no field data for verification is available, most model parameters and constitutive relationships were assumed to be as simple as possible. The following model parameters were used:

- Fracture Geometry: 3-Dimensional

This is a 3-dimensional planar fracture model. Fractures propagate in vertical and lateral direction. For long and short fractures, the model approaches the Perkins-Kern-Nordgren (PKN) constant height type geometry (Perkins and Kern 1961, Nordgren 1972). Without contrasts in confining stress, toughness or elastic moduli,

the model approaches a vertical radial-type geometry. This model is applicable for all length to height aspect ratios.

*Fracture flowback: off*

Fracture flowback turned on would allow fluid and proppant to flow back from the fracture into the well. It would be required to simulate cross-flow between fractures in multiple layer. We did not use this option.

*Fracture simulate to closure: off*

Fracture propagation and lateral proppant transport is not simulated after pumping (during closure) unless a flow rate of zero is input in the treatment schedule.

*Fracture fluid gradient: excluded*

It is assumed that the pressure within the fracture is not depth dependent. If the hydrostatic pressure gradient would be included this would affect pressure distribution and fracture propagation.

*Fracture propagation parameters: positive growth only*

The fracture propagation option “positive growth only” overrides the mass conservation, continuity and momentum equations by not allowing fractures to recede.

*Fracture initiation interval: Min. Stress Interval*

With this option, the formation stress profile along the perforated interval is examined. The portion of the perforated interval that contains the minimum closure pressure required to keep the fracture open is selected for fracture initiation. This may not be the interval which contains the lowest minimum horizontal stress. An initial fracture height equal to 10% of the total perforation interval height is assumed.

*Fracture friction model: off*

For the fluid flow calculation, laminar flow in a rectangular slot, modified for an ellipsoidal fracture width, is used. The Darcy friction factor takes the form  $f_D = 24/Re$ , with the Reynolds number  $Re$ . This should be valid unless very low viscosity fluids such as gas are pumped at high rates, which would induce turbulent flow.

*Fracture wall roughness: off*

Without wall roughness, the  $f_D$  inside the fracture is used without modification. This option would allow to include effects of roughness or waviness on the frictional dissipation.

*Fracture tip effects: off*

Tip effects represent a flow resistance at the fracture tip. These may be due to viscosity effects or some other phenomena such as tip geometry. As this effect is not well defined it is recommended to neglect it unless evidence for it is found in the data.

### **3.3.2 Model properties**

The well design described in Table 2.1 was used for the MFrac model with the difference that the 7” production casing does not go through to the surface but stops at 200 m depth. The same well design was used for all simulations even though smaller diameters would result from operations with tubing or the installation of a deeper liner. The bottom hole treating pressure (BHTP) depth was set to 1900 m for all simulations despite the

different modelled injection intervals. The actual BHTP would need to be re-calculated for all depths except for the 1800 – 1900 m interval. Note that this is not influencing any other model parameters. The rock and leak-off properties used for the sensitivity analysis and the forward modelling scenarios are summarized in Table 3.1 and Table 3.2. Young's modulus measured in the laboratory  $E_{lab}$  was used for all simulations except for the upscaled forward modelling scenarios where it was reduced to  $E_{H-B}$ .

Depth (m)	Lithology	$S_{hmin}$ (MPa)	$E_{lab}$ (GPa)	$E_{H-B}$ (GPa)	$\nu$ (-)	KIC (MPa m <sup>1/2</sup> )
0 - 830	Volcanics	13.3	30.0	30.0	0.30	1.65
830 -1650	Marble	26.4	49.0	36.0	0.27	1.87
1650 - 1800	Skarn	28.8	49.0	35.9	0.13	2.31
>1800	Granodiorite	30.4	42.8	31.4	0.35	2.36
-	Sensitivity analysis	24.8	49.0	-	0.27	2

Table 3.1: Rock properties data for the sensitivity analysis and forward modelling scenarios.

Depth (m)	Lithology	$P_p$ (MPa)	$c_t$ (1/kPa)	$k$ (mD)	$\Phi$ (-)	$\mu_{Res}$ (mPas)	$\mu_{filt}$ (mPas)
0 - 830	Volcanics	7.2	1.45e5	0.001	0.05	0.1	0.5
830 -1650	Marble	14.3	1.02e5	0.001	0.04	0.1	0.5
1650 - 1800	Skarn	15.7	1.02e5	0.001	0.04	0.1	0.5
>1800	Granodiorite	16.5	1.02e5	0.001	0.02	0.1	0.5
-	Sensitivity analysis	16.0	1.02e5	0.001	0.03	0.1	0.5

Table 3.2: Leak-off parameter for the sensitivity analysis and forward modelling scenarios. Note that the permeability of the injection interval was set to zero.

## 3.4 Results and discussion

### 3.4.1 Sensitivity analysis

With a simple sensitivity analysis, we want to quantify how different variables impact the simulation results. For slurry rate, injection volume, fracture toughness and minimum horizontal stress this is summarized in Table 3.3. The results of the sensitivity analysis may be summarized as follows:

An increasing slurry rate slightly increases fracture length, height, and width. Additionally, the pressure is slightly increased. This is because in an impermeable formation the formation breakdown pressure is reached also with lower flow rates as no leak-off occurs. During fracture propagation the influence of the flow rate on the hydraulic fracturing result is still minor as long as leak-off from the hydraulic fracture surface into the formation is insignificant.

Instead, larger injection volumes significantly enlarge the hydraulic fracture while the pressures remain unchanged. How much fluid needs to be injected to achieve a certain fracture half-length for example depends strongly on the fluid leak-off and to a certain extent also on the elastic rock properties, which change the fracture aperture. Since we assume no leak-off in our model despite the relatively low viscosity fluid (water), the volumes required to reach a certain fracture dimension have to be considered as an absolute minimum. It is very likely that real hydraulic fractures are much shorter compared to the results in Table 3.3, largely due to leak-off through an existing fracture network.

The notable change in fracture length and height resulting from a variation of the fracture toughness  $K_{IC}$  highlights that rock mechanical parameters also need to be well investigated for the best possible a-priori design of hydraulic fracturing treatments. Leak-off and other rock mechanical properties were not investigated. In our model, the stress field did not influence the fracture dimensions, but only the bottomhole (and surface) treating pressures, which are much higher when a higher minimum principal stress is present in the target interval. Without knowledge of the stress field it is therefore not possible to estimate the pressures required for hydraulic fracturing. The maximum pressures need to be known to know which equipment to use for the treatment.

Note that these results are significantly different when a heterogeneous parameter distribution and leak-off would be considered as well.

	SR (m <sup>3</sup> /min)			V <sub>tot</sub> (m <sup>3</sup> )			K <sub>IC</sub> (MPa m <sup>1/2</sup> )			S <sub>hmin</sub> (MPa)		
	2	4	6	300	450	600	1.5	2	2.5	19.0	24.8	28.5
<b>L (m)</b>	540	542	543	538.25	617.68	680.92	548	538	529	538	538	538
<b>H (m)</b>	1081	1084	1085	1078	1236	1363	1096	1078	1058	1078	1078	1078
<b>w (cm)</b>	0.04	0.05	0.05	0.04	0.04	0.04	0.04	0.04	0.04	0.04	0.04	0.04
<b>P<sub>inF</sub> (MPa)</b>	1.11	1.12	1.12	1.09	1.09	1.09	1.09	1.09	1.1	1.09	1.09	1.09
<b>P<sub>surf</sub> (MPa)</b>	7.7	7.8	8.1	7.7	7.7	7.7	7.7	7.7	7.7	1.8	7.7	11.3
<b>BHFP (MPa)</b>	26.0	26.0	26.0	25.9	25.9	25.9	25.9	25.9	26.0	20.1	25.9	29.6
<b>BHTP (MPa)</b>	26.3	26.5	26.7	26.3	26.3	26.3	26.3	26.3	26.3	20.5	26.3	30.0

Table 3.3: Sensitivity analysis for injection parameters slurry rate (SR) and injection volume (V<sub>tot</sub>) and Mode I fracture toughness (K<sub>IC</sub>) as an example for a rock property.

### 3.4.2 Forward modelling scenarios

For the forward models total of 2500 m<sup>3</sup> of water was injected with a constant rate of 6 m<sup>3</sup>/min. A minimum horizontal stress gradient of 16 MPa/km was used and rock properties from laboratory data as summarized in Table 3.1 and Table 3.2 were applied. The results show an excessive fracture height growth and limited fracture length due to the stress increasing stepwise with depth (Table 3.4). This would be even worse if a linear stress gradient would be assumed (Lepillier and Hofmann 2020). However, this may be significantly different in reality as the stress does not increase linearly and the rock mass is not homogeneous. Heterogeneous stresses and rock properties would lead to significantly better height growth confinement as shown in Chapter 4.

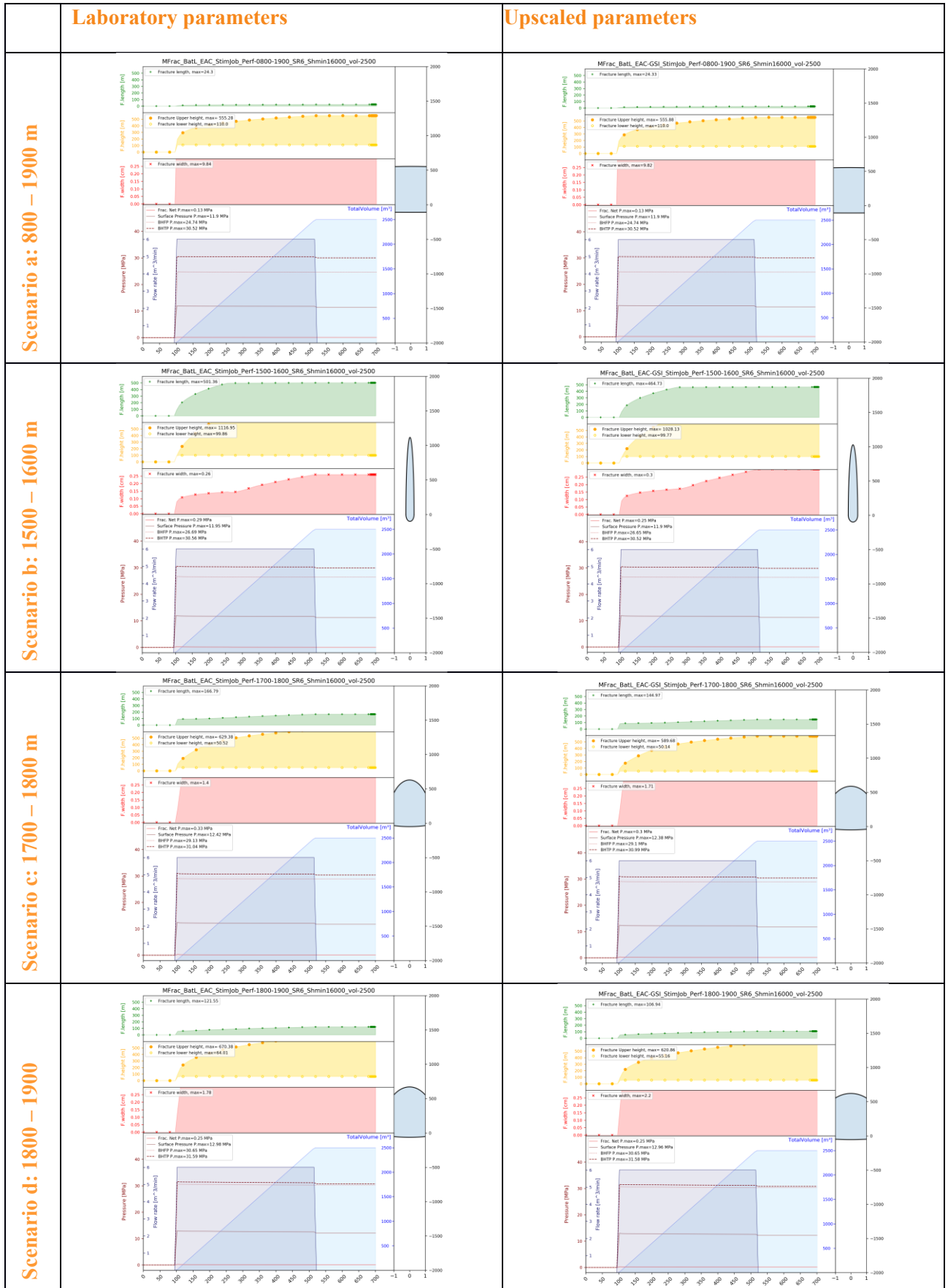


Table 3.4: Mfrac simulation results for the four forward modelling scenarios using laboratory rock properties.

### 3.5 Conclusions

This study shows that stimulation of an impermeable open hole well most likely focuses on the depth of the casing shoe, where in-situ stress is lowest. It also highlights that a hydraulic fracture would grow significantly upward if no height growth barrier in the form of stress contrasts, leak-off contrasts, strength contrasts or stiffness contrasts would exist.

## 4 Hydraulic and acid fracturing analysis of EAC-2 with MFrac

### 4.1 Introduction

In addition to the hydraulic fracturing scenarios discussed in Chapter 3, which were based on data from laboratory experiments of reservoir and outcrop samples, we performed MFrac simulations of well EAC-2 based on well log data and laboratory data. Such well logs were not available for EAC-1, but the results may be valid for both wells. Also, chemical stimulation is investigated here by simulating the injection of HCl together with the water to etch the fracture surfaces and permanently keep the hydraulic fracture open. Another difference is that leak-off was considered here as compared to Chapter 3.

### 4.2 Methodology

The simulations were performed with the commercial hydraulic fracturing simulator MFrac Suite 13 (Baker Hughes 2019). Compared to Section 3.2, we only add a short description of the additional features used for the simulations presented here. These include well logs, acid fracturing, and calculation of thermal and water fronts. The reader is referred to Baker Hughes (2019) for details on the theoretical background.

First, minimum horizontal stress, Young's modulus, Poisson's ratio, reservoir pressure, permeability and porosity were imported from available well logs of EAC-2 from 803 to 1394 m. Note that Young's modulus and Poisson's ratio from these logs are dynamic values and the minimum horizontal stress was computed for the case of normal faulting and hydrostatic pressure of (cold) water, which are different assumptions as compared to Section 2.2. However, using log data here, as compared to laboratory data in Chapter 3, allows to appreciate the influence of heterogeneity on hydraulic fracture development. Total compressibility was calculated based on the available logs. All of this data was then discretized into 1000 individual zones. All other parameters were either constant for the whole model, when no data was available, or set for the individual rock types based on laboratory experiments. MFrac was used for 3D hydraulic fracturing and acid fracturing simulations and the produced water reinjection simulator MPwri was used to calculate the thermal and water fronts.

First, injection at four different depth intervals is simulated including the target intervals defined later (Figure 39). Second, the volume and time required to achieve a fracture half-length of 300 m is calculated for different flow rates and the resulting fracture properties are described. Third, the volume and time required to achieve shorter or longer fractures with the same flow rate of 50 l/s are derived. Fourth, the influence of acid concentration and diffusivity on fracture conductivity and width is shown. Fifth, the influence of multiple parallel (or branching) fractures on the properties of the main fracture is simulated for up to 10 fractures. Finally, the important role of the minimum horizontal stress gradient is highlighted.

### 4.3 Model setup

The MFrac models were run in design mode with linear reservoir coupling, harmonic fluid loss model, acid treatment type, empirical wellbore hydraulics model, 1 minute maximum time step size, 30 iterations and heat transfer option. The fracture geometry was 3-dimensional, flowback and fracture closure were simulated,

fracture fluid gradient was included, default fracture growth, standard fracture friction model and no wall roughness or tip effects were used. The fracture initiation interval was calculated based on the minimum stress interval.

For EAC-2, rock properties (Figure 5) and leak-off parameters (Figure 6) were imported from well logs and laboratory experiments. The well was cased until 800 m (156.3 mm inner diameter) and open from 800 to 1900 m (149.2 mm inner diameter), which was also defined as the target zone and perforated interval for the base case scenario. The open hole section was mimicked by 2000 perforations with 76.2 mm diameter.

The Rock/Acid System R/A01 (Limestone / Nierode Data.HCL-L) was selected with the following characterization parameters: acid specific gravity of 1.5, acid molecular weight of 36.47, heat of reaction of 0 kcal/g mol, dissolving power of 1.37 mass rock/mass acid and the following acid properties: reaction order of 0.22, reaction rate coefficient of  $0.000527 \text{ (g mol/cm}^3\text{)}^{(1-n)}\text{cm/s}$ , activation energy of 15.2 kcal/g mol, reference temperature of 338.7 K, diffusivity of  $1\text{e-}4 \text{ cm}^2\text{/s}$ , and activation energy of 0 kcal/g mol. Acid concentration at inlet of 28%, acid concentration at equilibrium of 1.8% and diffusivity multiplier of 0.01 were used for the base case scenario. Additional acid data were a conductivity damage factor of 0.2, a fracture closure stress of 40 bar, a rock embedment strength of 3000 bar, an in-situ acid temperature of 150°C, a carbonate specific gravity of 2.71, an average carbonate porosity of 0.02 and a fraction of non-reactive fines of 0.

Heat transfer was modelled with a base fluid type and in-situ fluid type of water, a reservoir lithology of limestone, an average porosity of 0.02, a mean formation temperature of 150°C and an injection fluid inlet temperature of 20°C. For multiple fracture development a full fracture interaction and fluid loss interaction was assumed.

For the MPwri simulations thermal stresses were included, but poroelastic stresses were excluded. The layer temperature was specified assuming a temperature gradient of 150°C/km and the coefficient of thermal expansion was assumed to be  $1\text{e-}7 \text{ 1/}^\circ\text{C}$ . Thermal/Water front data were set to water as injection fluid, limestone as reservoir lithology, and water as in-situ fluid. A minimum reservoir height of 200 m and a reservoir half-length of 500 m were selected, resulting in a drainage area of 100 ha.

In the base case scenario 1062 m<sup>3</sup> of water with 28% HCl were injected at a constant rate of 50 l/s for 354 minutes.

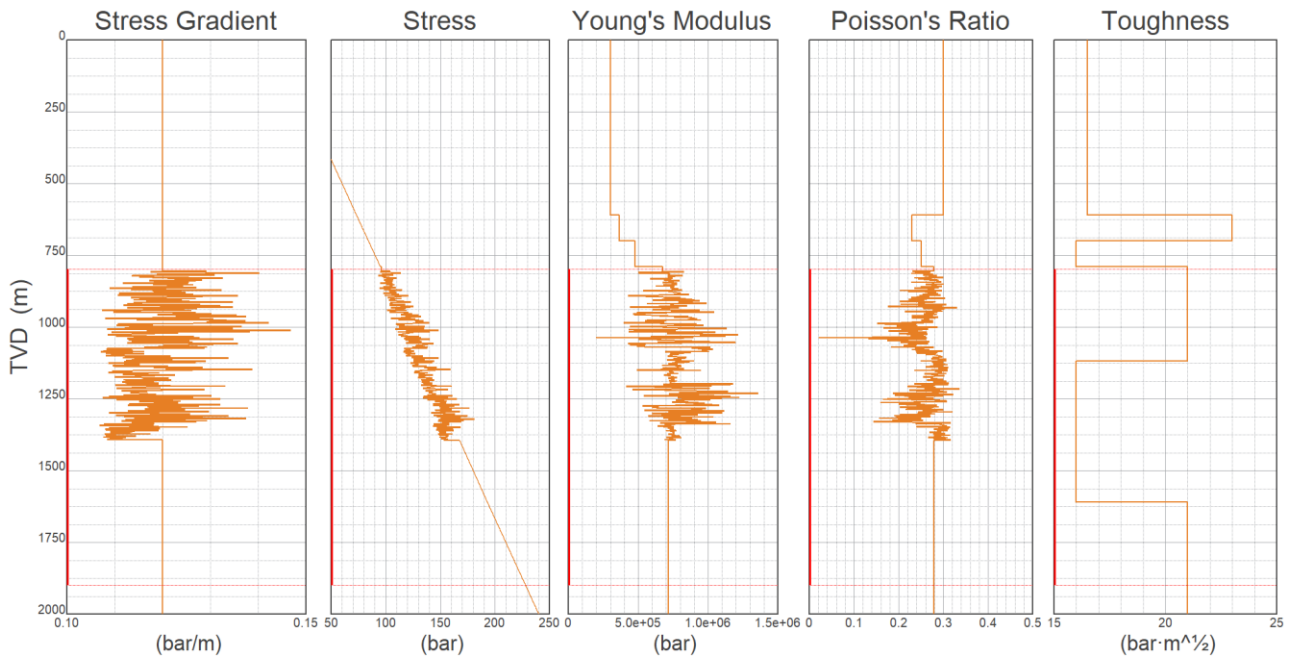


**Figure 5: MFract rock properties based on well logs in EAC-2 and laboratory experiments. Laboratory data was used for the formations where no well log data was available.**

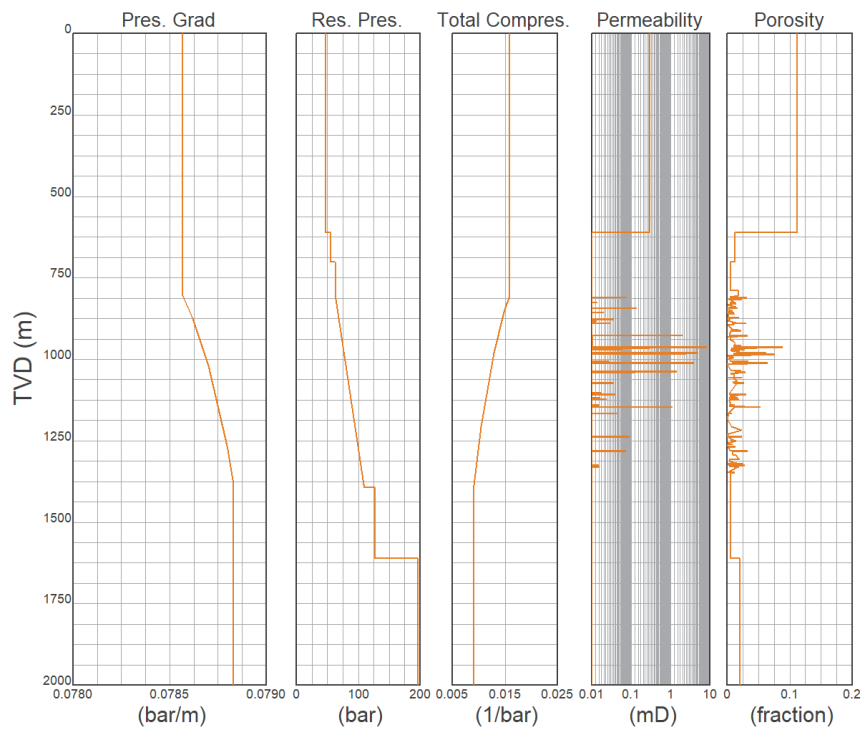


**Figure 6: MFract leak-off parameters based on well logs in EAC-2 and laboratory experiments (where no well log data was available). Fluid viscosity of reservoir fluid and filtrate fluid were set constant to 0.3 mPas and wall building coefficient  $C_w$  of 5000 cm/min<sup>1/2</sup> (equivalent to no filter cake) and spurt loss coefficient of 0 cm were assigned to the whole model.**



## 4.4 Results and discussion

### 4.4.1 Hydraulic fracturing scenarios at different depths

First, we simulated the injection of 1062 m<sup>3</sup> of water at a constant injection rate of 50 l/s in four different depth intervals. This results in a fracture half-length of 300 m in the base case scenario (Figure 8). Since a hydraulic fracture without proppants or acids would close again after injection, 28% HCl (1.8 % of which are non-reactive) with a diffusivity of 1e-6 cm<sup>2</sup>/s were added to simulate the fracture conductivity at the end of the hydraulic fracturing job. This influences fracture width and conductivity only.

In Scenario 1 the open hole interval is defined from 800 to 1100 m, forcing the hydraulic fracture to initiate within the skarn at ~875 m, 75 m below the casing shoe (Figure 7). The fracture tends to grow upward but seems to be restricted to the interface to the volcanic layer starting at 610 m, which has a higher leak-off compared to the underlying limestones, marbles and skarns. With a fracture half-length of 162 m and total fracture height of 368 m fracture the total height/total length ratio is ~1.1. If a variable stress profile based on well logs below 800 m could have been generated the fracture height growth may be less. The fracture aperture is increased at lower depths with lower stress and lower stiffness.

Scenario 2 is the base case scenario for all simulations. It simulates the stimulation of the whole open hole section from 800 to 1900 m (Figure 8). Hydraulic fractures initiate at ~1125 m, at the interface between skarn and marble. Fracture height growth is well confined to 227 m by the stress differences calculated from the well logs. With a fracture half-length of 300 m the total height/total length ratio is ~0.4. Fracture aperture is highly variable within the fracture due to the heterogeneous well log information. This Scenario is considered the most realistic one, as it is the only one where well log information was available for the whole fracture growth interval and since the open hole section of the well is simulated as it is. However, due to the lower stresses below the casing shoe the fracture initiation point may actually be shallower and more similar to Scenario 1.

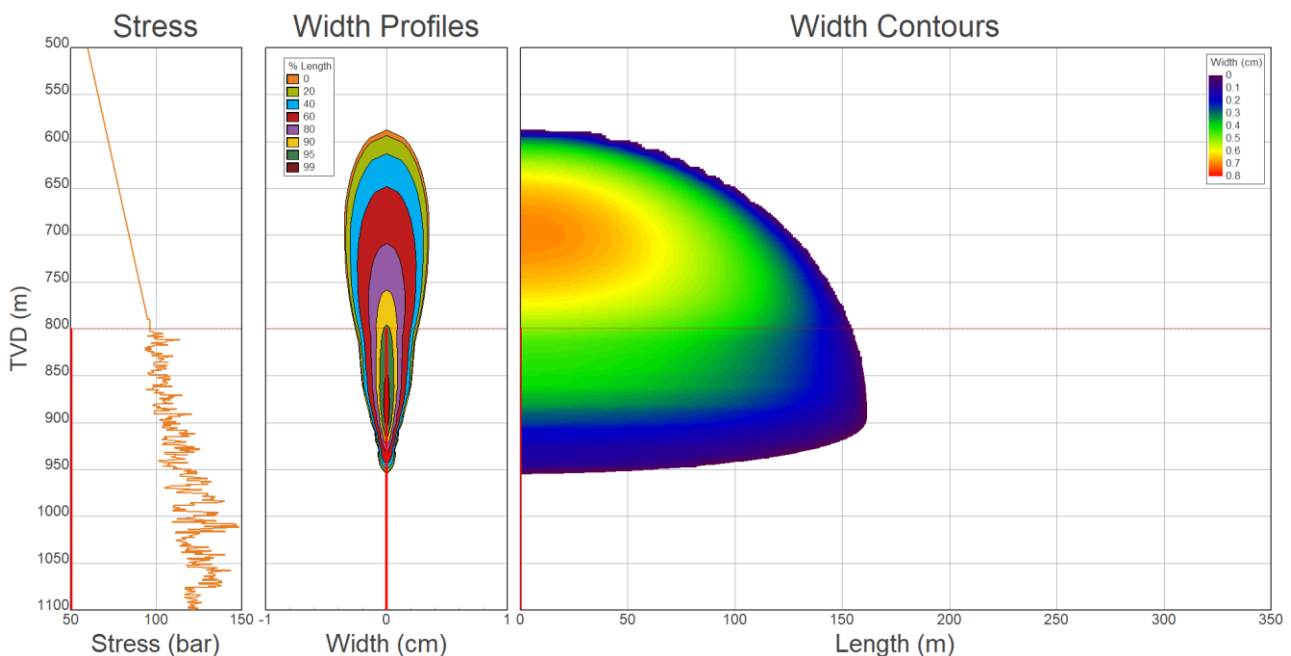


**Figure 7: Scenario 1 - Hydraulic fracture geometry at the end of injection (before closure) resulting from injection of 1062 m<sup>3</sup> water at 50 l/s below the casing shoe (open hole interval 800 – 1100 m) in EAC-1.**

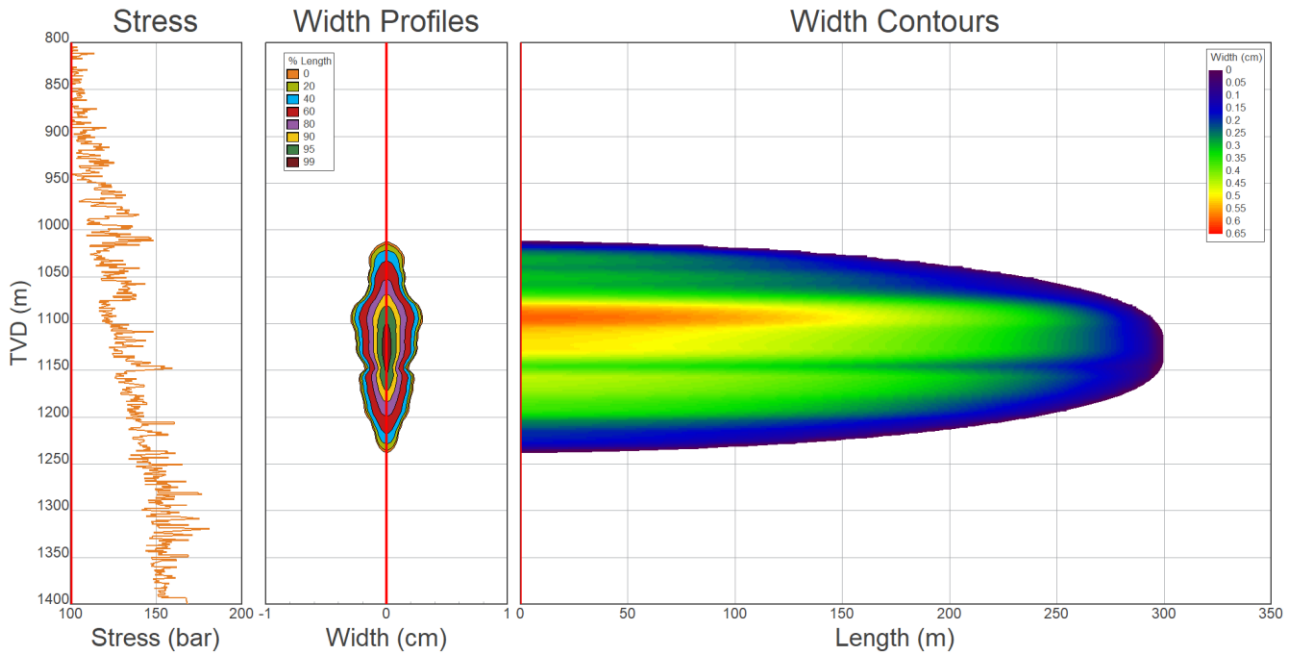


**Figure 8: Scenario 2 (base case) - Hydraulic fracture geometry at the end of injection (before closure) resulting from injection of 1062 m<sup>3</sup> water at 50 l/s below the casing shoe (open hole interval 800 – 1900 m).**

In Scenario 3 the injection interval was restricted to the marbles at 1500 – 1700 m, one of the deeper stimulation target zones identified earlier (Figure 39). Since no well log information was available the stress profile was assumed to be linear at this depth interval, which leads to significant fracture height growth (613 m) and a limited fracture half-length of 84 m (total height/total length ratio of ~3.6; Figure 9). With the available information no fracture height growth barriers are present and the target zone is not efficiently stimulated due to excessive fracture height growth.

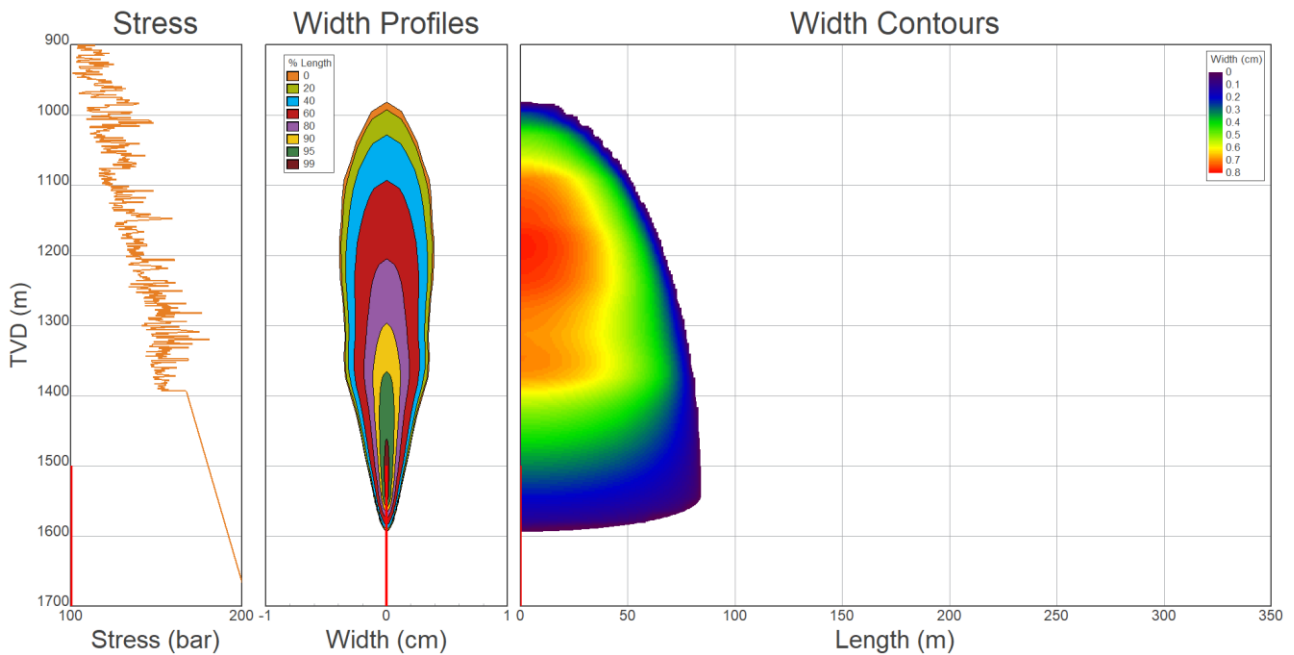


**Figure 9: Scenario 3 - Hydraulic fracture geometry at the end of injection (before closure) resulting from injection of 1062 m<sup>3</sup> water at 50 l/s below 1500 m (open hole interval 1500 – 1900 m).**

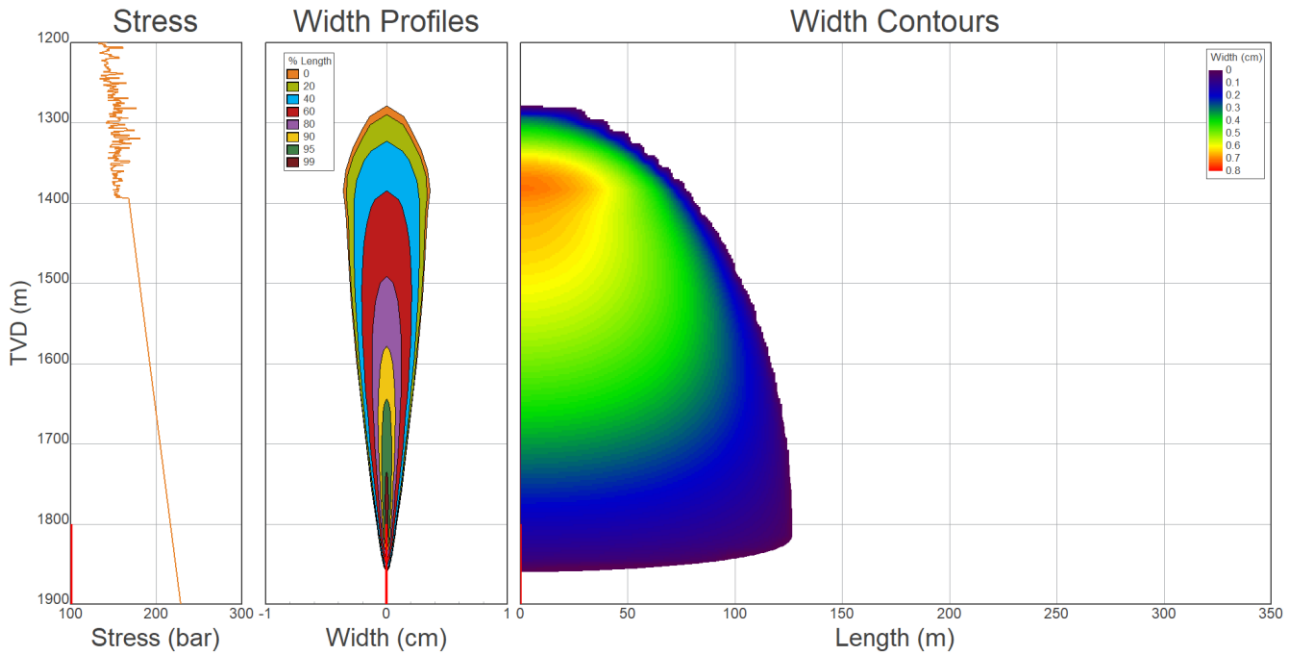


**Figure 10: Scenario 4 - Hydraulic fracture geometry at the end of injection (before closure) resulting from injection of 1062 m<sup>3</sup> water at 50 l/s below 1800 m (open hole interval 1800 – 1900 m).**

In Scenario 4 the injection interval was restricted to the granitic rock at 1800 – 1900 m, the second deeper stimulation target zone identified earlier (Figure 39). Like Scenario 3, fracture height growth is significant (582 m) and fracture half-length is limited to 127 m (total height/total length ratio of ~2.3; Figure 10) and the target zone could not efficiently be stimulated.

#### **4.4.2 Influence of injection rate on treatment parameters, fracture geometry, fracture conductivity and thermal and water fronts**

Stimulation of low permeability rock, as encountered in both Acoculco wells, does not require high flow rates to build up the required pressures to hydraulically fracture the rock. However, leak-off from a hydraulic fracture face into the formation increases with increasing fracture size, which reduces the fracture efficiency. Figure 11 shows the injection volume and time required to develop a hydraulic fracture of 300 m half-length in the base case scenario (Scenario 2) and the resulting total fracture height, average fracture width and fracture efficiency. With increasing flow rates less fluid needs to be injected in a shorter duration of time because the fracture efficiency increases. While the fracture height slightly increases, the fracture width is significantly reduced with increasing flow rate. This is due to the lower amount of HCl injected in these scenarios as the total injection volume is lower. Without acid, the fracture width slightly increases with increasing flow rate.

The fracture conductivity profiles at the end of injection for these different flow rate scenarios is shown in Figure 12. It can be seen that the 12 m from the fracture tip are not affected by the acid and that the lowest injection rate (with the highest amount of HCl) delivers the highest fracture conductivity and propped fracture half-length.

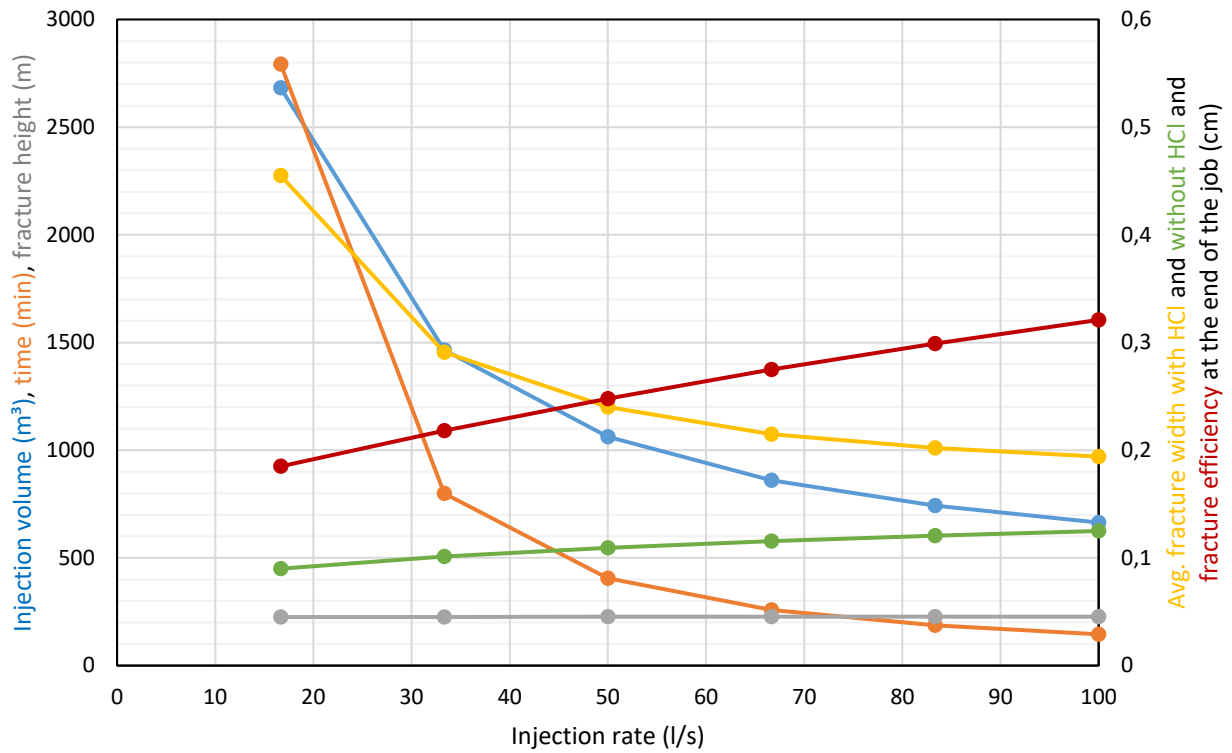


Figure 11: Treatment parameters volume and time required to achieve a fracture half-length of 300 m in Scenario 2 (base case) and resulting fracture height and width at the end of the treatment (before fracture closure) for different water injection rates.

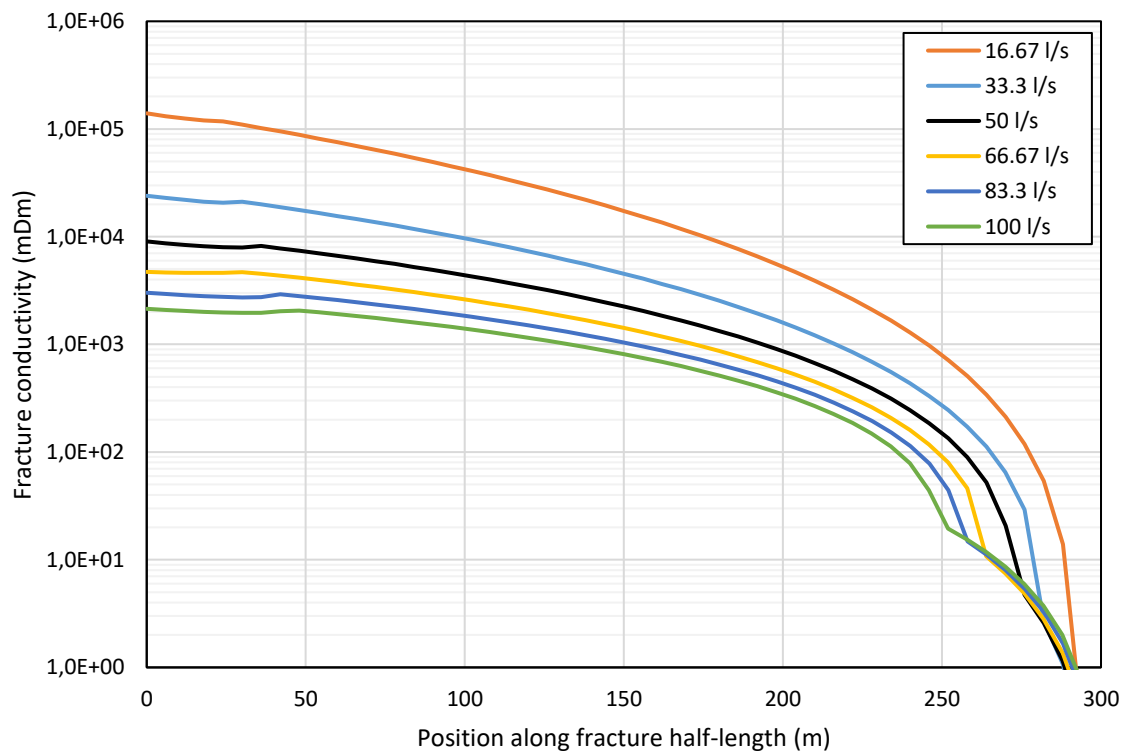
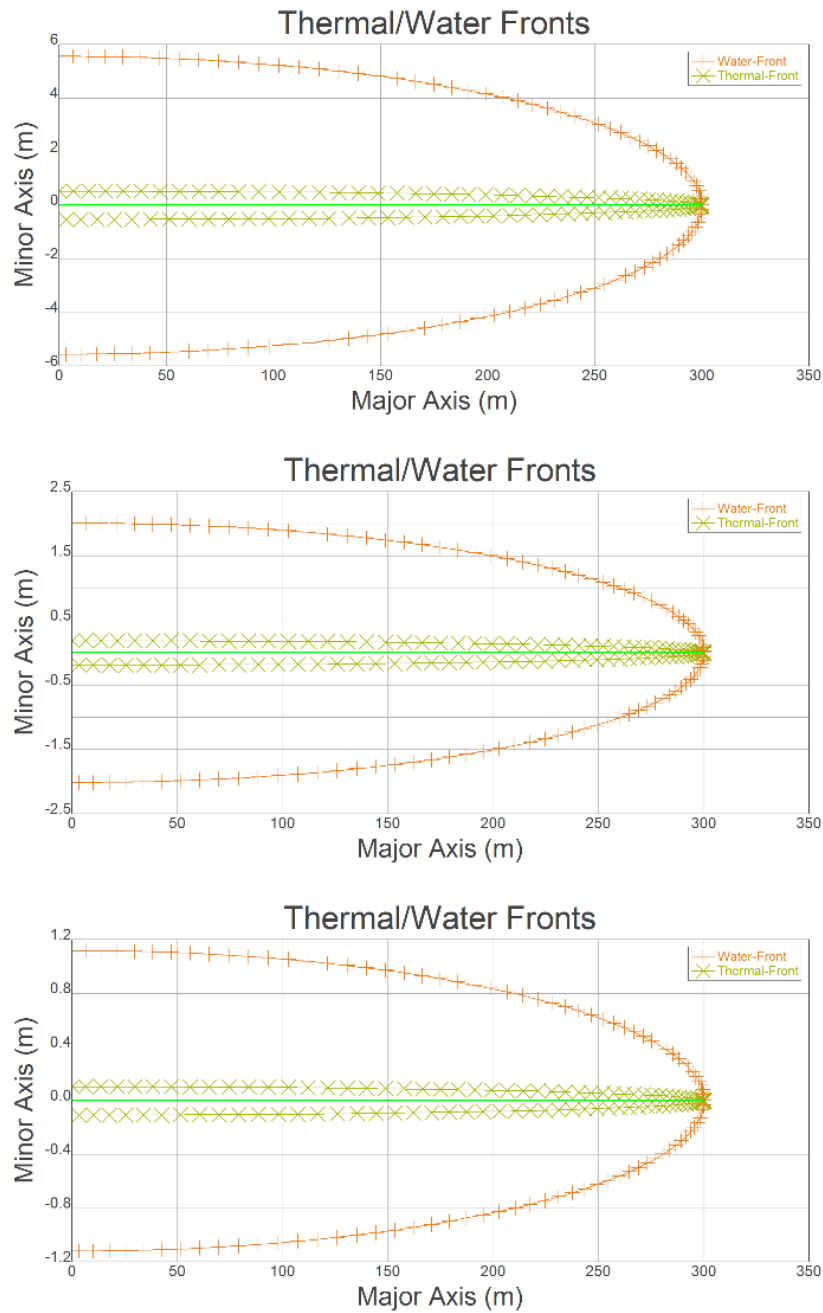


Figure 12: Fracture conductivity along one fracture wing at the end of the treatment (before closure) resulting from the different flow rate scenarios to achieve a fracture half-length of 300 m in Scenario 2 (base case).

Injection of cold water into the hot formation results in fluid and heat diffusion from the fracture into the formation. The resulting thermal and water fronts for different injection rates are shown in Figure 13. The water front reaches  $>5$  m away from the fracture for the lowest flow rate/highest injection volume scenario (16.67 l/s) and only slightly  $>1$  m for the highest flow rate/lowest injection volume scenario (100 l/s). The same trend is seen for the thermal front, while the thermal influence during the stimulation is limited to  $<0.5$  m from the fracture wall in all cases. Thus, roughly a fluid volume of  $>2500$  m<sup>3</sup> needs to be injected for multiple days in order to affect a rock volume of  $>10$  m surrounding the hydraulic fracture for the base case scenario. For a significant thermal area of influence these numbers would need to be at least one order of magnitude higher since heat conduction is a very slow process.



**Figure 13: Top view of thermal and water fronts of one fracture wing resulting from injection with 16.67 l/s (top), 50 l/s (center), 100 l/s (bottom) until a fracture half-length of 300 m is reached.**

#### 4.4.3 Injection parameters required to achieve different fracture half-lengths and influence on fracture geometry

Larger fracture half-lengths obviously require larger volumes of injection fluid and longer treatments. The required volume and time to achieve different fracture half-lengths with 50 l/s constant injection in Scenario 2 (base case) is quantitatively shown in Figure 14 (left). The larger amount of HCl resulting from the larger water volumes would lead to a linear increase in fracture width and the fracture height growth is restricted to ~225 m for half-lengths of up to 425 m. Continued injection leads to slight out-of-zone fracture growth (Figure 14, right).

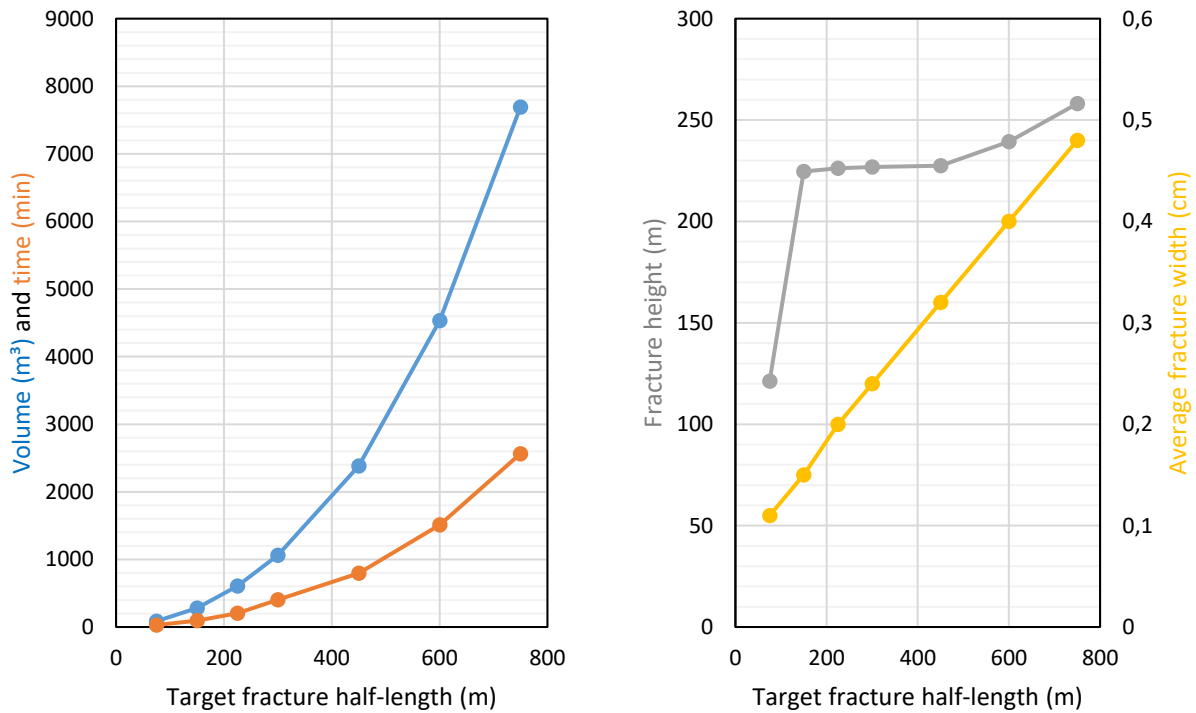


Figure 14: Treatment parameters (left) and fracture dimensions (right) at the end of the treatment (before closure) for different target fracture half-lengths when injecting water at 50 l/s in Scenario 2 (base case).

#### 4.4.4 Influence of acid diffusivity and concentration on fracture conductivity and width

Using HCl to dissolve calcite and other minerals would require a detailed planning of an acid stimulation, which is beyond the scope of this section. Nevertheless, we show the influence of HCl concentration, equilibrium conditions and diffusivity on the resulting fracture conductivity in Figure 15 and width in Figure 16. This allows to better judge the simulation results. It can be seen that a low diffusivity in the order of  $1e-6$  cm²/s or less is required for the HCl to be transported with the water along the fracture and react with the fracture wall along the whole fracture surface. Higher diffusivities result in chemical reactions occurring only close to the well. In field applications the diffusivity can be changed by using different injection fluids, for example. Comparing the 15% HCl and 28% HCl case shows that by varying the HCl concentration the final fracture conductivity can be adapted. The 1.8% HCl equilibrium conditions mean that 1.8% of the HCl are not reacting with the rock. Since this is a relatively low value, its influence on the final result is negligible. Figure 16 shows how the acid etches an additional fracture width into the open fracture, which would result from injection without acid. After injection, the fracture would close again completely without acid, while the additional etched fracture width would remain open.

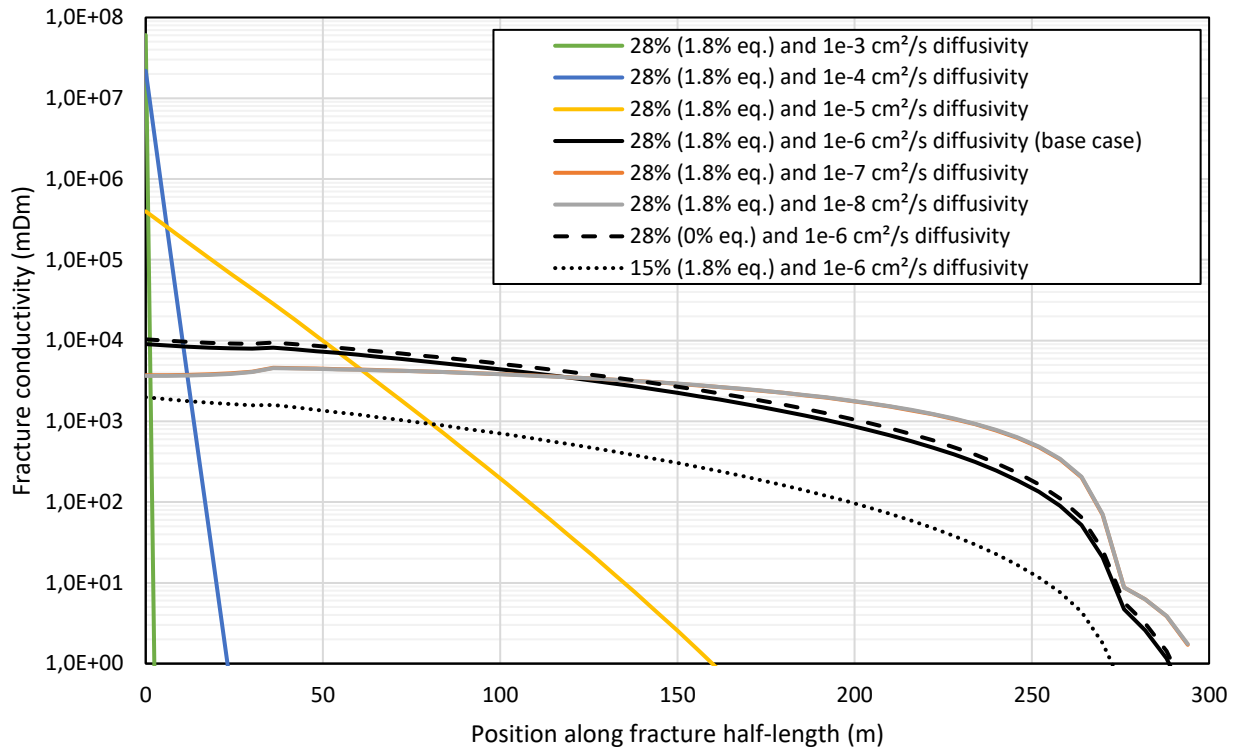


Figure 15: Fracture conductivity along one fracture wing at the end of the treatment (before closure) resulting from different HCl concentrations, equilibrium (eq.) concentrations and diffusivities.

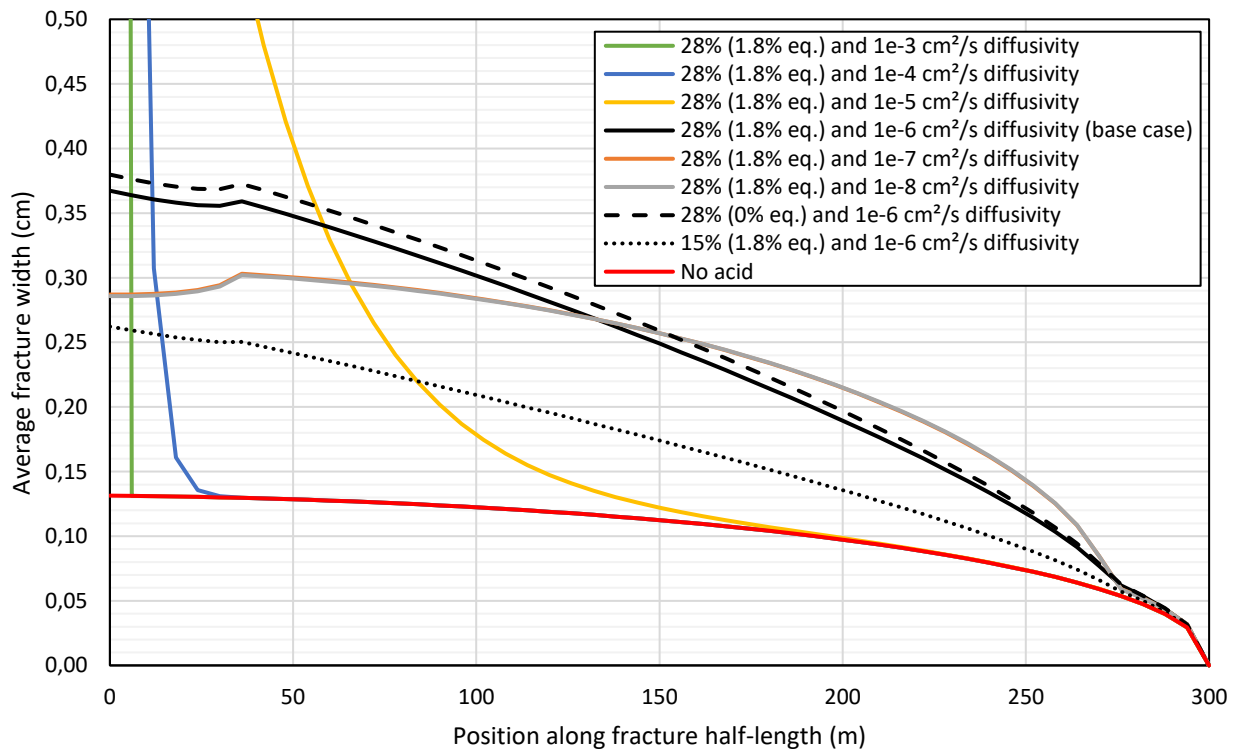


Figure 16: Average fracture width along one fracture wing at the end of the treatment (before closure) resulting from different HCl concentrations, equilibrium (eq.) concentrations and diffusivities compared to the fracture width without acid.

#### 4.4.5 Influence of multiple fracture growth on fracture dimensions

In case multiple hydraulic fractures would initiate and develop at the same time and thus a fracture network would be stimulated, the injected fluid would be distributed to the whole fracture network and the individual fractures would interact with each other hydraulically and poroelastically. As a result, the main fracture would become shorter when the same treatment parameters are used. This is shown in Figure 17 for the base case scenario and different number of fractures.

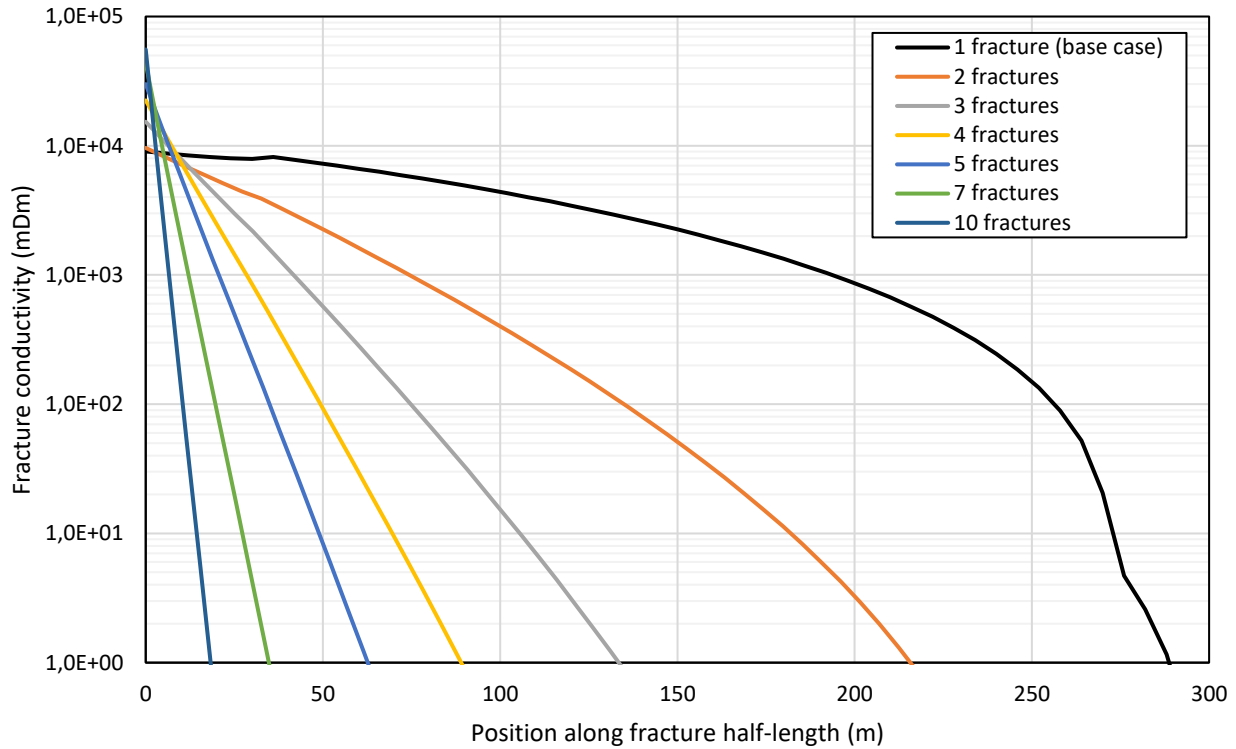
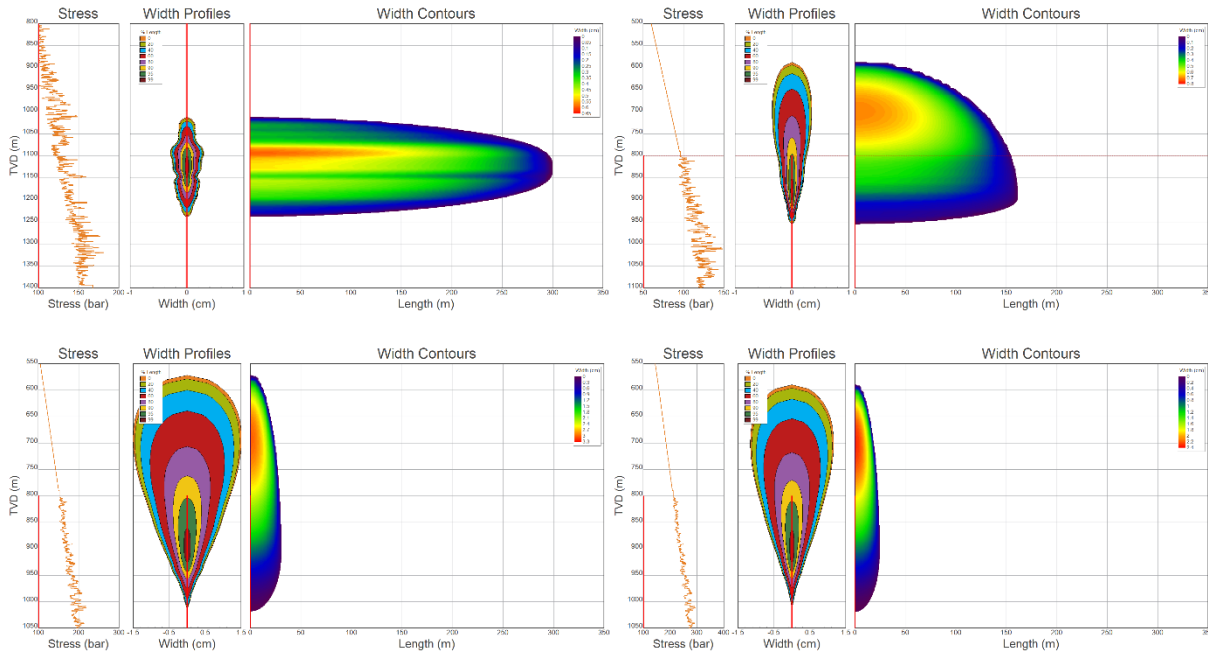


Figure 17: Fracture conductivity along one fracture wing at the end of the treatment (before closure) resulting from multiple parallel fracture growth compared to the base case scenario where only one single hydraulic fracture develops.

#### 4.4.6 Influence of stress gradient on fracture dimensions

The investigated Scenarios are based on a relatively low minimum horizontal stress gradient of  $\sim 12$  MPa/km (120 bar/km), which is based on well logs. However, the minimum horizontal stress gradient may be much higher. To show how significant the stress gradient affects the simulation results, two more simulations were run with stress gradients of 19.2 MPa/km (192 bar/km) and 26.4 MPa/km (264 bar/km), respectively (Figure 18). In both scenarios fracture height growth is excessive, and fractures become very short. Thus, an efficient stimulation of the target intervals would not be possible.





**Figure 18: Hydraulic fracture geometry at the end of injection (before closure) resulting from injection of 1062 m<sup>3</sup> water at 50 l/s in the open hole interval 800 – 1900 m with a stress gradient of 12.0 MPa/km (top left), 19.2 MPa/km (bottom left), and 26.4 MPa/km (bottom right), and below the casing shoe (open hole interval 800 – 1100 m; top right).**

## 4.5 Conclusions

Different hydraulic fracturing scenarios have been simulated with the commercial hydraulic fracturing software MFract. It was shown that >300 m long hydraulic fractures can be developed if fracture height growth is contained by barriers resulting from heterogeneous rock properties and stresses. A larger volume of hydraulic influence may be achieved by injecting large amounts of water for a long time at a low injection rate, but the volume of thermal influence remains significantly smaller. Injection should be stopped if excessive fracture height growth is observed or when the target fracture half-length is reached. Adding HCl to the injection fluid may result in permanent etched fracture width, which is strongly influenced by the diffusivity of the HCl and its concentration.

## 5 Analytical and numerical analysis of hydraulic fracturing and fracture re-opening

This chapter is based on the manuscript “Modeling fluid re-injection in a stimulated geothermal reservoir” by Francesco Parisio and Keita Yoshioka (submitted to Geoscience Letters).

### 5.1 Introduction

Hydraulic stimulation in geothermal reservoirs has certain peculiarities: i) proppants are almost never employed (one of the few exceptions is Legarth et al. 2005) zonal isolation is rarely applied (exceptions are for example Zimmermann et al. 2010, Petty et al. 2013, Bendall et al. 2014) because of either packer's limitations at higher temperature and/or concerns about sealing existing fractures (feed zones) by cementing and iii) stimulation is often carried out within the basement rocks that pose a greater risk of inducing earthquakes. In EGS stimulation, pure mode-II fracture propagation is unlikely and the propagation of new tensile fractures in mode-I is the key component in the hypothesis of mixed-mechanism stimulation where newly created fractures interact with pre-existing ones (McClure and Horne 2014). At Acoculco, the low

permeability hints toward a low matrix permeability and mostly sealed natural fracture networks, which implies that mode-I propagation through the rock mass is the most likely mechanism of stimulation.

Without pumping proppants or any chemical additives and after the injection, fractures will close up to the minimum aperture that rock asperities can hold. Because of fluid extraction during EGS operation, the depleted formation will further decrease the permeability of fractures and ultimately hinder fluid flow. Overall, successful heat extraction depends mostly upon the residual permeability that is achieved during stimulation. Without isolation and/or selective stage control, the state of the stress or weak spots (pre-existing fractures, faults, or bedding planes) determine the initiation and propagation of hydraulic fractures. In poorly fractured formation, such as Acoculco, a planar fracture whose normal direction coincides with the least stress is expected to grow. Finally, to maximize the energy output, EGS are usually stimulated in the hotter and deeper part of the reservoir in 3-5 km depth in the low permeable crystalline basement. Such depth corresponds to an increased seismogenic potential and to minimize the risks of inducing large magnitude earthquakes (Terakawa et al. 2012, Ellsworth et al. 2019), relatively low flow rate and limited injection pressure must be applied (Brown 2009, Chabora et al. 2012, Garcia et al. 2016, Matsunaga et al. 2015, Schill et al. 2017). The goal of this contribution is to study the stimulation effects at Acoculco. In particular, we aim at characterizing the hydro-mechanical response of water re-injection in a previously stimulated fracture. We use a combination of analytical and numerical methods: whilst the former are robust tools to study the involved mechanisms and give indications about preliminary design of stimulation methods (Garagash and Detournay 2000, Detournay 2016, Dontsov 2016), the latter allow us to explore complex scenarios and reduce the number of hypotheses and simplifications to be made (McClure and Horne 2014, Hofmann et al. 2016a, Yoshioka and Bourdin 2016, Lecampion et al. 2018).

## 5.2 Methodology

Firstly, we study the propagation of a pure mode-I fracture in the intact rock and analyse the influence of temperature and flow rate in hydraulic-fracture growth. Secondly, we use a numerical approach based on the finite element method with enriched discontinuities (Watanabe et al. 2012) to study the effects of re-injection in the newly created fracture in the reservoir.

### 5.2.1 Fluid-driven fracture propagation

We employ the theory of fluid driven crack-propagation in porous media (Figure 19), which considers a penny-shaped fracture that propagates quasi-statically in a permeable, linear elastic medium and is driven by a pressurized incompressible Newtonian fluid (Savitski and Detournay 2002). The fracture propagates on the normal plane to a uniform far-field stress in mode-I (Savitski and Detournay 2002). The well radius is negligible compared to the radius of the fracture  $R(t)$  and the elliptic fracture opening profile  $w(r)$  taken along the radial coordinate depends on time  $t$ . The porous medium behaves accordingly to linear elastic fracture mechanics (LEFM) and is characterized by the Young's modulus  $E$ , the Poisson's ratio  $\nu$ , the critical fracture toughness  $K_{IC}$  and the leak-off coefficient  $C_l$ . The fluid has a dynamic viscosity  $\mu$  and is injected at the center of the fracture at a constant volumetric flow rate  $Q_0$ . Boundary conditions are applied at the inlet and at the tip of the fracture. The conventional hypotheses applied to the problem are: i) the fluid is injected from a point source; ii) there is no-lag between the fracture tip and the fluid front; iii) the fracture propagates continuously in mobile equilibrium; iv) the fluid flow follows lubrication theory; v) the effect of gravity is neglected; vi) the stress intensity factor at a crack tip does not increase with crack length. The elasticity equation of the porous solid controls the crack opening based on the fluid pressure. The condition for fracture propagation states that a fracture propagates if the mode-I stress intensity factor equals the critical value  $K = K_{IC}$ . The boundary conditions are no tangential flow and zero width at the crack tip and a prescribed flow rate at the crack mouth (injection). Fluid-driven fracture propagation theory provides an estimate of fracture length and width at the

end of the stimulation treatment. For details of the mathematical implementation the reader is referred to the original paper by Parisio and Yoshioka (submitted).

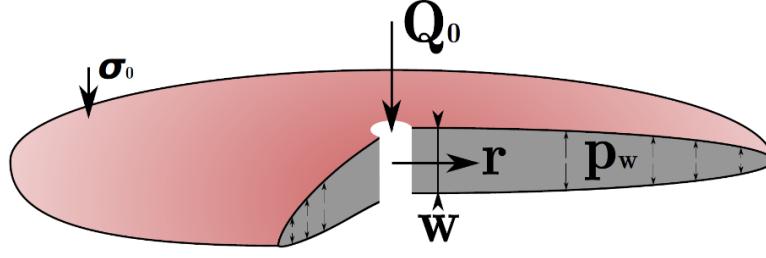


Figure 19: Penny-shaped fluid driven fracture in an elastic porous medium.

### 5.2.2 Lower interface elements for re-injection modelling

Simulations were performed with coupled hydro-mechanical finite elements analyses using the object-oriented open source platform OpenGeoSys (Bilke et al. 2019). The fracture created in the first stage (stimulation) is modeled as a local enrichment at the element boundaries applying a Lower-dimensional Interface Element (LIE) (Watanabe et al. 2012), in a formulation which shares some similarities with the Extended Finite Elements Method (Yoshioka et al. 2019).

The governing equations of the coupled hydro-mechanical problem in porous media are derived from the linear momentum conservation equation and the mass balance equation. For details of the mathematical description, numerical implementation and text examples the reader is referred to the original paper by Parisio and Yoshioka (submitted), Watanabe et al. (2012) and Yoshioka et al. (2019).

## 5.3 Model setup

As a potential scenario, stimulation is to take place in the lower 200 m of one of the two Acoculco wells (between 1800 and 2000 m) through open hole hydro-fracturing in the granite formation (Lorenzo-Pulido et al. 2010, Calcagno et al. 2018). Given the stress regime in the field (Normal or strike-slip faulting), we expect a vertical fracture to form within this interval, initiating at the casing shoe (at the lowest stress) unless any weakness (natural fracture or bedding plane) pre-exists.

The constant geothermal gradient is 0.13 K/m, indicating that heat transfer in the system is mainly conductive. The pore pressure gradient is hydrostatic accounting for the density variation with temperature and pressure (depth). The hydromechanical material parameters of the granite are taken from literature (Lepillier et al. 2019) and are  $E = 43$  GPa,  $\nu = 0.35$ ,  $\Phi = 0.028$  and  $K_{IC} = 2.41$  MPa m<sup>1/2</sup>. The isotropic permeability is very low, i.e.,  $k = 10^{-19}$  m<sup>2</sup>, which makes the rock essentially impermeable.

### 5.3.1 Fluid-driven fracture propagation

We assumed two case scenarios for stimulation: i) a first case in which the fluid is assumed to be in thermal equilibrium with the rock (hot fluid) and ii) a second case in which the fluid is assumed to remain the wellhead temperature during injection (cold fluid). The properties of the fluid for the hot injection are taken at temperature and pressure at 1900 m depth, i.e.,  $p = 16.7$  MPa and  $T = 298$  °C so that the fluid has the viscosity  $\mu = 9.1 \times 10^{-5}$  Pa s, the specific density  $\rho_w = 793$  kg/m<sup>3</sup>, enthalpy  $h = 1397.3$  kJ/kg and the compressibility  $\beta_w = 2.46 \times 10^{-9}$  1/Pa. The properties of the fluid for the cold injection scenario are computed for  $T = 20$  °C and  $p = 16.7$  MPa. The two cases serve the purpose of investigating the effects of the fluid rheology on hydraulic-fracture propagation conditions: we are not accounting for effects induced by temperature variations such as

thermo-elastic strains or thermal expansion of water. The injection flow rate for the base case is  $Q_0 = 0.1 \text{ m}^3/\text{s}$  and a stimulation time of  $T = 20$  minutes is considered for a total injected volume of  $120 \text{ m}^3$ .

### 5.3.2 Re-injection modelling

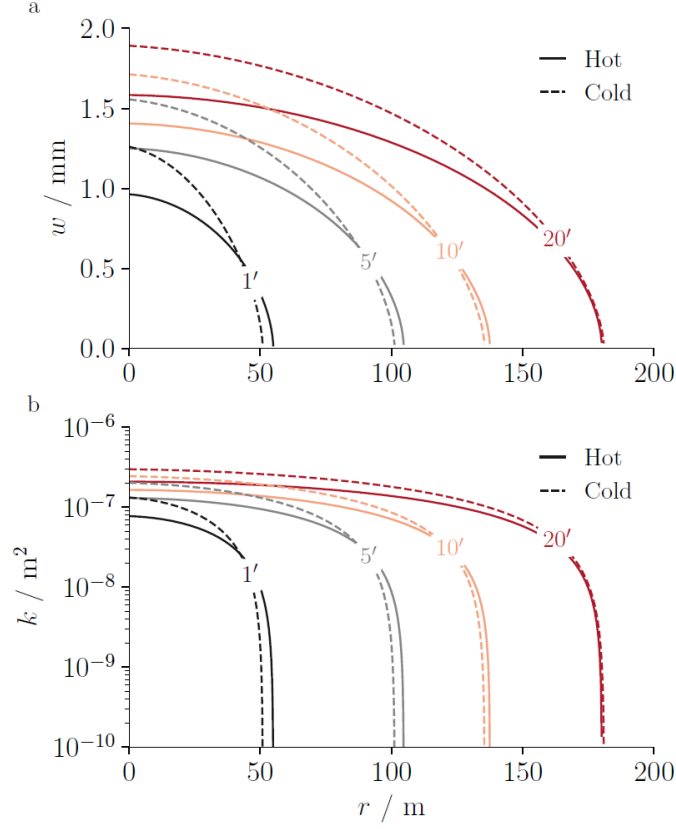
In the second phase of the study, we assume that a fracture of a given length is created in the reservoir and has closed to an aperture of  $0.1 \text{ mm}$  after the stimulation. We investigate the consequences of fluid re-injection in terms of fracture re-opening and pressurization by using the LIE-FEM approach with a fixed size fracture. We have analyzed different scenarios, in which i) a short-term ( $\sim 10^3 \text{ s}$ ) re-injection is performed in a closed crack, ii) a longer ( $\sim 2 \times 10^4 \text{ s}$ ) re-injection is performed on a closed crack and iii) a longer re-injection ( $\sim 2 \times 10^4 \text{ s}$ ) is performed on a crack connected at its tip with a highly permeable fracture network, which is simulated as a constant pore pressure boundary equal to the reservoir initial pore pressure, i.e., free-flow conditions. We assume a shear stiffness of  $k_s = 0.01 \text{ GPa/m}$  and a normal stiffness of  $k_n = 0.1 \text{ GPa/m}$ .

## 5.4 Results

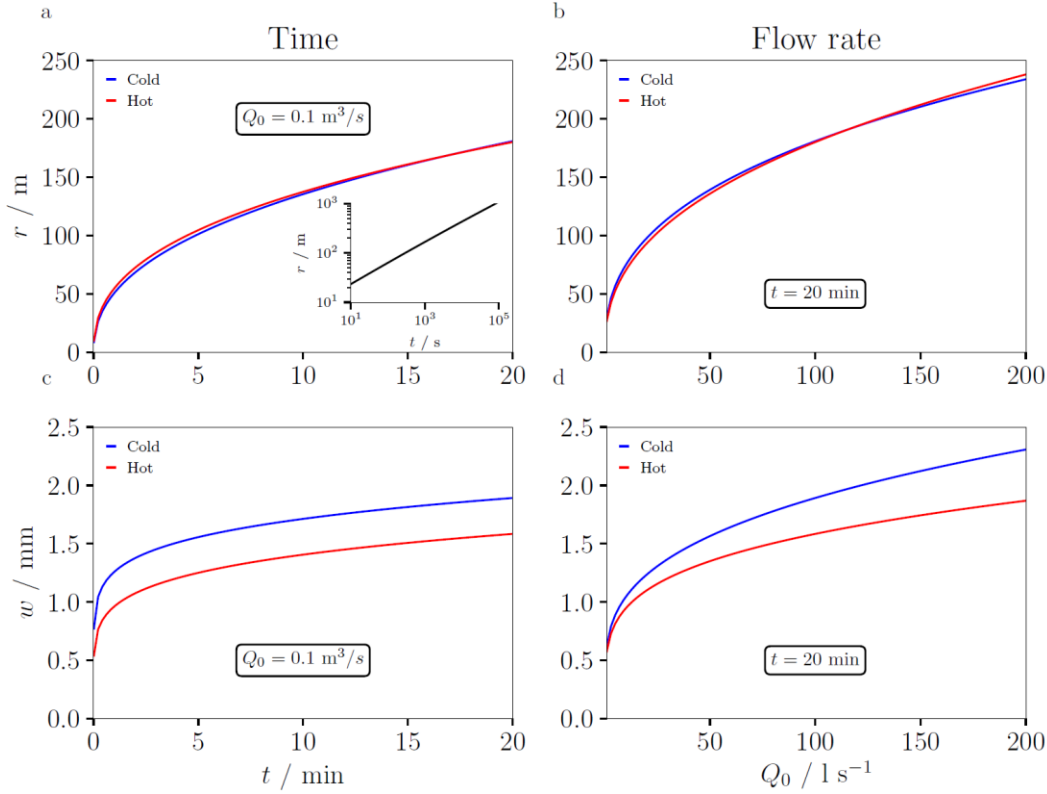
### 5.4.1 Hydraulic fracturing scenarios

Figure 20 shows the results of the stimulation in terms of fracture width (a) and permeability (b) evolution with time for the two case scenarios. Injecting hot fluid generates a lower fracture width at the injection point compared to cold fluid and the fracture radius is slightly larger in early times while it is almost identical after 20 minutes of injection (Figure 20a). The lower fluid viscosity of the hot case injection implies a smaller flow resistance, hence a lower pressure decrease along the crack radius. The difference between the two cases reduces with time, since fluid-driven fracture problems transition with time from the viscous to the toughness regime, in which viscous forces are a secondary control with respect to the fracture resistance. The reduced opening in the lower viscosity case is related to the higher matrix leak-off, since Carters leak-off coefficient is inversely proportional to viscosity (more fluid is transferred from the fracture to the porous matrix). The fracture permeability increases with time (Figure 20b) and the difference between the two scenarios is marginal. The increase of permeability at the injection point is about 5 times between 1 and 20 minutes of injection for both cases. As permeability is a quadratic function of the width, the value drops by 3 to 4 orders of magnitude at the fracture tip where the width tends to zero following a power-law asymptote of exponent  $1/2$  for the toughness regime and  $2/3$  for the viscous regime. At the end of the stimulation, the maximum fracture radius achieved is in the order of  $\sim 180 \text{ m}$ .

Following the base case scenario, we investigate the evolution of the fracture radius and the maximum fracture width at the injection point (Figure 21a and c) in time and the effects of different flow rate (Figures 3b and 3d) at a fixed time (20 min). The fracture radius is insensitive to the temperature of the fluid. It increases rapidly in the early time and tends to stabilize with lower growth rate toward the end of the injection. In other words, propagating a radial fracture becomes more energetically expensive at longer time. A similar observation can be made for the fracture width at the injection point, which shows an even quicker response in the early time and a stable opening toward longer time. On the contrary, the width is sensitive to the fluid's temperature. The final fracture radius is proportional to the flow rate with a rapid increase up to roughly  $100 \text{ l/s}$  and a shallower slope thereafter. The fracture width at the injection point is sensitive to the combination of flow rate and fluid viscosity: the difference between the two curves in Figure 21d increases at higher injection rate.



**Figure 20: Evolution of hydraulic fracture width (a) and permeability (b) with time for hot and cold water injection.**



**Figure 21: Evolution of hydraulic fracture radius (a) and width (c) at different times for  $Q_0 = 0.1 \text{ m}^3/\text{s}$  and for different flow rates (b, d) after 20 minutes of injection when injecting hot and cold fluid.**

### 5.4.2 Fracture re-opening scenarios

We have investigated the re-opening of a fracture created by a hydraulic fracturing job during re-injection. The fracture is assumed to be 180 m of radius with an initial opening of 100  $\mu\text{m}$ . Figure 22a shows the case of rapid re-injection with step-wise increase of the injected flow rate in an isolated crack: i) the pressure rapidly increases during re-injection and as a consequence the crack re-opens; ii) the crack re-opening increases the permeability and reduces the over-pressure by increasing storage. During continuous and constant flow rate re-injection (dotted line) the pressure monotonically decreases and reaches relatively quickly a steady state, which is temporary. If the injection continues for a prolonged time (Figure 22b), the opening reaches an equilibrium with the deformation of the surrounding rock contrasting the pressure inside the crack. The pressure response shows a minimum at which the crack is completely filled with fluid.

Once the crack is filled, continuous injection starts pressurizing the crack further, with a linear slope that is a function of the whole system compressibility and a step-wise increase in the flow rate from 25 l/s to 40 l/s has a minimum effect in terms of pressure response. If the crack is connected with a permeable fracture network that offers no resistance to flow, no pressurization occurs as the injected fluid can escape with no resistance other than frictional viscous forces (dotted line in Figure 22b).

Comparing the fracture pressurization evolution at longer times shows that after  $\sim 4$  days, the pressure within the fracture has reached the total far field stress ( $\sigma_0 = 50$  MPa), a tensile state develops at the fracture tip which will eventually overcome the tensile strength and the fracture will re-propagate (light blue line in Figure 22c). Comparing results against the case of a 930 m long crack (reached after approximately 10 days of initial stimulation) shows a short delay of the pressurization response for the longer initial crack (dotted black line in Figure 22c). Pressurization increases linearly in the log-log plot with a slope that is almost independent on the fracture length.

The crack width profile during continuous re-injection shows no difference between the non-connected case (Figure 22d, solid line) and the connected case (Figure 22d, dots) in the early times, i.e., when the crack is not filled and pressurized yet. Once the crack approaches the beginning of re-pressurization, the response between the two cases starts to diverge, with the width of the connected crack being smaller than the non-connected one. The connected crack is more difficult to pressurize once the fluid has reopened the crack entirely, as evidenced by the width (Figure 22d) and the pressure (Figure 22e) profiles along the crack.

During short-time re-injection, step-wise increase in the flow rate generates additional over-pressure and crack re-opening, which then reduces accordingly the pressure with time. Figure 23a-h shows on the left the evolution the deformed FEM model ( $10^4$ -times amplified) with crack width and pore pressure at different instants of time; the different time instants of the contour map are shown on the right as points in the time vs pressure curve from Figure 22a (step-wise injection increase). The crack initially opens as a consequence in the over-pressure, which is also transmitted to the rock matrix. At the crack tip, because of equilibrium conditions stemming from Linear Elastic Fracture Mechanics (LEFM), the pressure decreases to values lower than the initial pressure. During injection (Figure 23a-d), the crack tip advances and the width increases all along its profile; after shut-in at 60 l/s (Figure 23e-h), the crack tip continues to advance as the pressure quickly decays with time and the fluid redistributes toward the crack tip. As a consequence of the fluid re-distribution, the width decreases at the injection point while increasing toward the tip (crack re-opening) as a pressure signal traveling along the crack.

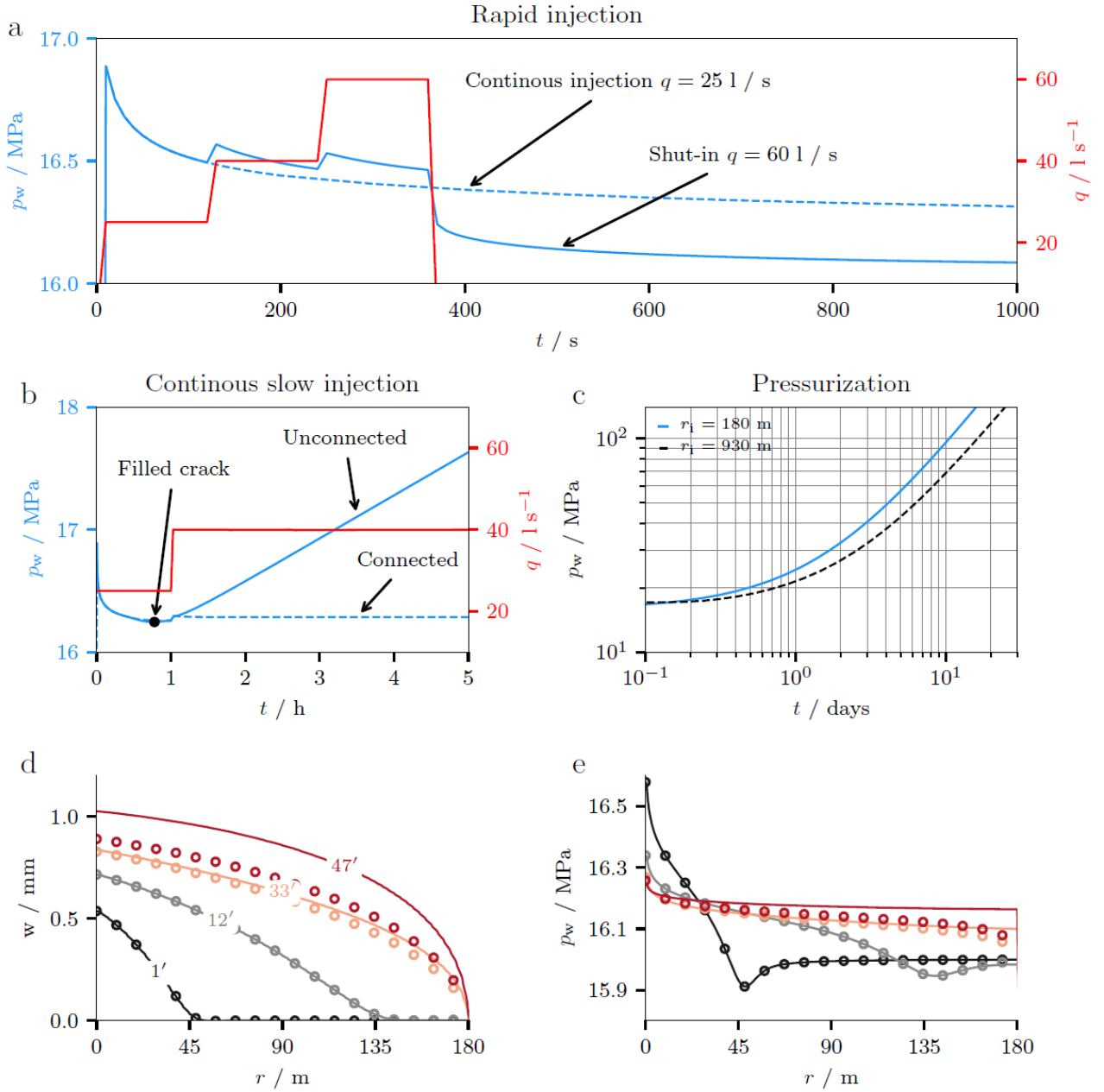


Figure 22: A rapid injection case (a) shows the initial pressure decay as a consequence of re-opening the existing crack, while continuous long-term injection will later pressurize the crack to failure (c), unless the crack is connected to a permeable fracture network (b). The width profile (d) along the crack at different time shows the different pressurization efficiency for the connected and non-connected case. A similar argument can be drawn for the pore pressure profile (e).

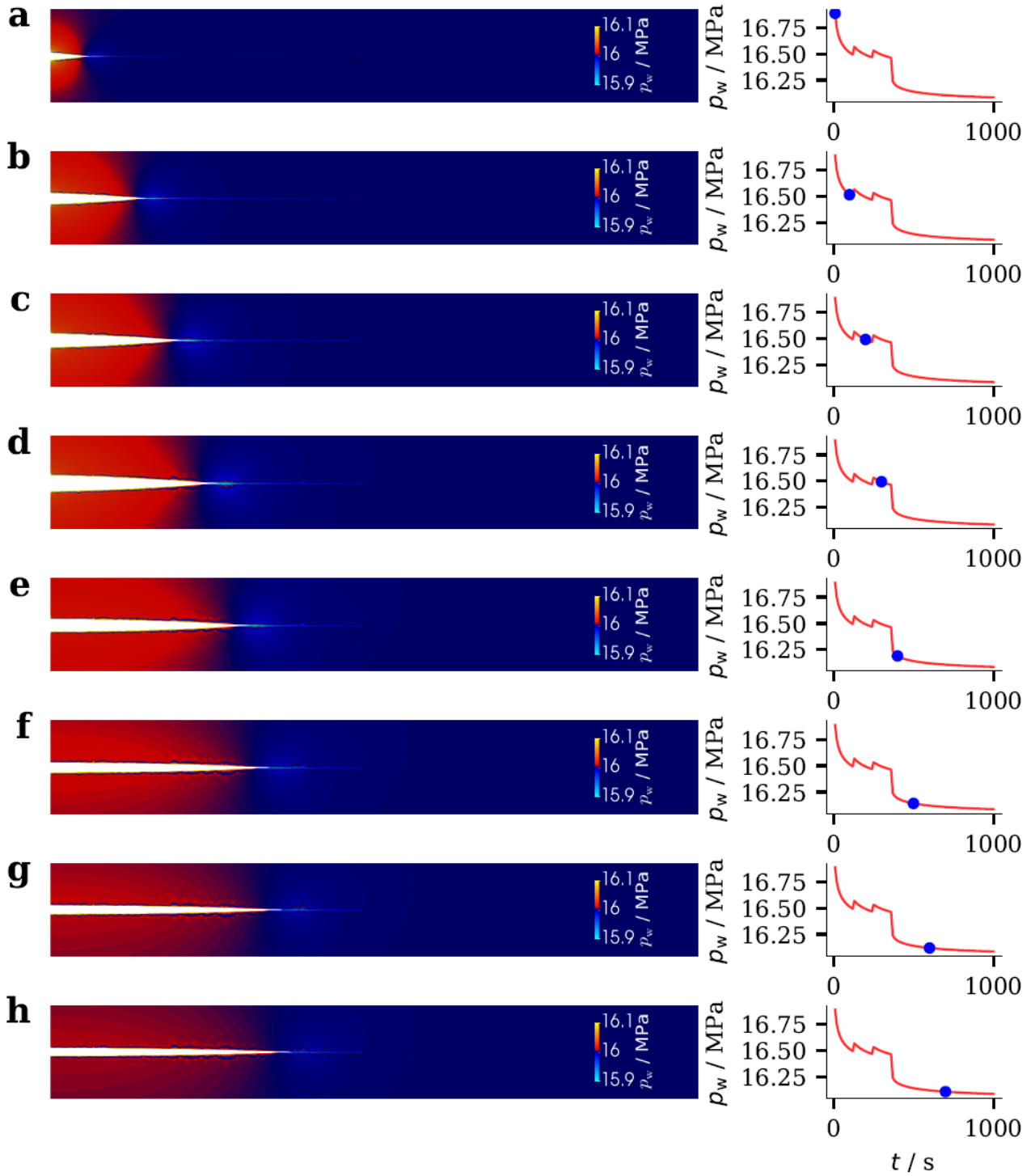


Figure 23: Deformed contour map of pressure during short-time water injection with variable flow rate at different time steps. The time instances are indicated as points in the time vs. pressure curve on the right side of each contour map.

## 5.5 Discussion and conclusions

We have shown that the fluid rheology plays a role in fracture propagation by affecting leak-off and viscous dissipation: the viscosity decreases with increasing fluid temperature, leading to increasing leak-off and decreasing fluid flow resistance. Based on our analyses, we conclude that the temperature of the injected fluid plays a minor role in the propagation behavior of the fracture. Flow rate and time (volume) of the stimulation



procedure instead play a dominant role in determining the final fracture length and its opening profile which, in turn, affects the fracture permeability.

After the stimulation performed at high injection rate, the fracture will close, and the permeability decreases by several orders of magnitude. FEM analyses have shown that fluid re-injection will re-open the existing fracture and pressure will decay with time as the fracture re-opens. When the fracture is filled with fluid, continuous injection further pressurizes the fracture at a rate that is a function of the system compressibility (fracture + water + rock matrix). If the fracture is non-connected, the pressurization will continue and the injectivity is a decreasing function of time (even after some re-propagation). On the other hand, if the fracture is connected to a highly permeable network, the pressurization will stop and the injectivity reaches a constant and time-independent value.

Our analyses have shown that isolated fractures are unlikely to create the suitable conditions for geothermal development: during injection, the crack will quickly fill in the order of hours as the storage space is in this case limited. For a successful exploitation of the geothermal reservoir, it is imperative that the newly created fracture find a permeable network. One way to achieve a maximum connectivity is zonal isolation (Yoshioka et al. 2015). Injection into a long section of open hole or slotted liner will likely initiate a fracture at the least resistance point (either the least stress or pre-existing weakness) and every sub-sequence fluid re-injection will redirect the fluid within the more permeable fracture. The fracture is then quickly filled and injectivity will decrease with time. Prolonged stimulation is not an effective strategy, because the gain in additional storage space marginally shifts the pressurization time and tensile fracturing is delayed by only ~20 days. Furthermore, prolonged stimulation in a closed fracture increases drastically the over-pressure, posing a great risk of triggering unabated dynamic ruptures in critically stressed faults (Garagash and Germanovich 2012, Elsworth et al. 2019).

Zonal isolation will instead impose to create multiple fractures within a given section of the borehole, increasing the probability of intersecting and connecting to an existing network of fractures. Connectivity is crucial to avoid excessive pressurization and to create an adequate flow path in the reservoir by connecting the stimulated fractures with the existing ones.

In summary, we found that hydraulic stimulation in the low-permeable crystalline basement is likely to produce large fractures with a radius of ~200 m, but if such fractures do not intersect pre-existing permeable structures or a second wellbore (unconnected), the overall injectivity remains insufficient for successful geothermal exploitation. Target-oriented drill paths and zonal isolation combined with multi-stage stimulation are the most promising techniques to increase the chance of intersecting natural fractures and connecting them.

## **6 Analysis of hydraulic stimulation of pre-existing fracture network with OpenGeoSys**

This chapter is based on the paper “Variational Phase-field modelling of hydraulic fracture interaction with natural fractures and application to Enhanced Geothermal Systems” by Baptiste Lepillier, Keita Yoshioka, Francesco Parisio, Richard Bakker, and David Bruhn (submitted to JGR: Solid Earth, under review).

### **6.1 Introduction**

Successful hydraulic stimulation in Acoculco depends critically on the permeability increase of pre-existing fractures. Even when a hydraulic fracture initiates from the wellbore it will interact with the pre-existing fracture network. In this chapter, hydraulic fracture initiation, propagation and interaction with natural fractures is simulated using a two-dimensional variational phase-field model implemented in OpenGeoSys.

## 6.2 Methodology

OpenGeoSys is a free open-source software ([www.opengeosys.org](http://www.opengeosys.org)). Recently, a variational phase-field approach (Alessi et al. 2018; Chukwudozie et al. 2019; Yoshioka et al. 2019) has been implemented in the FEM code. Fracture development is based on linear elastic fracture mechanics and the criterion for fracture propagation is that the mechanical energy restitution rate  $G$  equals to the critical surface energy release rate  $G_c$ . The two-dimensional model assumes plane-strain conditions.

The discrete fracture network (DFN) representing the natural fractures in the reservoir is derived from scanline measurements on outcrop analogues of Acoculco (Lepillier et al. 2020). These measurements were extrapolated using the multiple point statistic method (Bruna et al. 2019). As a result, three different DFNs are retrieved, representing limestone, marble and skarn, respectively. Each of the DFNs is a two-dimensional georeferenced section of 600 x 600 m<sup>2</sup> (Figure 24). From this, three smaller sub-domains of 100 x 100 m<sup>2</sup> are extracted. Each sub-domain is then rotated to align the model boundaries with the principal stress directions.

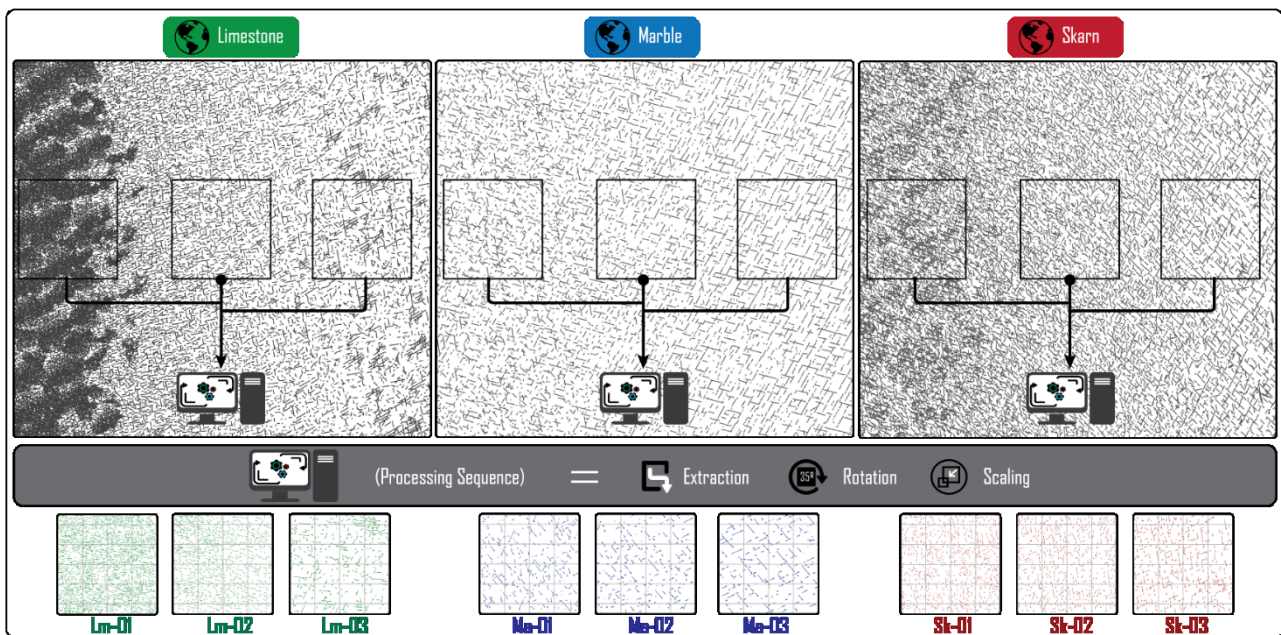


Figure 24: Pre-processing methodology from reservoir scale to extracted, rotated and scaled DFNs used for the phase field simulations.

## 6.3 Model setup

Elastic properties, strength and critical energy release rate of the modelled lithologies are based on laboratory experiments on analogue outcrop samples. The model parameters for the different lithologies are summarized in Table 6.1. The natural fractures of the DFN are assumed to be cemented and hydraulically closed before stimulation. Fracture toughness and critical strain energy release rate of natural fractures are assumed to be 10% of the value of the surrounding rock matrix. The rock matrix is assumed to be impermeable and has no porosity. No a priori hydraulic fracture length was implemented in the model, but hydraulic fractures initiate from a borehole (injection point). A normal faulting stress regime is assumed with a maximum horizontal stress direction of N56°E. Minimum and maximum horizontal stress magnitudes of 20 MPa and 21 MPa, respectively, were chosen. The model consists of a regular mesh with 25 cm element size.

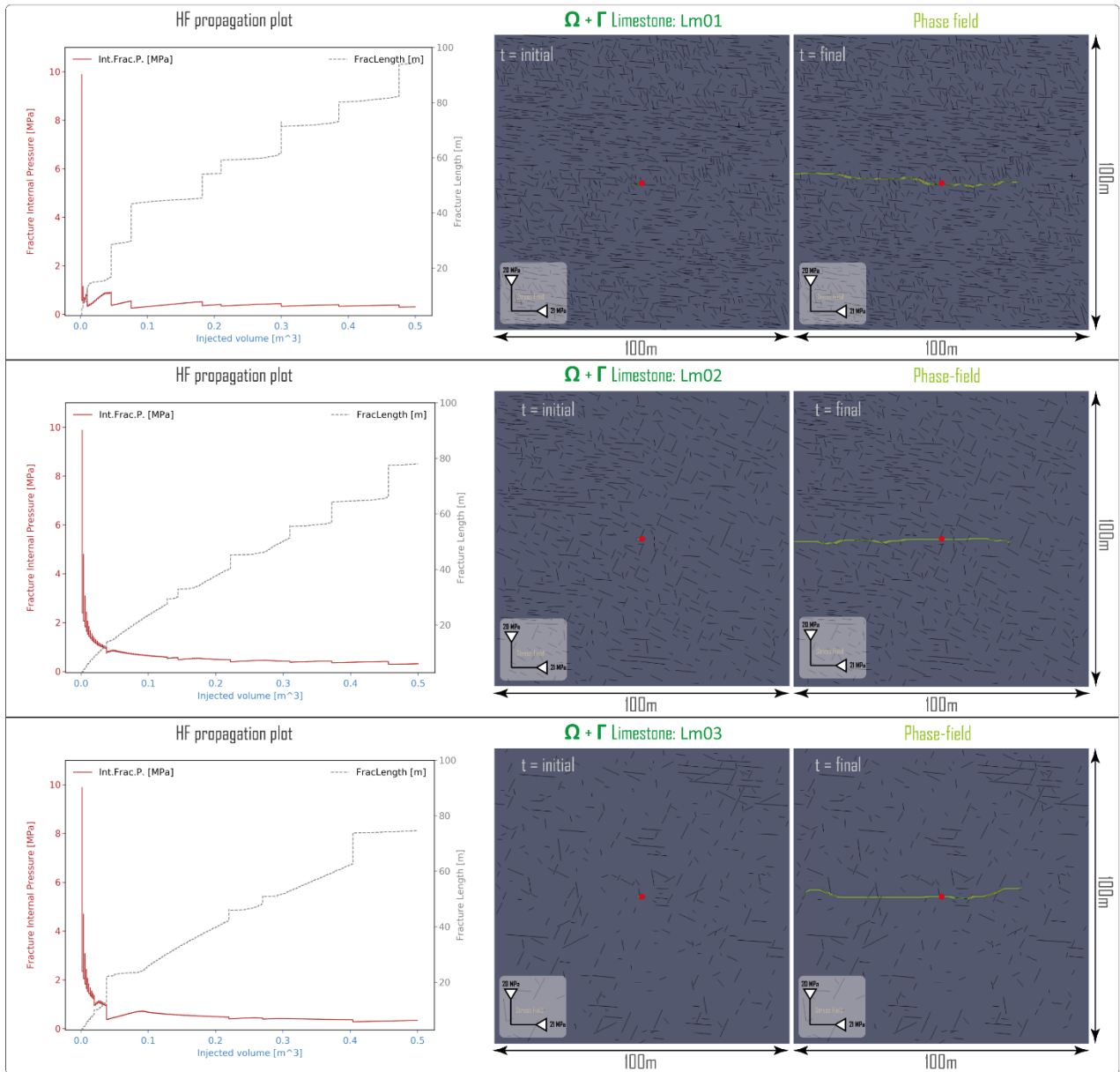
Lithology	E (GPa)	$\nu$ (-)	$K_{IC}$ (MPa m <sup>1/2</sup> )	$G_c$ (Pa m)
Limestone	37.9	0.27	2.63	182.0
Marble	49.2	0.27	1.87	71.4
Skarn	49.0	0.13	2.31	108.0

Table 6.1: Input parameters for the OpenGeoSys phase field models.

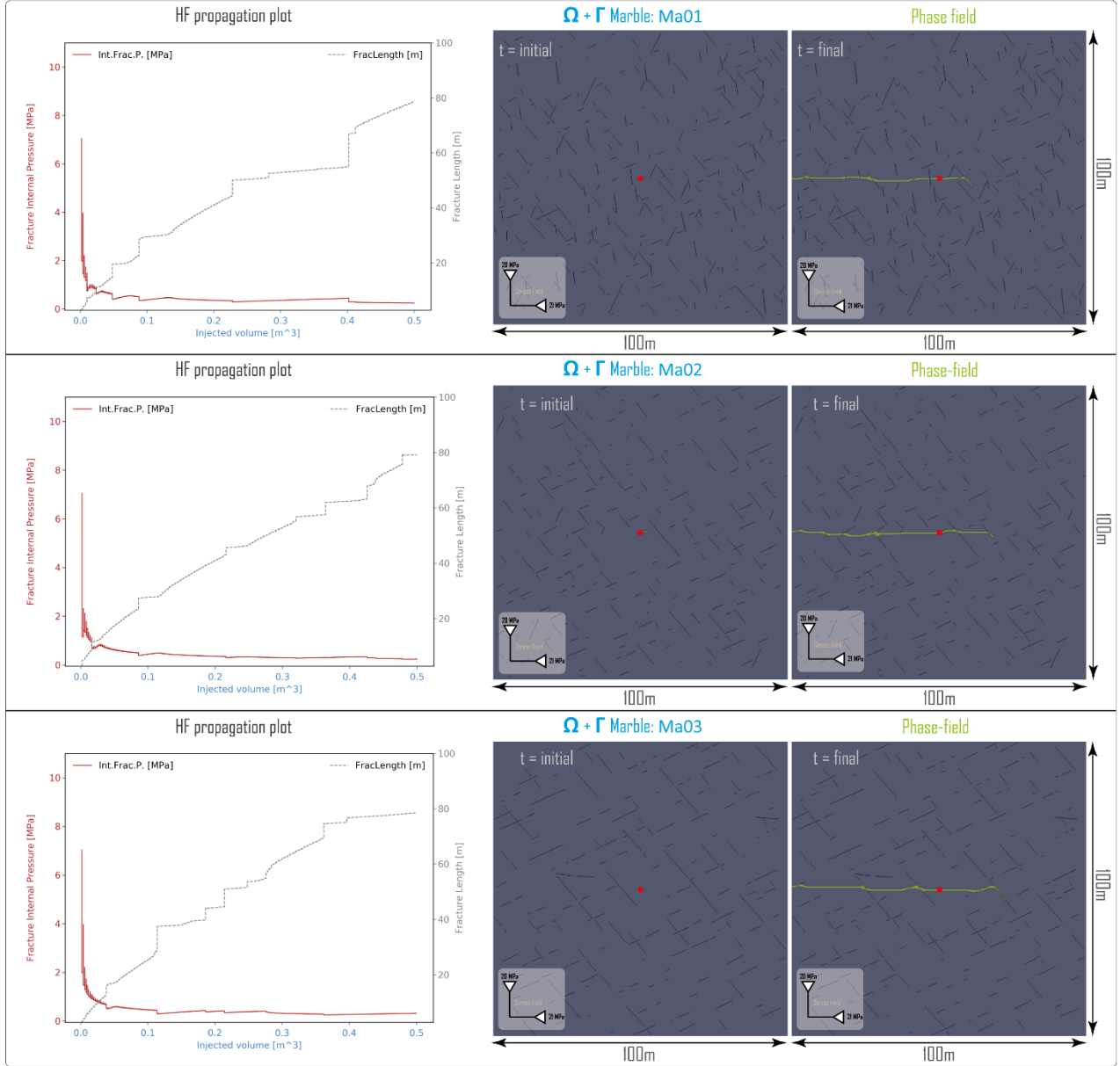
## 6.4 Results and discussion

Figure 25, Figure 26 and Figure 27 show the results of the simulated hydraulic fracturing scenarios for the three different lithologies. All cases have in common that the pressure in the hydraulic fracture decreases with volume and crack length. Whenever the hydraulic fracture interacts with a natural fracture, the pressure drops as a result of the increased storage from the sudden crack propagation within the natural fracture. Whenever the hydraulic fracture encounters a favourably oriented natural fracture, the hydraulic fracture requires almost no resistance and propagates rapidly over a finite length. From all three lithologies, the lowest pressure is seen in the marble cases and the highest one in the limestone.

The hydraulic fracture roughly follows the maximum horizontal stress direction even with the sealed pre-existing fractures present. However, these fractures lead to local deviations from this growth direction and preferential fracture growth in one direction rather than symmetric bi-wing fracture growth from the well.



**Figure 25: Hydraulic fracture models using the variational phase-field approach with sub-DFNs of the limestone reservoir. The matrix domain  $\Omega$  is shown in grey. The natural fracture domain  $\Gamma$  is shown in black. The red dot represents the wellbore.**



**Figure 26: Hydraulic fracture models using the variational phase-field approach with sub-DFNs of the marble reservoir. The matrix domain  $\Omega$  is shown in grey. The natural fracture domain  $\Gamma$  is shown in black. The red dot represents the wellbore.**

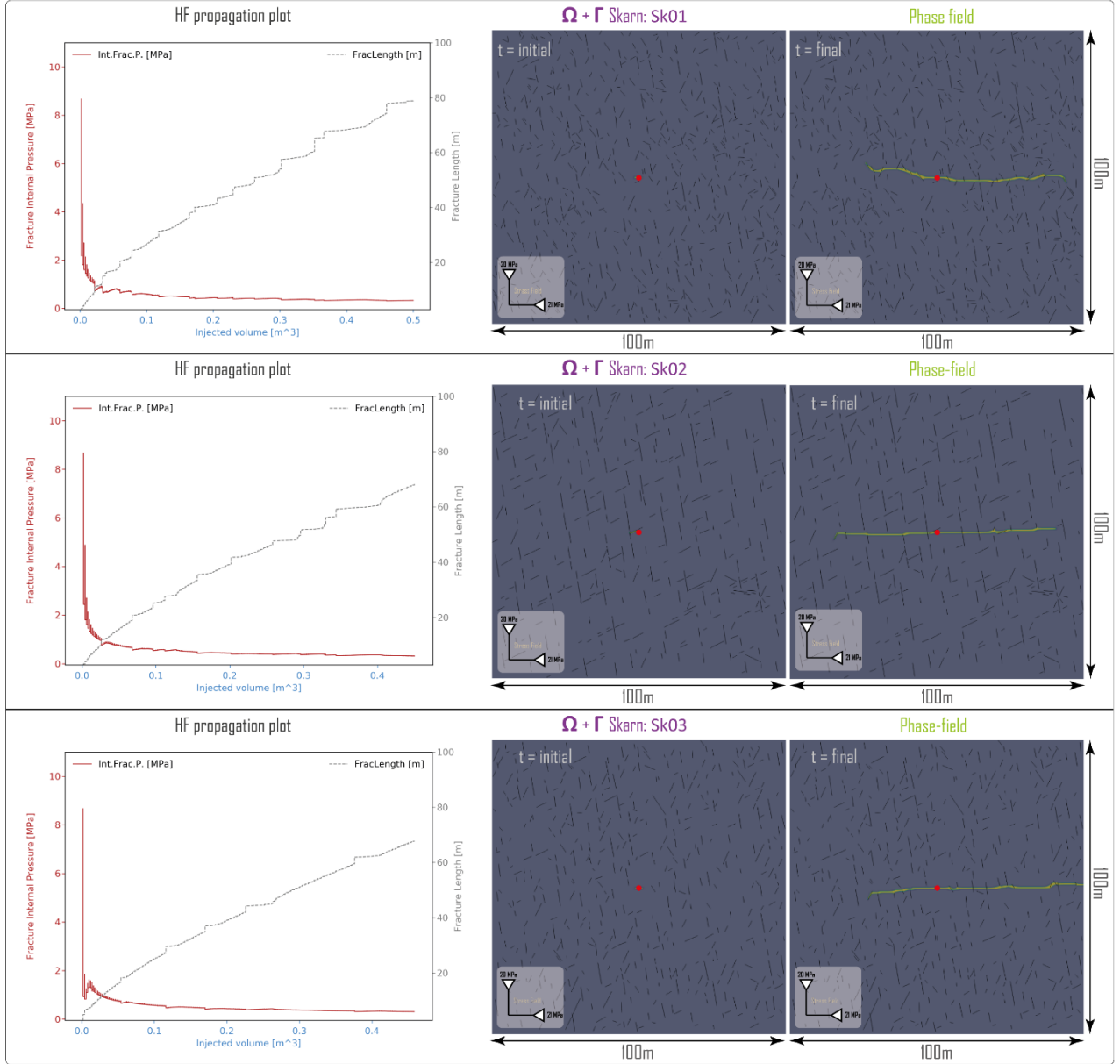


**Figure 27: Hydraulic fracture models using the variational phase-field approach with sub-DFNs of the skarn reservoir. The matrix domain  $\Omega$  is shown in grey. The natural fracture domain  $\Gamma$  is shown in black. The red dot represents the wellbore.**

## 6.5 Conclusions

We have presented a two-dimensional model for hydraulic fracture propagation in an impermeable rock matrix and interaction with a sealed natural fracture network. The model is based on a variational phase-field approach with high numerical stability. The results show that the hydraulic fracture growth direction is strongly depending on the direction of the minimum horizontal stress even for low differential stresses. Depending on their orientation natural fractures may lead to local deviations from this path. The simulations indicate that marble is the best stimulation target because of the lowest pressures. Marble has the lowest density of natural fractures, but fractures are longer and better connected. However, the optimal stimulation target depends on the ultimate goals of the EGS development and a detailed cost-balance analysis.



## 7 Induced seismicity and permeability enhancement during fluid injection

### 7.1 Introduction

The objective of this section is of twofold: (1) to evaluate the potential of reactivation of pre-existing faults by fluid injection during the stimulation stages, and (2) to predict the induced seismicity and the permeability enhancement inherent to the process of fault reactivation.

### 7.2 Methods and model setup

The new semi-analytical approach we developed is dedicated to honoring the physics of the problem where the key ingredients have been described in Candela et al. (2019). Our model considers fluid injection throughout a single fault in which the local pore pressure increase due to the transient pore pressure diffusion can potentially decrease the effective normal stress and push the fault to failure. The effect of cooling on the development of induced stresses and the reactivation of pre-existing faults is not currently included in our modelling approach. Once the fault slips, two processes are honored. First, the fault permeability can be locally enhanced following the dilatant model and then assuming a semi-steady-state solution for the diffusion equation (Fokker et al., 2020). Second, the shear and normal stresses are redistributed along the fault surface following the boundary element method. This way, multiple successive rupture events can be modelled. The workflow of our modelling approach is presented in Figure 28.

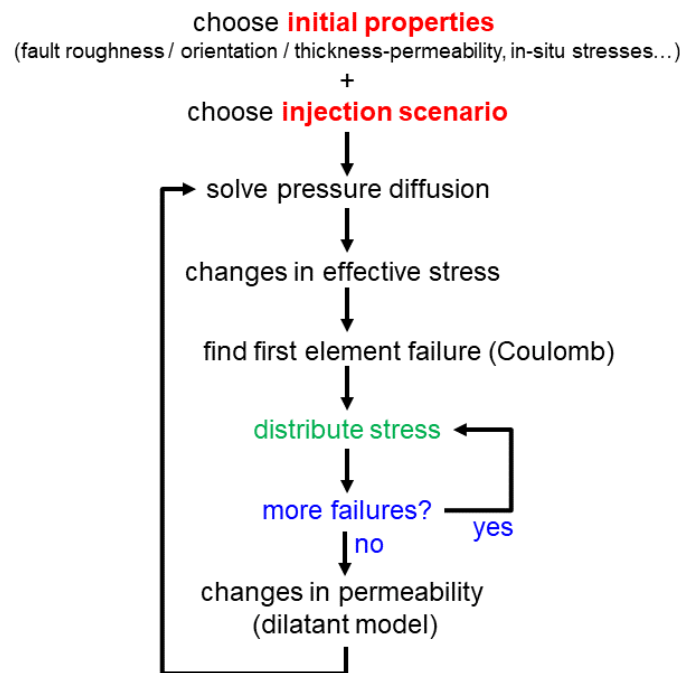


**Figure 28: Workflow to simulate induced seismicity and permeability enhancement during fluid injection throughout a fault.**

One of the key ingredients of our modelling approach is the inclusion of realistic heterogeneities solely at the level of the fault surface roughness. Indeed, instead of introducing unconstrained complexities in the fault friction, we choose to focus on the fault roughness and thus heterogeneities in the spatial distribution of the tectonic pre-stresses (before the start of injection). This modelling choice is justified by the fact that natural

observations indicate that the roughness of faults might be universal and can be well described by a synthetic fractal self-affine geometrical model (Candela et al., 2012; see Figure 29).

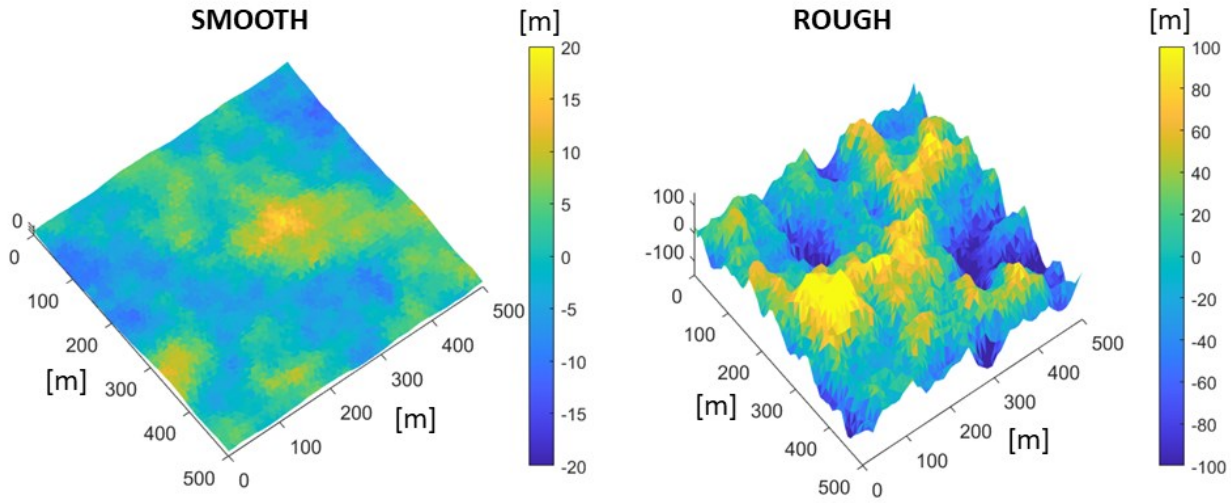


**Figure 29: Synthetic fault surface geometries used as inputs for our modelling strategy.**

Table 7.1 summarizes the scenarios we identified depending on: (1) type of fault roughness, (2) fault orientation, (3) in-situ stresses, (4) injection depth, (5) fracture permeability scheme, and (6) injection scheme.

Fault type	Fault orientation	In-situ stresses	Depth of injection	Fracture permeability scheme	Injection scheme
Smooth	Normal	Normal	800 m	Constant	Constant
Rough	Strike-slip	Strike-slip	1750 m	Updated	Cyclic

**Table 7.1: Range of scenarios covered in this fault reactivation study.**

#### *Type of fault roughness:*

The fault surface geometry has been built by following the approach described in Candela et al. (2009). Following the two end-members of the range of roughness observed for natural fault surfaces, we picked two types of fault geometry: the smooth type and rough type (see Figure 29).

#### *Fault orientation:*

Following the geological interpretations of the area of interest (see Figure 1, Section 2.1). Two fault orientations have been used, either the orientation of the strike-slip faults, striking N132°E with a dip of 67° towards SW, or the orientation of the normal faults striking N34°E with a dip of 74° towards NW.

#### *In-situ stresses:*

Two types of in-situ stresses have been used (cf. Section 2.2, Figure 3):

- (1) a strike-slip faulting regime with minimum horizontal stress gradient of 19.2 MPa/km, a vertical stress gradient of 24.3 MPa/km, and a maximum horizontal stress gradient of 34.4 MPa/km with an orientation of N56°E, and



- (2) a normal-slip faulting regime with minimum horizontal stress gradient of 19.2 MPa/km, a vertical stress gradient of 29 MPa/km, and a maximum horizontal stress gradient of 27 MPa/km with an orientation of N56°E.

For both faulting regimes the pore pressure gradient was 8.73 MPa/km.

#### *Injection depth:*

Two injection depths have been picked: (1) 800m that is below the open hole, and (2) 1750m that is at the granite/marble interface in line with the stimulation targets in Section 8.4.

#### *Fracture permeability scheme:*

Two types of permeability scheme have been used: either (1) the permeability was kept constant or (2) the permeability was enhanced following the dilatant model. In the dilatant model, the fracture opening is directly proportional to the local amount of slip and thus also directly proportional to the local fault roughness.

#### *Injection scheme:*

Two injection schemes have been used, either a constant injection rate or a cyclic injection (see Figure 30). These two injection schemes are aligned with the MFRAC injection scenarios for well EAC-1 (see Section 3):

- (1) Constant injection rate of 100 kg/s maintained for 166.6 minutes, and thus a total volume injected of 1000 m<sup>3</sup>,
- (2) Cyclic injection rate (constant injection of 20min at a rate of 100 kg/s, alternating with shut-in period of 60 min) with a total volume injected of 1000 m<sup>3</sup>.

For both injection schemes, after injection, a shut-in period of up to 2 days was applied.

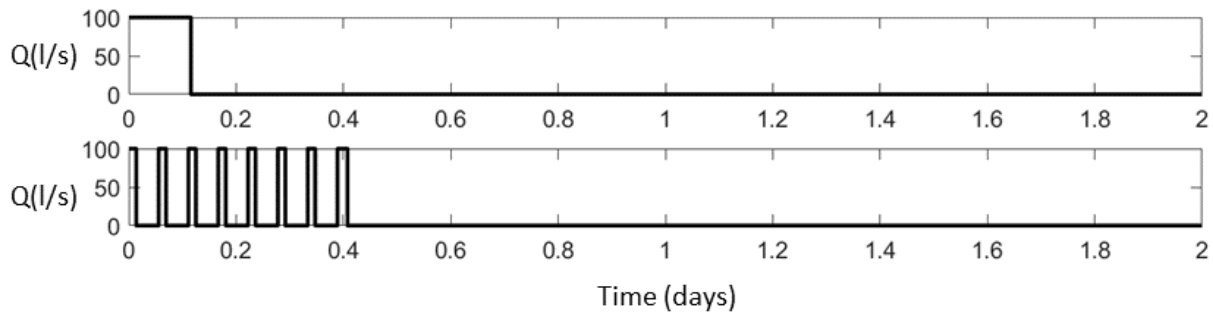


**Figure 30: Constant (top) and cyclic (bottom) injection schemes used for the fault reactivation study.**

Consequently, in total 64 (2<sup>6</sup>) possible scenarios were identified. In addition, the initial fault width and thus its permeability (linked together following the cubic law) have been constrained by both (1) the magnitude of the minimum horizontal stresses at both injection depths and (2) the injection scheme. The idea here is that in our injection model, the bottom hole pressure should not be higher than the minimum horizontal stress to avoid hydraulic fracturing of the rock matrix instead of reactivating a pre-existing fault. To this end, for each injection depth multiple runs with different initial permeability have been conducted, each of them making sure the bottom hole pressure was below the minimum horizontal stress.

### 7.3 Results

Here, only the results obtained with the strike-slip fault orientation and strike-slip faulting regime are presented. Thus, the number of scenarios reduces to 16 ( $2^4$ ). These results are representative for the other couple of fault orientation / faulting regime.

Figure 4 presents the spatial distribution of the initial (before injection) distance to criticality which is defined as fault strength minus shear stress for the injection depth of 800 m. In other words, this metric informs us on how far/close the fault surface is from failure before fluid injection.

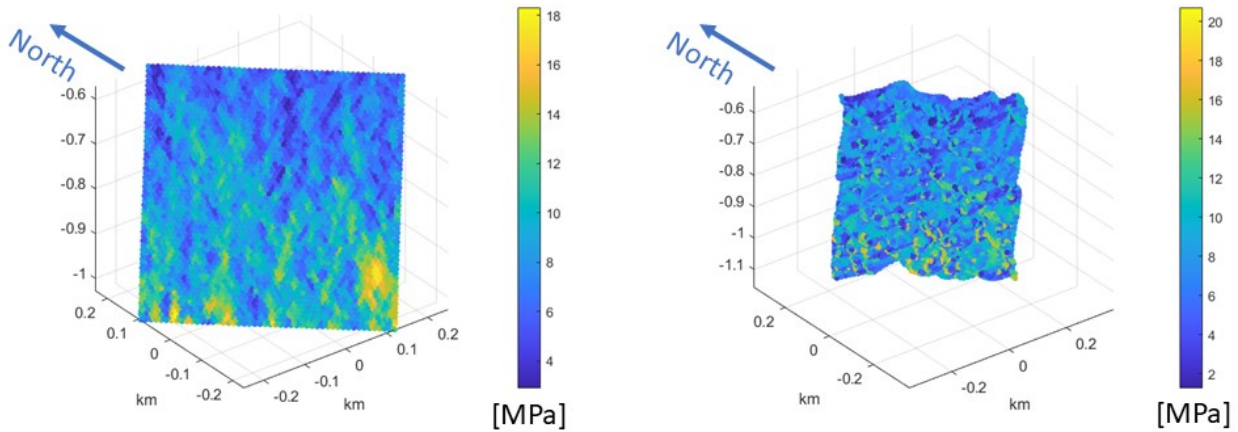


**Figure 31: Pre-injection distance to criticality at 800 m injection depth for the smooth (left) and rough (right) fault scenario.**

Figure 32 to Figure 35 display the results for the 16 scenarios of the strike-slip fault orientation and strike-slip faulting regime. As stated previously, for each scenario multiple runs varying the initial fracture permeability/thickness have been conducted. For each of these figures:

- the first column displays the magnitude of the induced rupture events in the spatio-temporal domain for all the scenarios,
- the second column shows the spatio-temporal distribution of the induced rupture events. Each color indicates an individual run with different initial fracture permeability, and
- the third column displays the spatial distribution of the fault permeability. Each color indicates an individual run with different initial fracture permeability.

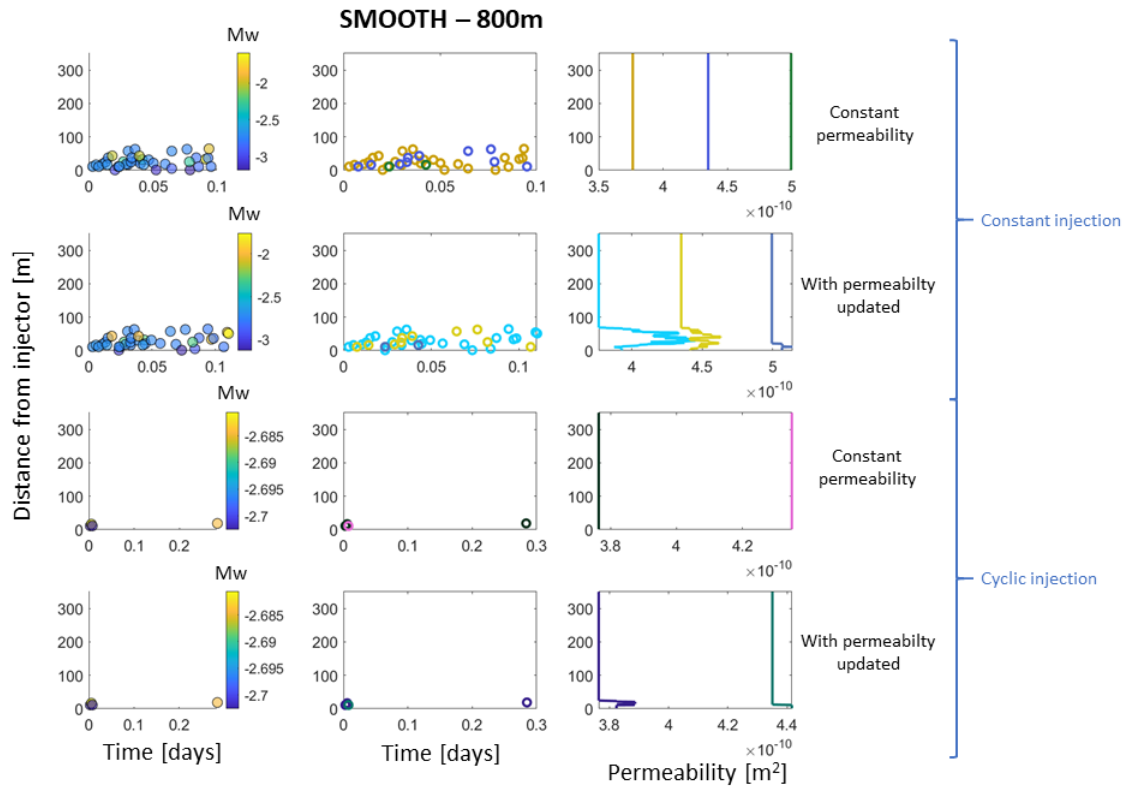


Figure 32: Simulation results for the smooth fault and injection depth of 800 m.

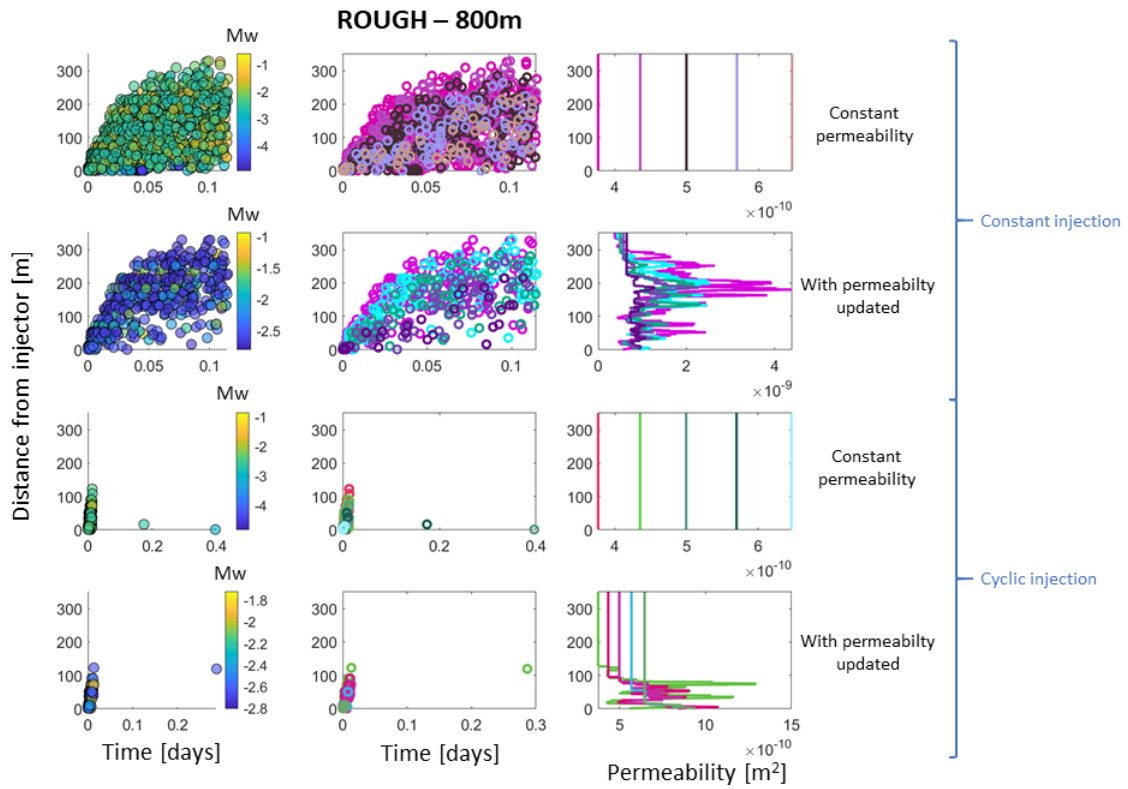


Figure 33: Simulation results for the rough fault and injection depth of 800 m.

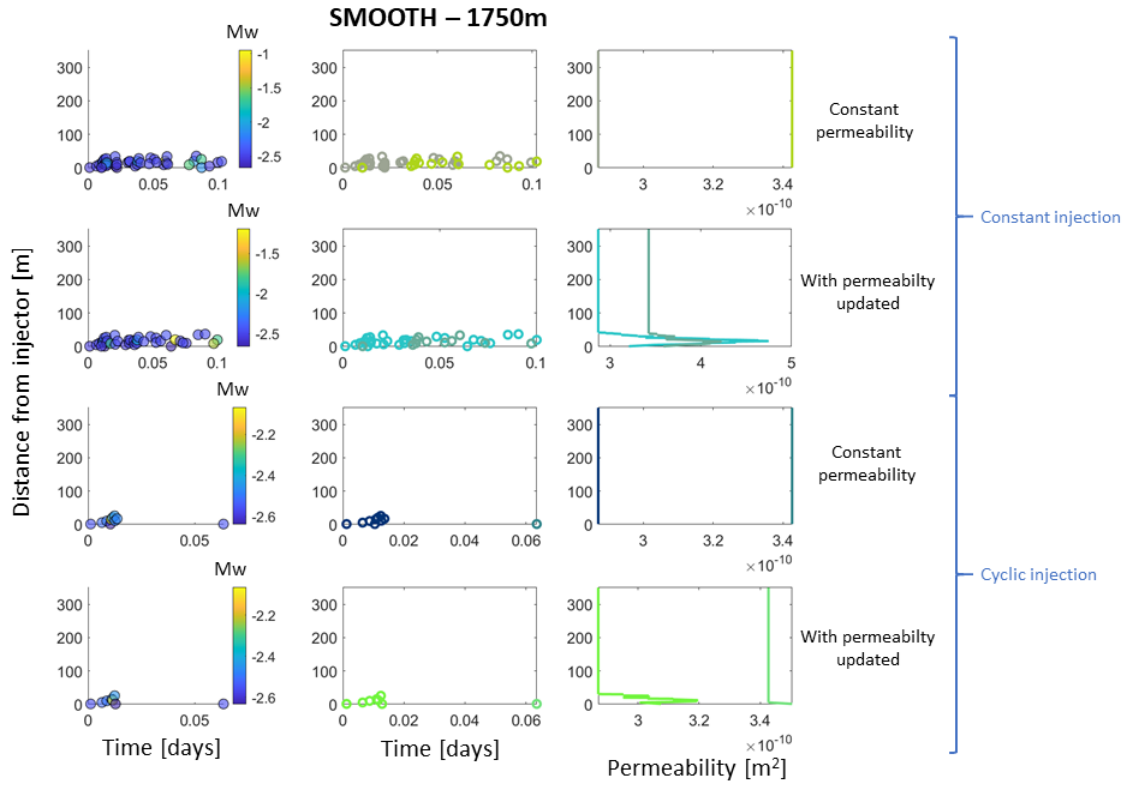


Figure 34: Simulation results for the smooth fault and injection depth of 1750 m.

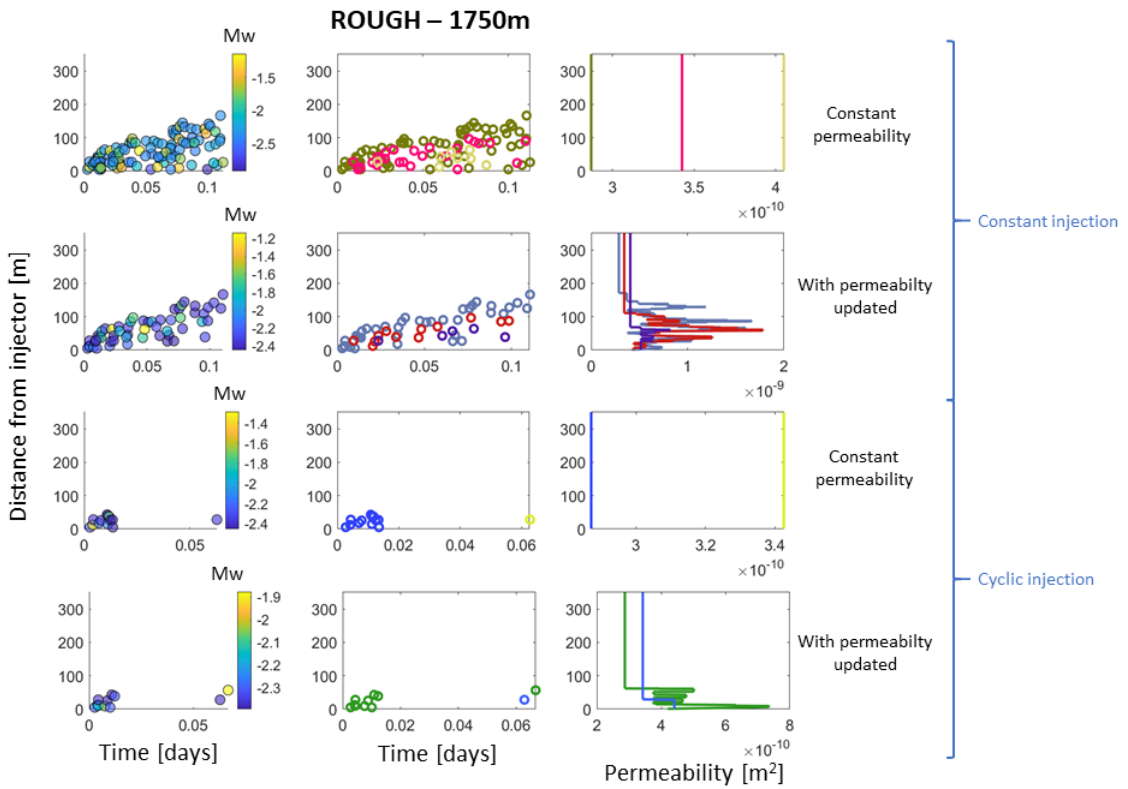


Figure 35: Simulation results for the rough fault and injection depth of 1750 m.

## 7.4 Discussion and conclusions

### *Effect of the permeability enhancement on the rate of induced seismicity:*

As expected, the rate of induced rupture events is slightly reduced when the fault permeability is enhanced following the dilatant model. This can be explained by the slowdown of the pressure increase when the permeability is locally enhanced.

### *Effect of the cyclicity on the rate of induced seismicity:*

The rate of induced rupture events is significantly reduced when applying the cyclic injection scheme. This can be explained by the lowering of the maximum increase in bottom hole pressure when injecting cyclically and applying shut-in periods during which the local increase in pore pressure diffuses away (see Figure 36).

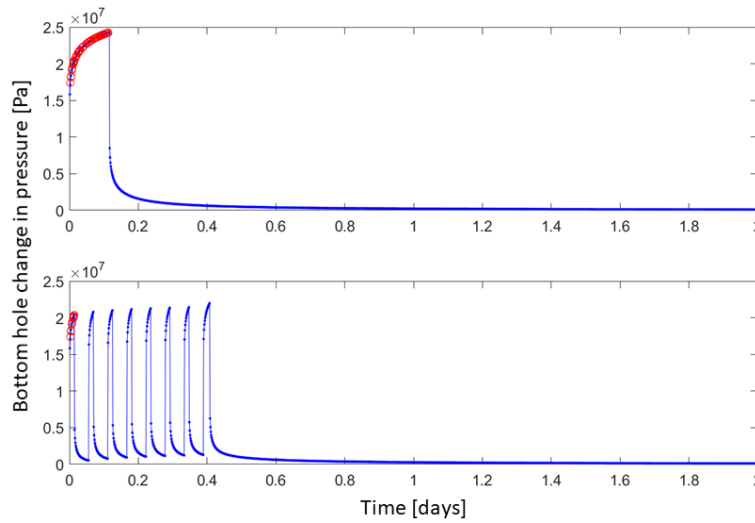


Figure 36: Changes in the bottom hole pressure during constant (top) and cyclic (bottom) injection for the scenarios with an injection depth of 1750 m, and a constant permeability. Red circles represent the times of induced rupture events.

### *Effect of the fault roughness on the rate of induced seismicity:*

The rate of induced rupture events is significantly increased when the fault surface is rougher. This can be partially explained by the larger fluctuations of the pre-injection distance to criticality for the rougher faults (see Figure 31).

Overall, for all the scenarios, the maximum magnitude of the induced rupture events remains small, smaller than minus one. Consequently, our modelling approach predicts that the risk associated with induced seismicity remains limited. In other words, one can consider all simulated scenarios of injection as relatively safe from an induced seismicity perspective. Note, that this analysis does not replace a seismic risk assessment. The scenario stimulating a rough fault with an injection depth of 800 m and with a constant injection rate can be seen as the most optimum. Indeed, for this scenario the fault permeability can be enhanced up to one order of magnitude.

## 8 EGS development options for EAC-1 and EAC-2

### 8.1 Stimulation type

#### 8.1.1 Thermal stimulation

Injection of cold water into a hot rock mass leads to a thermal contraction of the rock, which then creates thermal cracks that can act as fluid pathways. This effect is enhanced by larger temperature differences and the presence of different minerals with variable thermal expansion coefficients. Thermal stimulation occurs at all pressures and can thus also be performed at low overpressures. Injection of cold water can be done continuously or cyclically. These phenomena were observed by Grant et al. (2013), who provide a review of thermal stimulation of geothermal wells. They propose that the injectivity of a geothermal well might increase with time  $t$  at a rate of  $t^n$  with  $n$  between 0.4 and 0.7 by up to two orders of magnitude and that the transmissivity increases proportional to  $\Delta T^3$ . However, they also found that thermal stimulation effects can be reversible if insufficient propping is achieved by fracture surface asperities.

Thermal fracturing has been performed primarily in high temperature fields worldwide. One example in Mexico are thermal fracturing treatments of wells H-40, H-41, H-43, H-44 and H-45 in the Los Hornos geothermal field (Flores-Armenta and Tovar-Aguado 2008; Luviano et al. 2015). Thermal stimulation was performed with  $\sim 20^\circ\text{C}$  water injected in a cyclic manner ( $\sim 1$ -3 hours injection followed by  $\sim 10$  hours shut-in) with stepwise increasing flow rates between  $\sim 17$  l/s and 48 l/s and injection pressures of up to 15 MPa. With this method, it was possible to successfully stimulate deeper target zones without zonal isolation in Los Hornos. While the hydraulic performance of these wells could be improved formation damage (indicated by positive skin) remained.

The experience in Los Hornos shows that thermal stimulation of deep feed zones in Acoculco may also be successful without zonal isolation. In EAC-1 and EAC-2 this method is more suitable for the deeper and hotter granites compared to the shallower formations with lower temperature. In impermeable rock the thermal stimulation effect is limited to the near wellbore area. If existing flow paths are present or new flowpaths are created this area of influence can be somewhat extended, as shown in Chapter 4. Long-term, possibly cyclic, injection and large volumes of cold water would be required to achieve significant thermal stimulation effects.

#### 8.1.2 Hydraulic shear stimulation

Hydraulic shear stimulation treatments aim to improve the permeability of existing fractures by shear displacement caused by shear stresses on these fractures, which are opened up by pressure increase and stress changes. Since displaced rough fracture surfaces do not match each other anymore a permanent aperture increase may be achieved. This allows fractures to stay open without the use of proppants or chemicals. Shear stimulation is more effective in rocks with a high compressive strength, such as granites, since the asperities keeping the fracture open are stronger (Hofmann et al. 2016b; Milsch et al. 2016). However, weak, and preferably partially open fractures are required to make this method feasible. Dedicated hydraulic shear stimulation treatments are performed below the hydraulic fracturing pressure of the target formation.

In EAC-1 and EAC-2, shear stimulation would be most efficient in the strong granites, highly fractured marbles and identified inflow zones, as highlighted in Chapters 6 and 7. Without zonal isolation, it will not be possible to stimulate a dedicated target zone, but the fractures most susceptible to slip along the open hole section will be stimulated. Simulations presented in Chapter 7 indicate that the hydraulic performance of the wells may be enhanced by one order of magnitude by hydraulic shear stimulation.

### **8.1.3 Hydraulic fracturing**

Hydraulic fracturing improves the well performance by creating new fractures as fluid pathways by high pressure injection above the fracturing pressure (Economides and Nolte 2000). Since these fractures open in tensile mode without shear displacement, proppants or acids are required in order to keep a permanent flow path open after the treatment. However, both mode I (tensile) and mode II (shear) failure may occur during high pressure fluid injections into a fractured rock mass (McClure and Horne 2014). This may lead to permanently open fractures resulting from pure water fracturing treatments without proppants or acids.

Gel-proppant fracturing has limited applicability for EAC-1 and EAC-2 since the length of propped hydraulic fractures is typically less than 100 m (Zimmermann et al. 2011) and more complicated stimulation fluids and treatment schedules would be needed. Dedicated water fracturing treatments above the hydraulic fracturing pressure would also not be advised for the planned injection test in Acoculco since zonal isolation would be required to stimulate zones significantly below the casing shoe (see Chapters 3, 4 and 5), higher pressure equipment would be required as compared to shear stimulation, and the required pressure to hydraulically fracture the rock is currently largely unknown as a result of the limited information on the stress field (Figure 3).

Nevertheless, investigating hydraulic fracturing scenarios for Acoculco is still useful. It can be seen as one end-member of processes that may occur during fluid injection. As stated above, the separation between hydraulic fracturing and shear-stimulation is rather conceptual, since both mode I (hydraulic fracturing) and mode II (hydroshearing) opening may result from fluid injection with uncertain boundary conditions and it can not always be identified which process is the dominant one.

### **8.1.4 Chemical stimulation**

Chemical stimulation treatments aim to dissolve specific minerals to develop new flow pathways and improve existing ones. A history of acid fracturing and common procedures is provided by Kalfayan (2007). Targets could be fracture fillings such as Calcite, which can be dissolved by HCl, or Quartz, which can be dissolved by HF. Near wellbore damage may also be resolved by dissolving the mud cake which plugs flow paths after drilling.

In Acoculco the application of HCl to dissolve Calcite in fractures and marbles would be the primary target. For such a treatment special safety measures would be required to protect casing and cement. Given the state of the wells EAC-1 and EAC-2 it is not advisable to apply this technique before thermal and hydraulic stimulation treatments have been tested. Nevertheless, the simplified models presented in Chapter 4, that do not consider the multiple stages typically performed in chemical stimulation treatments, show the added fracture conductivity that may result from a targeted application of chemical stimulation in the carbonate formations in Acoculco.

## **8.2 Zonal isolation**

Different zonal isolation options for wells EAC-1 and EAC-2 are summarized in Figure 37.

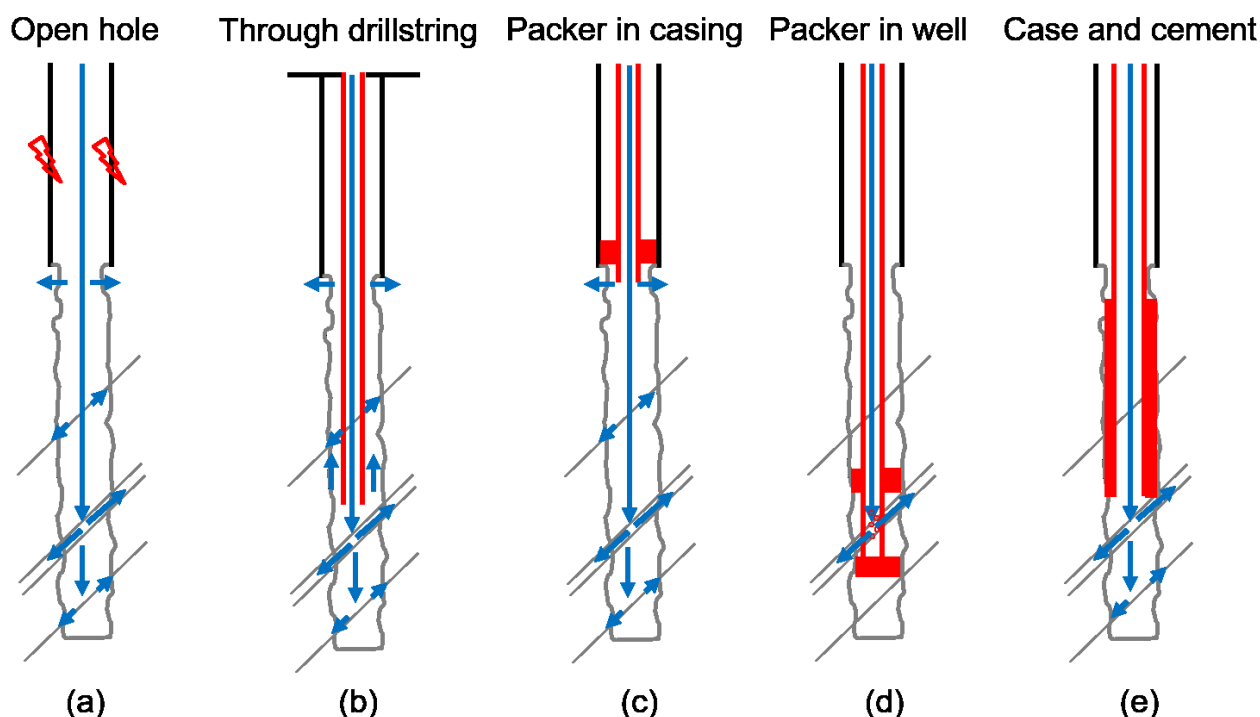


Figure 37: Summary of zonal isolation options. A) no zonal isolation with injection through the wellhead, B) no zonal isolation with injection through an injection string, C) isolation between casing and open hole by inflatable packer in casing, D) straddle packer system to isolate the desired target section, E) case and cement the well down to the target interval.

### 8.2.1 Open hole stimulation

Open hole stimulation with injection through the wellhead is the easiest and most inexpensive stimulation operation since no rig is required. However, one must make sure that the casing is intact and will not fail due to applied pressures, thermal stresses or acids. This is especially true for old wells, such as EAC-1 and EAC-2. Wellbore integrity is addressed in Section 8.3. Additionally, no isolation of specific target zones is possible with this procedure. When high pressures are applied, the stimulated area will likely be below the casing shoe, where in-situ stresses are lowest, and potentially some deeper parts of the well that already accept fluids. Thermal stimulation combined with hydraulic shear stimulation of pre-existing feed zones would be the most promising stimulation processes for open hole stimulations.

### 8.2.2 Injection string

With injection string and no packers, chemical stimulation would be possible when the acid is injected through the injection string to the depth of the stimulation target and at the same time the annulus is pressurized to prevent the acid from flowing up the annulus again and forcing it into the target zone. Additionally, thermal stimulation can be performed more target-oriented as the lowest fluid temperature in contact with the formation would be at the bottom of the injection string and the casing would be better protected from thermal stresses. For the thermal stimulation scenario, the annulus should be closed. For hydraulic fracturing and hydraulic shear stimulation the injection string would only increase the frictional pressure losses as compared to the open hole stimulation (Figure 38). It would not have any benefits.



### 8.2.3 Casing packer

If the casing integrity with respect to the applied thermal stresses, pressures or acids is in question, injection through an injection string and a packer set right above the casing shoe can protect the casing from pressures and acids and also reduces the thermal strain.

### 8.2.4 Open hole packer

Zonal isolation by setting inflatable or swellable packers inside the open hole section has a low chance of success because of out of gauge hole conditions, pre-existing fractures, development of vertical fractures in a vertical well, high reservoir temperatures and missing borehole televiewer images. Multi-set packers would be needed, the well would need to be continuously cooled and at least caliper log information would need to be available in order to increase the chances of success.

### 8.2.5 Case and cement

The safest, but most expensive way to isolate the deep and hot part of the wells from the shallow zones with lower temperatures is to install a casing to the desired target depth. This allows to stimulate the bottom of the well efficiently. Later on, the casing could be perforated to additionally stimulate shallower intervals with the help of casing packers.

Besides the high cost and operational risks of such a procedure, it also significantly reduces the well diameter, which will cause high frictional pressure losses. The 5 7/8" to 6" open hole diameter allows to install a casing with maximum OD of 4 1/2" and maximum ID of ~4". These pressure losses  $\Delta P$  resulting from injecting a fluid with viscosity  $\mu$  at a flow rate  $Q$  along a pipe with a length  $L$  and a diameter  $D$  can be estimated by the following equation:  $\Delta P = L \rho^{0.8} Q^{1.8} \mu^{0.2} / 901.63 D^{4.8}$  (Gabolde and Nguyen 2006). With a density  $\rho$  of 1000 kg/m<sup>3</sup>, a viscosity of 1 mPas, and a diameter of 4" and this would lead to frictional pressure losses of up to 16 MPa at 100 l/s flow rate of water (Figure 38). Whether or not this option is feasible depends on the budget and anticipated target flow rate.

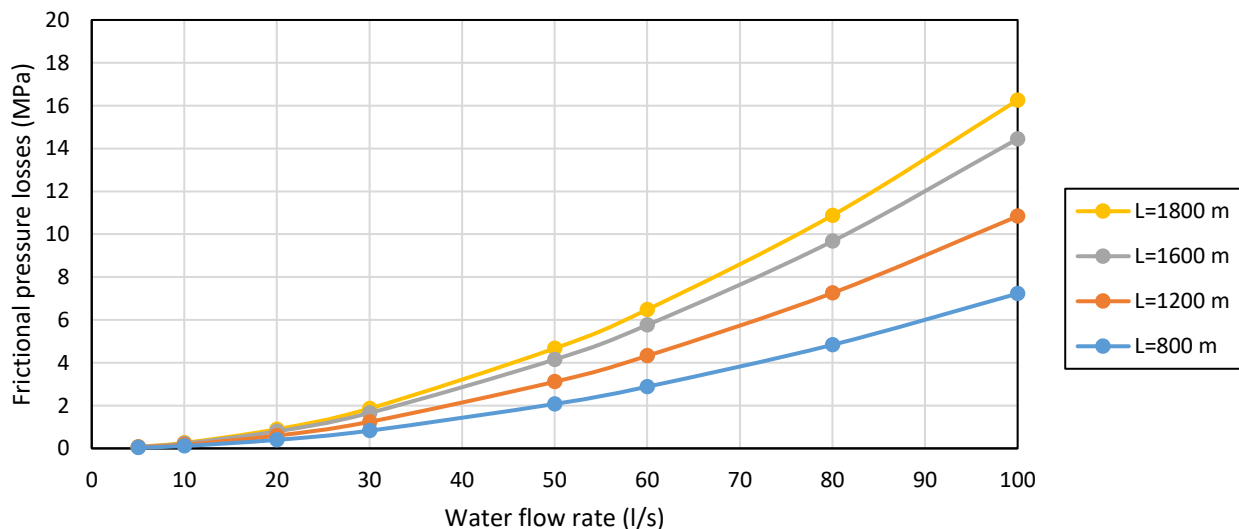


Figure 38: Frictional pressure losses resulting from cold water injection or production through a 4" ID casing of variable length L.

### 8.3 Wellbore integrity

A significant amount of thermo-mechanical stresses resulting from the aforementioned stimulation scenarios (i.e., hydraulic, shear, and thermal) will threaten the integrity of the coupled casing-cement-rock system potentially leading to casing failures, cement cracking or debonding at cement interfaces (Kruszewski et al., 2018) and, as a result, formation of fluid pathways. This is especially dangerous in the case when multiple aquifers with different temperature and chemical composition are penetrated. To mitigate risks resulting from the stimulation operations in Acoculco, stresses at interfaces of the coupled casing-cement-rock system, most desirably with integration of sonic and ultrasonic cement bond logs, shall be evaluated and the intervals most susceptible to failure should be localised. Such scenarios were investigated within the GEMex project in Kruszewski et al. (2019).

For the case of acid stimulation it is of utmost importance to secure good seal between cement and stimulation interval as well as assure that no direct contact between acidic stimulation fluid and cement material is present. In the most undesirable case, a direct contact between a cement material and acidic injection fluids may occur. This can lead to a dissolution of cement material and, as a result, will cause rupture of the cement sheath. In the situation of acid stimulation, it is of utmost importance to apply cement blends insensitive to the acid environment and, in addition, resistant to thermal and pressure cyclic loads. One of the possible options are sealants not based on conventionally used Portland cement types, based primarily on gypsum and clinker. These non-Portland sealants may include alkali-activated aluminosilicates (i.e., so-called geopolymers), which exhibit stable and high compressive and flexural strength, good resistance towards thermal cyclic loading, improved ductility with low elastic moduli, acid insensitivity, and improved water permeability, while its self-induced shrinkage remains marginal (Kruszewski, Glissner, Hahn, Wittig, submitted).

### 8.4 Stimulation targets and scenarios

Based on the previous considerations, potential stimulation targets are listed below. The order is important. If the first target will not achieve the desired well performance, the following target should be pursued:

- 1) Overcome near wellbore damage to access a permeable rock mass
- 2) Improve permeability of existing fracture networks
- 3) Connect permeable fault damage zone or fault intersection to the well
- 4) Hydraulically connect wells EAC-1 and EAC-2 through the stimulated fracture networks
- 5) Drill a third well or side-track an existing one into the stimulated reservoir volume
- 6) Use the knowledge gained through exploration and injection tests to develop a dedicated EGS by drilling new wells in Acoculco

Potential target sections are marked green in Figure 39. These were primarily identified based on the following fracture and fluid flow indicators: temperature anomalies, fluid loss during drilling and fractures identified on cores or cuttings. Given the close proximity of EAC-1 to local faults and fault intersection, it is more likely that these can be stimulated by injection into EAC-1 (Figure 1). Additionally, there were almost no fluid losses in EAC-2 while at least very minimum fluid losses occurred in the deeper sections of EAC-1, which makes it a better stimulation candidate to start with.

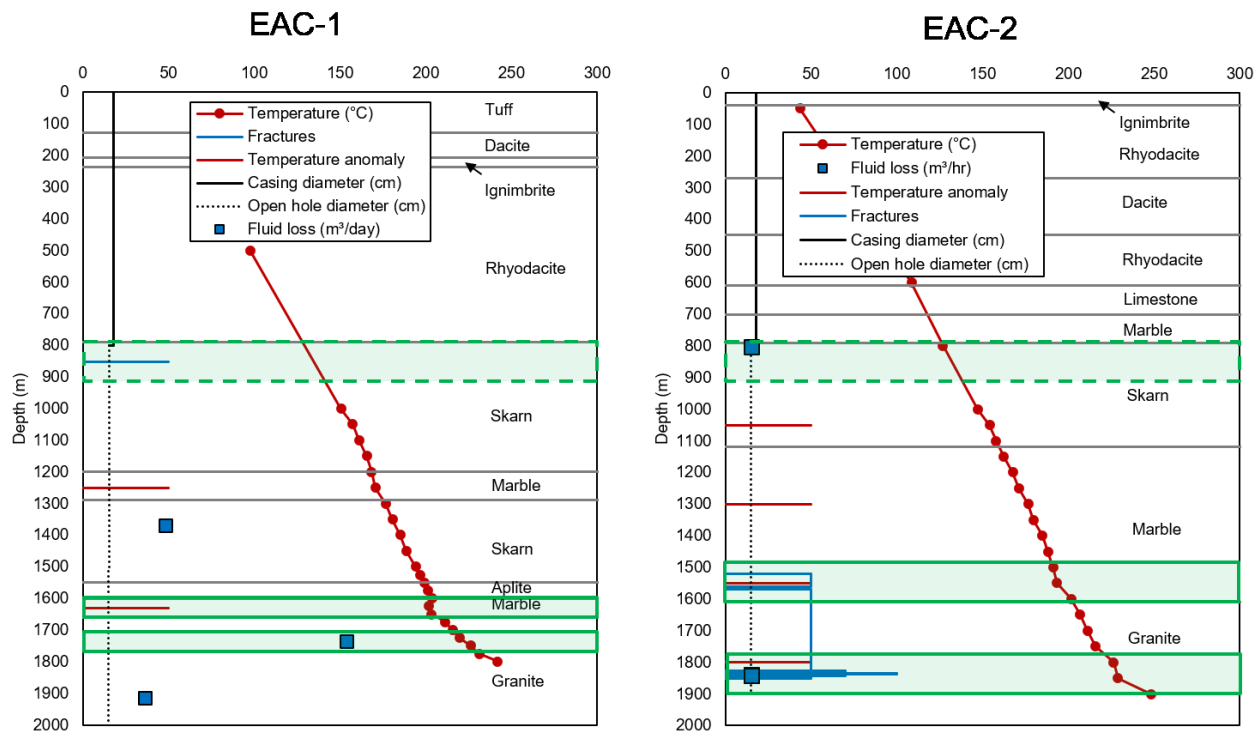


Figure 39: Wellbore schematic, lithology, identified fractures, temperature logs 6 hours after drilling, fluid losses during drilling and potential stimulation target zones (green) in wells EAC-1 (left) and EAC-2 (right).

#### 8.4.1 Scenario 1: Stimulation of skarns below 800 m

Open hole stimulation with or without casing packer would likely stimulate the well directly below the casing at 800 m depth. The temperature of the produced water from this zone would be ~150°C.

Potential activated structures are fractures filled with calcite and pyrite identified by Gama et al. (1995) at 850 – 853 m in EAC-1 and a zone that encountered a steam influx at 799 m in EAC-2 (Figure 39). No temperature data is available between 800 m and 1000 m in both wells so that no temperature anomalies could be identified. The high variability of porosity, resistivity, elastic properties and strength of skarn may prevent stimulation out of zone (Chapter 4). This is important as fracture growth into the overlying volcanics and limestones would significantly reduce hydraulic stimulation efficiency, as a large amount of injected fluid may leak-off into these volcanic rocks, which have a higher porosity and permeability compared to the skarns.

Hydraulic shear stimulation and chemical stimulation with HCl are the most suitable methods for this section. Hydraulic fracturing is required if the natural fractures cannot be opened. After an initial injection test to determine the initial hydraulic performance, a step rate test should be performed to identify the fracture opening pressure (FOP). Once this is established, the stimulation should be performed only slightly above this FOP in order to reduce the chance of out-of-zone fracture growth. If this does not lead to the desired performance increase short cycles of high flow rate injection should be performed. If the hydraulic performance increase is reversible HCl should be added to the injection fluid to dissolve the calcite filling the fractures and etch the fracture surfaces, which would keep the fractures open. Alternatively, proppants would need to be injected.

#### **8.4.2 Scenario 2: Stimulation of marbles at 1200 – 1300 m or 1600 – 1650 m in EAC-1 and 1500 – 1600 m in EAC-2**

Temperature anomalies in each of the marble sections indicate some flow in these formations. Without zonal isolation and injection through the well head these zones may only be stimulated thermally and hydraulically at low flow rates and pressures over the course of weeks and months. The initial flow rates should be similar to the leak-off rates observed in the wells (0.3 – 1.7 l/s) to identify the initial hydraulic performance and can be increased in steps. This would slowly decrease the fluid temperature, which would protect the casing, and it would reduce the risk to stimulate the shallower parts of the well. If the permeability of these inflow zones is gradually increased by thermal and hydraulic effects due to injection, the flow rate can be increased until the desired target rates, while the pressures have to be kept below the pressure required to hydraulically fracture the shallower intact parts of the well. For economic reasons, such an operation may be performed without drill rig on site.

#### **8.4.3 Scenario 3: Stimulation of granites below 1700 m in EAC-1 and below 1600 m in EAC-2**

Overall, zonal isolation and high pressures would be required to hydraulically fracture the granitic rock due to its higher strength and high stresses. Since all formations above the granites should have similar or lower permeability, strength and stresses, even with zonal isolation height growth out of the granite body may be excessive (see Chapter 3 and 4). Thermal or hydraulic stimulation may be successful in this case by targeting existing fractures and inflow zones. Chemical stimulation with HF to dissolve quartz minerals may be an option if thermal and hydraulic stimulation remains unsuccessful. Since a drill rig would be required, the costs for this scenario are comparatively high.

### **9 EGS development workflow for EAC-1 and EAC-2**

Based on the evaluation of the stimulation options discussed above, we consider it most valuable to use the planned stimulation tests in the exploration wells EAC-1 and EAC-2 to constrain structural geological features and stresses and to learn from these injection tests for future EGS projects in Acoculco, where wells are specifically designed for stimulation. Figure 40 shows the proposed stimulation workflow for well EAC-1 which primarily targets the deep inflow zones in marbles and granites, with skarns below the casing shoe as secondary targets.

Monitoring should include a seismic surface network that allows to locate seismic events down to magnitude -1 automatically in real-time with reasonable location accuracy. Additionally, a borehole geophone chain or fibre optic cable should be installed in the other well in order to improve the vertical location accuracy. The microseismic monitoring concept for the planned stimulation test in Acoculco is summarized by Hernández et al. (2020) and GEMex Deliverable 7.3 (Peters et al. 2020a). To support this, an initial investigation of the behaviour of the seismic wavefield with and without partial melting was performed by Farina et al. (2020). The injection well should be equipped with a fibre optic temperature cable in order to monitor in real-time the development of the feed zones. Alternatively, frequent temperature logs are required during the operations. Where applicable, flow rates, pressures and temperatures should be monitored at the wellhead, at target depth, on the return line and in the other well. Moreover, monitoring should include seismic-while drilling by the drill-bit source during drilling of new wells in super-hot and potential EGS. This method is more extensively described in GEMex Deliverable D8.4 (Mendrinós et al. 2020) together with distributed acoustic sensing (DAS) in high-temperature geothermal systems.

First, a dummy and/or temperature log should be run to determine whether the well is accessible and to determine the initial wellbore condition. This should be followed by reaming operations in order to clean the well from any potential obstructions. Afterwards, the casing integrity should be tested hydraulically and by logging. If casing or cement are not intact and this cannot be fixed operations should continue with well EAC-2. If the casing may not withstand the expected temperature, pressure and chemical changes an injection string with casing packer needs to be installed to protect the casing. First, an injection test with constant injection below 1.7 l/s should be conducted until a relatively constant pressure level is reached (at least 1 hour) followed by a shut-in period of at least two times the injection period ( $>2$  hours). 1.7 l/s was the highest fluid loss rate during drilling of EAC-1 in 1736 m depth, which is the primary target of this operation. A higher rate may be used if no considerable pressure increase is observed. This test will allow to determine the initial injectivity index of the well and the calculation of hydraulic well and reservoir parameters, such as compressibility, skin, transmissivity and productivity index. After this test a temperature log will confirm the depth where the injected fluid was injected into. This may also be confirmed by induced seismic events if present. At this stage, no induced seismicity is expected to occur though due to the low pressures. If injection occurred at 1736 m depth, or a similar deep inflow zone, injection should continue for a longer duration with at least the same and up to twice the flow rate used in the injection test. If an injectivity increase with time is observed continue injection until injectivity remains constant. Then, increase the flow rate to a higher level and continue injection again until no further injectivity increase is observed. Each of the flow rate steps should last until the injectivity stays constant. This process is repeated until the pressure or flow rate cannot be further increased or the target injectivity is reached as long as induced seismicity is under control. Temperature measurements and locations of induced seismic events should confirm whether injection still continues into the deep target zone after significant flow rate and/or pressure increase. If the pressure limit of the equipment is not yet reached, but the capacity of the surface water supply restricts further flow rate increase, injection should be temporarily halted or reduced while water tanks on site are filled to inject the stored water at a higher flow rate (i.e. cyclic injection). This would also allow the rock mass to heat up again, which may improve the thermal stimulation efficiency of the next cycles. If injection into shallower zones (e.g. below the casing shoe) is observed, this may be defined as new target zone. To stimulate the shallow zone a step rate test should be performed to determine the fracture opening pressure FOP followed by injection above the FOP and similar stepwise flow rate increase as before.

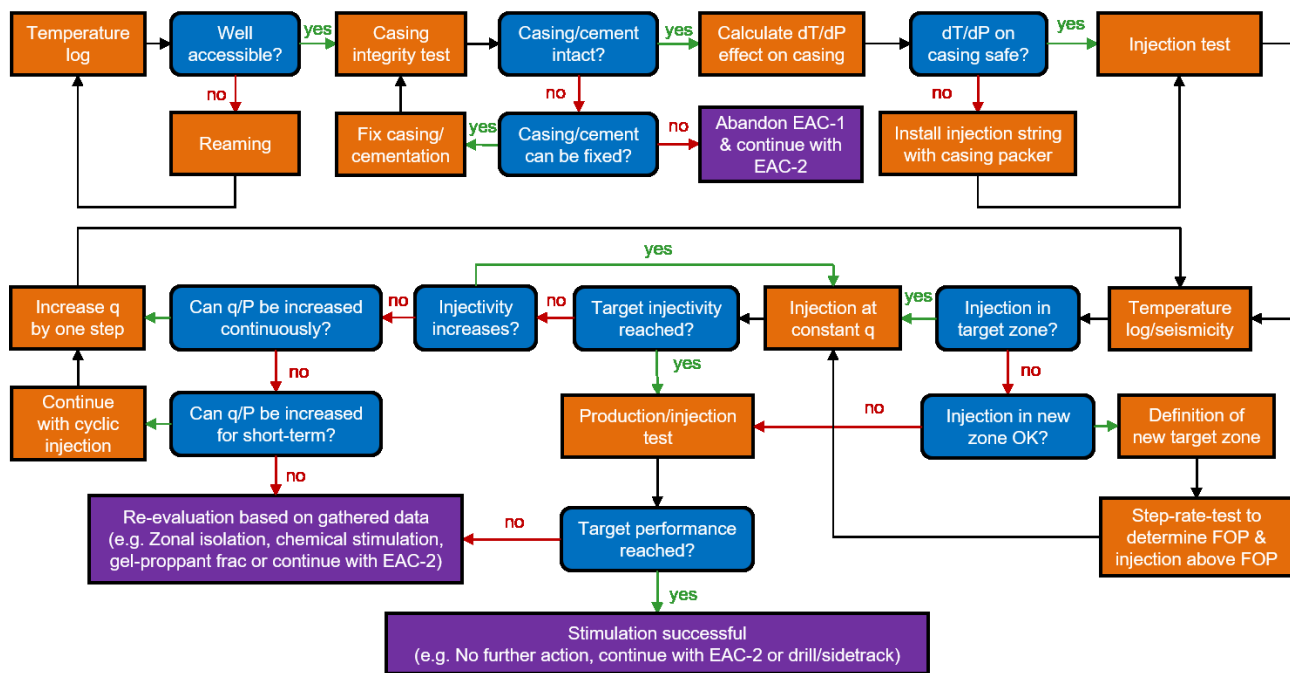


**Figure 40: Proposed EGS development workflow for Exploration wells EAC-1 or EAC-2 in Acoculco. It is recommended to start with EAC-1.**

In the end, a production or injection test should be done to evaluate the hydraulic performance increase. If this procedure does not yield the desired results, other stimulation options should be evaluated based on the acquired knowledge from these tests. If the stimulation is considered a success, stimulation of EAC-2 with monitoring in EAC-1 could follow. Depending on the results a hydraulic connection between EAC-1 and EAC-2 may or may not be possible. If a hydraulic connection may be achieved stimulation of EAC-2 should follow. If it is unlikely, it may be more feasible to drill a side-track or a second well into the stimulated cloud of EAC-1 or to use EAC-1 and EAC-2 independent of each other as injection or production wells. Independent on the commercial success, the knowledge gained during this operation will be valuable for future developments in Acoculco and similar volcanic systems.

## 10 Conclusion

The chances to develop a commercially successful EGS with the exploration wells EAC-1 and EAC-2 in Acoculco are considered relatively low. This is due to:

- limited knowledge of the local geology at depth,
- the possibility of no permeable structures that contain significant amounts of fluids near the wells,
- the current wellbore conditions (both wells are not accessible),
- the well completions that make zonal isolation difficult (long open hole sections),
- the stimulation of vertical fractures between two vertical wells due to the expected normal to strike-slip stress regime (that might not hydraulically connect the wells to each other), and
- a possible fault zone in between the two wells (that may be a barrier for fluid flow and fracture development).

Nevertheless, the optimized stimulation scenario for Acoculco wells EAC-1 and EAC-2 involves the following aspects:

- Thermal stimulation and hydraulic shear stimulation of the deep fracture zones in granites and marbles is considered the most suitable stimulation approach.
- A successful EGS with wells EAC-1 and EAC-2 requires to either access permeable structures that contain fluid or hydraulically connect both wells. Fault damage zones and fault intersections may be the only permeable structures in the vicinity of the wells, which intersected an impermeable matrix and sealed natural fractures. These are the primary stimulation targets.
- Stimulation of EAC-1 seems to be more feasible than EAC-2 due to the vicinity to the fault zones and higher fluid losses.
- Isolation of promising target zones is challenging in both wells. Therefore, an open hole stimulation test is advised after ensuring wellbore stability.
- The presented stepwise stimulation approach aims to increase the chance of success at the lowest operational risk. It is tailored to gain knowledge about EGS development in Acoculco even if no commercial EGS can be developed with the exploration wells EAC-1 and EAC-2.
- The knowledge gained by the proposed injection tests in the existing exploration wells can be the basis for a controlled development of an EGS in Acoculco with new wells specifically designed for stimulation

## References

- Alessi, R., Marigo, J. J., Maurini, C., Vidoli, S. (2018). Coupling damage and plasticity for a phase-field regularisation of brittle, cohesive and ductile fracture: One-dimensional examples. *International Journal of Mechanical Sciences*, 149:559-576. <https://dx.doi.org/10.1016/j.ijmecsci.2017.05.047>
- Avellán, D.R., Macías, J.L., Layer, P.W., Cisneros, G., Sánchez-Núñez, et al. (2019). Geology of the late Pliocene – Pleistocene Acoculco caldera complex, eastern Trans-Mexican Volcanci Belt (México). *Journal of Maps* 15(2). <https://doi.org/10.1080/17445647.2018.1531075>
- Baker Hughes, A GE Company, LLC (2018). User's Guide MFract Suite 13, pp. 770.
- Bendall, B., Hogarth, R., Holl, H., McMahon, A., Larking, A., Reid, P. (2014). Australian experiences in egs permeability enhancement-a review of case studies. Thirty-Ninth Workshop on Geothermal Reservoir Engineering, Stanford University, California, USA, February 24-26.
- Bilke, L., Flemisch, B., Kalbacher, T., Kolditz, O., Helmig, R., Nagel, T. (2019). Development of open-source porous media simulators: principles and experiences. *Transport in Porous Media* 130(1):337-361. <https://doi.org/10.1007/s11242-019-01310-1>
- Brown, D.W. (2009). Hot dry rock geothermal energy: important lessons from fenton hill. Thirty-fourth Workshop on Geothermal Reservoir Engineering, Stanford University, Stanford, California, USA, February 9-11.
- Bruna, P. O., Straubhaar, J., Prabhakaran, R., Bertotti, G., Bisdorf, K., Mariethoz, G., Meda, M. (2019). A new methodology to train fracture network simulation using multiple-point statistics. *Solid Earth* 10(2):537-559. <https://doi.org/10.5194/se-10-537-2019>
- Calcagno, P., Evanno, G., Trumphy, E., Gutiérrez-Negrín, L.C., Macías, J.L., Carrasco-Núñez, G., Liotta, D. (2018). Preliminary 3-d geological models of los humeros and acoculco geothermal fields (mexico)-h2020 gemex project. *Advances in Geosciences* 45:321. <https://doi.org/10.5194/adgeo-45-321-2018>

- Candela, T., Peters, E., Van Wees, J.D., Fokker, P., Wassing, B., Ampuero, J.P. (2019). Effect of fault roughness on injection-induced seismicity. 53rd US Rock Mechanics/Geomechanics Symposium, New York City, New York, USA, June 23-26.
- Candela, T., Renard, F., Klinger, Y., Mair, K., Schmittbuhl, J., Brodsky, E.E. (2012). Roughness of fault surfaces over nine decades of length scales. *Journal of Geophysical Research: Solid Earth* 117:B08409. <https://doi.org/10.1029/2011JB009041>
- Candela, T., Renard, F., Bouchon, M., Brouste, A., Marsan, D., Schmittbuhl, J., Voisin, C. (2009). Characterization of fault roughness at various scales: Implications of three dimensional high resolution topography measurements. *Pure and Applied Geophysics* 166:1817-1851. <https://doi.org/10.1007/s00024-009-0521-2>
- Canet, C., Hernandez-Cruz, B., Jimenez-Franco, A., Pi, T., Pelaez, B., Villanueva-Estrada, R. E., Alfonso, P., Gonzalez-Partida, E., Salinas, S. (2015). Combining ammonium mapping and short-wave infrared (SWIR) reflectance spectroscopy to constrain a model of hydrothermal alteration for the Acoculco geothermal zone, Eastern Mexico, *Geothermics* 53:154–165. <https://doi.org/10.1016/j.geothermics.2014.05.012>
- Canet C., Arana L., Gonzalez-Partida E., Pi T., Prol-Ledesma R.M., Franco S.I., Villanueva-Estrada R.E., Camprubi A., Ramirez-Silva G., Lopez-Hernandez A. (2010). A statistics-based method for the shortwave infrared spectral analysis of altered rocks: An example from the Acoculco Caldera, Eastern Trans-Mexican Volcanic Belt. *Journal of Geochemical Exploration* 105:1-10. <https://doi.org/10.1016/j.gexplo.2010.01.010>
- Chabora, E., Zemach, E., Spielman, P., Drakos, P., Hickman, S., Lutz, S., Boyle, K., Falconer, A., Robertson-Tait, A., Davatzes, N.C., et al. (2012). Hydraulic stimulation of well 27-15, desert peak geothermal field, Nevada, USA. Thirty-seventh Workshop on Geothermal Reservoir Engineering, Stanford University, Stanford, California, USA, January 30 – February 1.
- Chukwudozie, C., Bourdin, B., Yoshioka, K. (2019). A variational phase-field model for hydraulic fracturing in porous media. *Computer Methods in Applied Mechanics and Engineering* 347:957-982. <https://doi.org/10.1016/j.cma.2018.12.037>
- Deb, P., Parisio, F., Hofmann, H., Fokker, P., Dekker, E., Dueber, S. (2019). The robust stimulation model for the EGS-reservoir in the hot magmatic environment at Acoculco and its verification against the laboratory fracking experiment. GEMex Deliverable 6.5. <http://www.gemex-h2020.eu>
- Detournay, E. (2016). Mechanics of hydraulic fractures. *Annual Review of Fluid Mechanics* 48:311-339. <https://doi.org/10.1146/annurev-fluid-010814-014736>
- Dontsov, E. (2016). An approximate solution for a penny-shaped hydraulic fracture that accounts for fracture toughness, fluid viscosity and leak-off. *Royal Society open science* 3(12):160737. <https://doi.org/10.1098/rsos.160737>
- Economides, M.J., Nolte, K.G.: Reservoir stimulation. Third edition, Wiley, pp. 844.
- Ellsworth, W.L., Giardini, D., Townend, J., Ge, S., Shimamoto, T. (2019). Triggering of the Pohang, Korea, earthquake (Mw 5.5) by enhanced geothermal system stimulation. *Seismological Research Letters* 90(5):1844-1858. <https://doi.org/10.1785/0220190102>
- Farina, B., Poletto, F., Carcione, J.M., Mendrinós, D. (2020). Seismic modelling including temperature in SHGS and EGS geothermal systems. GEMex Final Conference, Potsdam, Germany, 18-19 February.



- Flores-Armenta, M., Tovar-Aguado, R. (2008). Thermal Fracturing of Well H-40, Los Humeros Geothermal Field. *Geothermal Resource Council Transactions* 32:8–11.
- Fokker, P.A., Singh, A., Wassing, B.B.T. (2020). A semi-analytical time-resolved poro-elasto-plastic model for wellbore stability and stimulation. *International Journal for Numerical and Analytical Methods in Geomechanics* 44(7):1032-1052. <https://doi.org/10.1002/nag.3048>
- Gabolde, G., Nguyen, J.-P. (2006). *Drilling data handbook*. Eight Edition, Technip, Paris, France, pp. 576.
- Garagash, D.I., Germanovich, L.N. (2012). Nucleation and arrest of dynamic slip on a pressurized fault. *Journal of Geophysical Research: Solid Earth* 117(B10310). <https://doi.org/10.1029/2012JB009209>
- Garagash, D., Detournay, E. (2000). The tip region of a fluid-driven fracture in an elastic medium. *Journal of Applied Mechanics* 67(1):183-192. <https://doi.org/10.1115/1.321162>
- Garcia, J., Hartline, C., Walters, M., Wright, M., Rutqvist, J., Dobson, P.F., Jeanne, P. (2016). The northwest geysers eggs demonstration project, California: Part 1: Characterization and reservoir response to injection. *Geothermics* 63:97-119. <https://doi.org/10.1016/j.geothermics.2015.08.003>
- Garcia-Palomo A., Macias J. L., Jimenez A., Tolson G., Mena M., Sanchez-Nunez J. M., et al. (2018). NW-SE Pliocene-Quaternary extension in the Apan-Acocolco region, eastern Trans-Mexican Volcanic Belt. *Journal of Volcanology and Geothermal Research* 349:240–255. <http://doi.org/10.1016/j.jvolgeores.2017.11.005>
- Heidbach, O., Rajabi, M., Reiter, K., Ziegler, M., WSM Team (2016). World Stress Map Database Release 2016. V. 1.1. GFZ Data Services. <http://doi.org/10.5880/WSM.2016.001>
- Hernández, A.L., Calò, M., Figueroa, A., Mendiola, L.E. (2020). Informe técnico estudio de optimización de redes sísmicas y detección de sismicidad inducida geotérmico de Acocolco. English translation “Set up of an optimized seismic monitoring system for the Acocolco injection test” by Hernández, A.L., Figueroa-Soto, A., Caló, M. GEMex report. <https://www.gemex-h2020.eu>
- Hoek, E., Carranza-Torres, C., Corkum, B. (2002). Estimating the Strength of Rock Materials. *Journal of The South African Institute of Mining and Metallurgy* 74:312-320. [https://doi.org/10.1016/0148-9062\(74\)91782-3](https://doi.org/10.1016/0148-9062(74)91782-3)
- Hofmann, H., Babadagli, T., Yoon, J.S., Blöcher, G., Zimmermann, G. (2016a). A hybrid discrete/finite element modeling study of complex hydraulic fracture development for enhanced geothermal systems (egs) in granitic basements. *Geothermics* 64:362-381. <https://doi.org/10.1016/j.geothermics.2016.06.016>
- Hofmann, H., Blöcher, G., Milsch, H., Babadagli, T., Zimmermann, G. (2016b). Transmissivity of aligned and displaced tensile fractures in granitic rocks during cyclic loading. *International Journal of Rock Mechanics and Mining Sciences* 87:69-84. <https://doi.org/10.1016/j.ijrmms.2016.05.011>
- Kalfayan, L.J. (2007). Fracture acidizing: History, Present State, and Future. SPE Hydraulic Fracturing Technology Conference, College Station, Texas, USA, 29-31 January. <https://doi.org/10.2118/106371-MS>
- Kruszewski M., Glissner M., Hahn S., Wittig V. (in review). Alkali-activated Aluminosilicates Sealing System for Deep High-Temperature Well Applications. Submitted to *Geothermics*.

- Kruszewski, M., Hofmann, H., Alvarez, F.G., Bianco, C., Haro, A.J., Garduno-Monroy, V.H., Liotta, D., Trumpy, E., Brogi, A., Wheeler, W., Bastesen, E., Parisio, F.: Integrated stress field estimation and implications for enhanced geothermals system development in Acoculco, Mexico. Submitted to *Geothermics* (in review).
- Kruszewski M., Montegrossi G., Ramírez Montes M., Wittig V., Gomez Garcia A., Sánchez Luviano M., Bracke R. (2019). A wellbore cement sheath damage prediction model with the integration of acoustic wellbore measurements. *Geothermics* 80:195-207. <https://doi.org/10.1016/j.geothermics.2019.03.007>
- Kruszewski M., Wittig V. (2018). Review of Failure Modes in Supercritical Geothermal Drilling Projects, *Geothermal Energy* 6:28. <https://doi.org/10.1186/s40517-018-0113-4>
- Lecampion, B., Bungler, A., Zhang, X. (2018). Numerical methods for hydraulic fracture propagation: a review of recent trends. *Journal of Natural Gas Science and Engineering* 49:66-83. <https://doi.org/10.1016/j.jngse.2017.10.012>
- Legarth, B., Huenges, E., Zimmermann, G. (2005). Hydraulic fracturing in a sedimentary geothermal reservoir: Results and implications. *International Journal of Rock Mechanics and Mining Sciences* 42(7-8):1028-1041. <https://doi.org/10.1016/j.ijrmms.2005.05.014>
- Lepillier, B., Yoshioka, K., Parisio, F., Bakker, R., Bruhn, D. (in review). Variational phase-field modelling of hydraulic fracture interaction with natural fractures and applications to enhanced geothermal systems. Submitted to *Journal of Geophysical Research: Solid Earth*. <https://doi.org/10.1002/essoar.10502690.1>
- Lepillier, B., Bruna, P.-O., Bruhn, D., Bastesen, E., Daniilidis, A., Garcia, Ó., Torabi, A., Wheeler, W. (2020). From outcrop scanlines to discrete fracture networks, an integrative workflow. *Journal of Structural Geology* 133:103992. <https://doi.org/10.1016/j.jsg.2020.103992>
- Lepillier, B., Hofmann, H. (2019). Acoculco wellbore hydraulic fracture stimulation models. Preliminary internal GEMex report, December 13. <https://www.gemex-h2020.eu>
- Lepillier, B., Hofmann, H. (2020). Acoculco Wellbore Hydraulic Fracture Stimulation models (Review). Internal GEMex report, May 4, 2020. <https://www.gemex-h2020.eu>
- Lepillier, B., Daniilidis, A., Gholizadeh, N.D., Bruna, P.-O., Kummerow, J., Bruhn, D. (2019). A fracture flow permeability and stress dependency simulation applied to multi-reservoirs, multi-production scenarios analysis. *Geothermal Energy* 7:24. <https://doi.org/10.1186/s40517-019-0141-8>
- Lopez-Hernandez, A., Garcia-Estrada, G., Aguirre-Diaz, G., Gonzalez-Partida, E., Palma-Guzman, H., Quijano-Leon, J.L. (2009). Hydrothermal activity in the Tulancingo–Acoculco Caldera Complex, central Mexico: Exploratory studies. *Geothermics* 38(3):279-293. <https://doi.org/10.1016/j.geothermics.2009.05.001>
- Lorenzo-Pulido, C., Armenta-Flores, M., Ramirez-Silva, G. (2010). Characterization of the acoculco geothermal zone as a HDR system. *Geothermal Resources Council Transactions* 34:369-372.
- Luviano, M.S., Armenta, M.F., Montes, M.R. (2015). Thermal stimulation to improve the permeability of geothermal wells in Los Hornos Geothermal Field, Mexico. *World Geothermal Congress*, Melbourne, Australia, 19-25 April.
- Marinos, P., Hoek, E. (2000). GSI: A geologically friendly tool for rock mass strength estimation. *ISRM International Symposium*, Melbourne, Australia, 19-24 November.

- Matsunaga, I., Niitsuma, H., Oikawa, Y. (2005) Review of the HDR development at Hijiori site, Japan. World Geothermal Congress, Antalya, Turkey, 24-29 April 2005.
- McClure, M.W., Horne, R.N. (2014). An investigation of stimulation mechanisms in enhanced geothermal systems. *International Journal of Rock Mechanics and Mining Sciences* 72:242-260. <https://doi.org/10.1016/j.ijrmms.2014.07.011>
- Milsch, H., Hofmann, H., Blöcher, G. (2016). An experimental and numerical evaluation of continuous fracture permeability measurements during effective pressure cycles. *International Journal of Rock Mechanics and Mining Sciences* 89:109-115. <https://doi.org/10.1016/j.ijrmms.2016.09.002>
- Nordgren, R.P. (1972). Propagation of a vertical hydraulic fracture. *SPE Journal* 12(4):306-314. <https://dx.doi.org/10.2118/3009-PA>
- Parisio, F., Yoshioka, K. (in review). Modeling fluid re-injection in a stimulated geothermal reservoir. Submitted to *Geoscience Letters*.
- Perkins, T.K., Kern, L.R. (1961). Width of hydraulic fractures. *Journal of Petroleum Technology* 13(9):937-949. <https://dx.doi.org/10.2118/89-PA>
- Peters, E., Angelone, M., Bongiovanni, G., Spaziani, F., Verrubbi, V., Guidarelli, M., Priolo, E., Candela, T., van Wees, J. D., 2020a. Report on environmental risk assessment and mitigation strategies. GEMex Deliverable D7.3. <https://www.gemex-h2020.eu>
- Peters, E., Candela, T., Lepillier, B., Hofmann, H., Deb, P., Kruszewski, M., Wheeler, W., Bastesen, E., Trumphy, E., Weydt, L., Bär, K., Sass, I., van Wees, J. D., 2020b. Report on model of potential drill target and proposed drill path. GEMex Deliverable D7.1., <https://www.gemex-h2020.eu>
- Petty, S., Nordin, Y., Glassley, W., Cladouhos, T.T., Swyer, M. (2013). Improving geothermal project economics with multi-zone stimulation: Results from the Newberry Volcano EGS demonstration. Thirty-eighth Workshop on Geothermal Reservoir Engineering, Stanford University, Stanford, California, USA, February 11-13.
- Pfeiffer, L., Bernard-Romeo, R., Mazot, A., Taran, Y. A., Guevara, M., Santoyo, E. (2014). Fluid geochemistry and soil gas fluxes (CO<sub>2</sub>-CH<sub>4</sub>-H<sub>2</sub>S) at a promissory Hot dry Rock Geothermal System: The Acoculco caldera, Mexico. *Journal of Volcanology and Geothermal Resources* 284:122–137. <https://doi.org/10.1016/j.jvolgeores.2014.07.019>
- Mendrinós, D., Kalantzis, C., Karytsas, C., Poletto, F., Barison, E., Farnia, B., Corubolo, P., Angelone, M., Montereali, M.R., Crovato, C., Nardi, E., Armiento, G., de Cassan, M.G., Caprioli, R., Propositio, M., Muller, J. (2020). Concept for performance characterization of the target area. GEMex Deliverable 8.4. <https://www.gemex-h2020.eu>
- Rocha S., Jimenez E., Palma H. (2008). Propuesta para dos pozos exploratorios en el proyecto geotermico de Acoculco, Pue, CFE Departamento de Exploracion report OGL-ACO-03/06, 2006. Schlumberger, Reporte Tecnico, Pozo EAC-2, Intervalo: 803 - 1394 m.
- Savitski, A., Detournay, E. (2002). Propagation of a penny-shaped fluid-driven fracture in an impermeable rock: asymptotic solutions. *International Journal of Solids and Structures* 39(26):6311-6337. [https://doi.org/10.1016/S0020-7683\(02\)00492-4](https://doi.org/10.1016/S0020-7683(02)00492-4)

- Schill, E., Genter, A., Cuenot, N., Kohl, T. (2017). Hydraulic performance history at the soultz egs reservoirs from stimulation and long-term circulation tests. *Geothermics* 70:110-124.  
<https://doi.org/10.1016/j.geothermics.2017.06.003>
- Terakawa, T., Miller, S.A., Deichmann, N. (2012). High fluid pressure and triggered earthquakes in the enhanced geothermal system in Basel, Switzerland. *Journal of Geophysical Research: Solid Earth* 117:B07305. <https://doi.org/10.1029/2011JB008980>
- Verma, S.P. (2001). Geochemical evidence for a lithospheric source for magmas from Acoculco caldera, Eastern Mexican Volcanic Belt. *International Geology Review* 43:31-51.
- Watanabe, N., Wang, W., Taron, J., Görke, U., Kolditz, O. (2012). Lower-dimensional interface elements with local enrichment: application to coupled hydro-mechanical problems in discretely fractured porous media. *International Journal for Numerical Methods in Engineering* 90(8):1010-1034.  
<https://doi.org/10.1002/nme.3353>
- Weydt, L. M., Ramírez-Guzmán, A. A., Pola, A., Lepillier, B., Kummerow, J., Mandrone, G., Comina, C., Deb, P., Norini, G., Gonzalez-Partida, E., Avellán, D. R., Macías, J. L., Bär, K., and Sass, I. (in review). Petrophysical and mechanical rock property database of the Los Humeros and Acoculco geothermal fields (Mexico). Submitted to Earth System Science Data.
- Weydt L. M., Bar K., Colombero C., Comina C., Deb P., Lepillier B., Mandrone G., Milsch H., Rochelle C. A., Vagnon F., Sass I. (2018). Outcrop analogue study to determine reservoir properties of the Los Humeros and Acoculco geothermal fields, Mexico, *Advances in Geosciences* 45:281-287.  
<https://doi.org/10.5194/adgeo-45-281-2018>
- Yoshioka, K., Parisio, F., Naumov, D., Lu, R., Kolditz, O., & Nagel, T. (2019). Comparative verification of discrete and smeared numerical approaches for the simulation of hydraulic fracturing. *International Journal on Geomathematics*, 10(1):1-35. <https://doi.org/10.1007/s13137-019-0126-6>
- Yoshioka, K., Bourdin, B. (2016). A variational hydraulic fracturing model coupled to a reservoir simulator. *International Journal of Rock Mechanics and Mining Sciences* 88:137-150.  
<https://doi.org/10.1016/j.ijrmms.2016.07.020>
- Yoshioka, K., Jermia, J., Pasikki, R., Ashadi, A. (2015). Zonal hydraulic stimulation in the Salak geothermal field. World Geothermal Congress, Melbourne, Australia, 19-25 April.
- Zimmermann, G., Blöcher, G., Reinicke, A., Brandt, W. (2011). Rock specific hydraulic fracturing and matrix acidizing to enhance a geothermal system – Concepts and field results. *Tectonophysics* 503:146-154.  
<https://doi.org/10.1016/j.tecto.2010.09.026>
- Zimmermann, G., Reinicke, A., Blöcher, G., Moeck, I., Kwiatek, G., Brandt, W., Regenspurg, S., Schulte, T., Saadat, A., Huenges, E. (2010). Multiple fracture stimulation treatments to develop an enhanced geothermal system (EGS)-conceptual design and experimental results. World Geothermal Congress, Bali, Indonesia, 25-29 April.
- Zoback, M.D. (2007). *Reservoir Geomechanics*, Cambridge University Press.

## Acknowledgments

We kindly acknowledge the data received from the Comisión Federal de Electricidad (CFE) on the two wells EAC-1 and EAC-2. We would like to thank CFE's staff for the fruitful discussions. We also thank Baker Hughes for providing an academic license of the MFrac Suite for research purposes.



Coordination Office, GEMex project  
Helmholtz-Zentrum Potsdam  
Deutsches GeoForschungsZentrum  
Telegrafenberg, 14473 Potsdam  
Germany